Pressure-Induced Electronic Phase Transitions
in
Transition Metal Oxides and Rare Earth Metals

By

Brian Ross Maddox
B.S. (California State University, Hayward) 2000

DISSERTATION

Submitted in partial satisfaction of the requirements for the degree of

Doctor of Philosophy

in

Physics

in the

OFFICE OF GRADUATE STUDIES

of the

UNIVERSITY OF CALIFORNIA
DAVIS

Approved:

_____

_____

_____

Committee in Charge

2006

"Other things may change us, but we start and end with family"

-Anthony Brandt

Acknowledgements

I would like to thank my LLNL mentor Dr. Choong-Shik Yoo and my advisors at UC Davis Prof. Warren E. Pickett and Prof. Richard T. Scalettar, whose patience and enthusiasm inspired me to stay focused and work hard. I would also like to thank my loving family. It is only through their unwavering support and encouragement I am the man I am today.

I would also like to acknowledge financial support from the Student Employee Graduate Research Fellowship program at Lawrence Livermore National Laboratory as well as the Stewardship Science Academic Alliance Program.

Abstract

Pressure-Induced Electronic Phase Transitions

in

Transition Metal Oxides and Rare Earth Metals

by

Brian Ross Maddox

Electron correlation can affect profound changes in a material's bulk properties. When the degree of correlation is changed, phase transitions can sometimes result. Because electron correlation stems from the Coulomb interaction, whose strength changes with distance, applying pressure can inducing changes in the degree of electron correlation by altering the interatomic distances of crystalline materials. This dissertation presents a study of a number of correlated systems at ultrahigh pressures generated by diamond-anvil cells. Some of these systems, which were once thought to undergo very similar phase transitions under pressure, are shown to behave very differently from each other at high pressure

The Mott transition is an example of a phase transition resulting from changes in the degree of electron correlation. A sharp transition induced by pressure from a highly correlated, insulating state to a weakly correlated, metallic state was predicted for the transition metal monoxides (MnO, FeO, CoO, and NiO) some 50 years ago. Numerous studies aimed at observing this transition have been unsuccessful. We present a study of MnO aimed at determining not only its crystal structure at high pressure but also its magnetic properties. Our results provide the first observance of the Mott transition in a transition metal monoxide.

The lanthanides (the $4f$ metals also known as rare-earths) are a series of elements known to possess strong correlations among their $4f$ electrons. At high pressure, many of these elements undergo phase transitions accompanied by large reductions in volume. The most notable of these elements is cerium (Ce) which, at just under 1 GPa (100,000 atmospheres), shrinks in volume by 15% without changing its underlying crystal structure. This transition is widely believed to be the result of changes in the degree of $4f$ correlation. We present a study of various light rare-earth metals using similar techniques to those used to study MnO. Our results show that these materials do not undergo Mott transitions at high pressure as some have suggested. A smooth and prolonged electronic transition under pressure was observed. A key signature of the Mott transition, *i.e.*, a vanishing magnetic moment, was also absent in the lanthanides. These results suggest that a Kondo-like model best describes the electron correlation behavior in the lanthanides.

A number of related materials were also studied at high pressure and discussed in this dissertation. Among these materials, half-metallic chromium dioxide (CrO_2) presents a unique opportunity to study the effects of electronic structure on a material's structural properties. CrO_2 possesses a very common crystal structure at ambient conditions: the six-fold coordinated rutile structure. This simple structure is shared by many other transition-metal oxides including stishovite (SiO_2), which makes up 50% of the Earth's weight and is an important geological material in the Earth's deep interior. However, CrO_2 is the only rutile-structured compound that is half-metallic. We present a high pressure structural study of CrO_2 and compare our findings to other rutile-structured compounds. Strong systematics are uncovered linking the ambient pressure lattice distortions present in virtually all rutile-structure compounds to their respective transition pressures to the orthorhombic $CaCl_2$ structure. An anomaly in the compressibility of CrO_2 at high pressure is also presented and discussed in the context of a possible half-metal to metal transition.

Contents

List of Tables

List of Figures

Chapter 1

Introduction

1.1 Motivation

The world of solid state physics before 1949 was dominated by the idea that electrons in a solid only interact with the large, immobile ion cores and could thus be treated independently from each other. The band theory of solids, for which Felix Bloch and Alan Wilson are most famous, was the crowning achievement during this period in the physics of crystalline materials [15, 16]. Guided by the relatively new principles of quantum mechanics, Wilson postulated that electrons (which can only take on discrete energy values in an atom) will form bands of allowed energies when brought together to form a solid. According to Wilson, for any material to be a good conductor they need to contain a partially filled band. Since each band can only hold two electrons due to the Pauli exclusion principle, any material which has an odd number of electrons per unit cell should be a metal. The Bloch-Wilson theory was wildly successful in explaining the sharp division between insulating and conducting materials, a problem that had plagued physicists for decades. It was so successful that, to this day, it is virtually impossible to discuss the electronic and magnetic properties of materials without invoking the principle of electronic

bands.

Physicists soon discovered that NiO, when approached using Wilson's band theory, was predicted to be metallic when in fact it was an electrical insulator. The key problem with Wilson's model was this long-standing principle that the electrons could be treated independently. In a paper written in 1949 entitled "The Basis of the Electron Theory of Metals, with Special Reference to the Transition Metals" [17], N. F. Mott theorized that in some materials it was precisely the opposite. It was these interactions, or "correlations", between the electrons themselves which dominated the electronic properties in the solid. This interaction is really nothing more than the well known coulomb interaction but has far-reaching implications for the transport properties of some materials. If strong enough, these correlations can turn a simple material like NiO into an insulator. These materials, for which strong electron correlations exist, became known as Mott insulators.

One exciting prediction born out of Mott's work was the existence of a transition between two regimes; one where electron correlation dictates the materials' properties and another where the kinetic energy of the system can override the strong correlations. This become known as a Mott transition and was originally predicted for the transition metal oxides NiO, FeO, MnO and CoO, the prototypical insulators used to illustrate Mott's ideas. He described an energy E required to remove an electron from one site to another, as in metallic conduction. He theorized that the application of pressure would reduce E by bringing the ions closer together. At a critical distance the materials would undergo a sharp transition to the metallic state. It has since been shown that some of the most technologically important materials derive their properties from electron correlations. The most striking example is in the high T_c superconducting cuprates, of which belongs a mercury bearing cuprate with the highest T_c to date of 138 K. These materials are composed of copper oxide layers which, when doped, undergo a Mott transition.

Despite the importance of Mott's work and the relevance to a number of technologically important materials, the Mott transition at high pressure in the transition metal monoxides has yet to be seen. A lower limit of 143 GPa has been placed on FeO by Badro *et al.* [14] using inelastic x-ray scattering techniques. Similarly, NiO has been studied to over 1 Mbar by Rueff *et al.* and has yet to undergo a pressure-induced Mott transition. These results leave many questions unanswered. Most importantly, are the transition metal monoxides truly Mott insulators and, if so, at what pressures do they metallize?

1.2 Rare-Earth Volume Collapse

Another phenomenon which involves changes in electron correlation occurs in the elemental rare-earth metal Ce. At a pressure of 7 kbar, trivalent Cerium undergoes a dramatic 15% change in volume [18]. This volume collapse occurs abruptly, *i.e.*, first-order. What is more interesting is that it occurs without a change in crystal structure. All materials become more dense with pressure and, in general, transform to more close-packed structures. And, these transitions are very often accompanied by large volume changes. However, the γ-α transition in Ce was isostructural and must therefore occur due to changes at the atomic level.

It was later discovered that many of the other $4f$ metals undergo similar volume-collapse transitions (VCTs) at high pressure. Figure 1.1 (reprinted from Ref. [3]) summarizes these transitions for the lanthanides Ce through Gd. Although Cerium's is the only isostructural VCT, the physical mechanism underlying all these transitions is thought to be the same. It is generally believed that these VCT transitions are the result of changes in the degree of $4f$ correlation at high pressures. However, there is an ongoing debate to whether these changes in f-f correlation are the result of changes in the strength of the

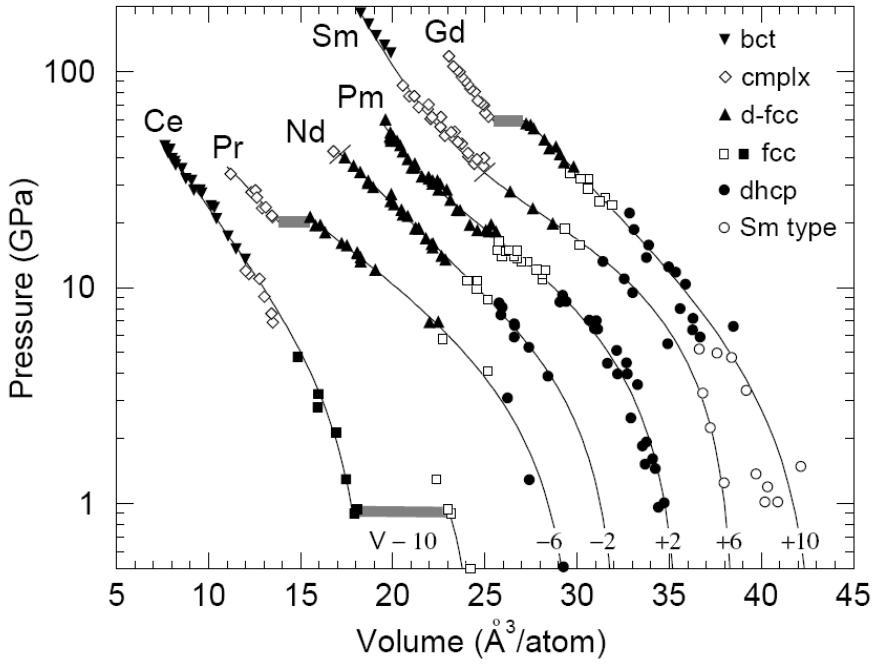

Figure 1.1. Pressure vs. volume relations for the lanthanides Ce through Gd. Figure reprinted from Ref. [3]

correlations themselves or whether they are due to increasing f-valence hybridization. The following sections give a chronology of the models proposed to describe the VCTs in the rare-earths.

The Promotional Model

The promotional model was the first, and most straightforward, scenario proposed to describe the isostructural volume-collapse phenomenon in Ce. Most of the lanthanides are trivalent, with the exception of Eu and Yb which each steal one valence electron to make a half-filled and filled $4f$ orbital, respectively. This leaves Ce with an electron configuration of $4f^1$, despite it being the second of the lanthanide series. In 1968, Coqblin *et al.* hypothesized that the volume-collapse was the result of a promotion of this single single $4f$ electron into the valence orbitals [19].

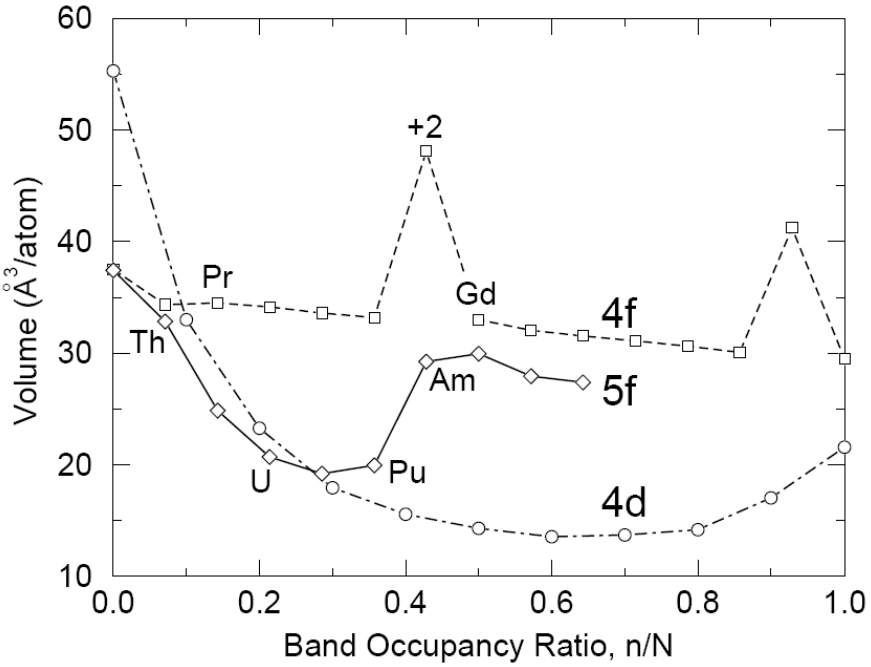

Figure 1.2. Ambient pressure atomic volumes for the $4f$ and $5f$ metals (along with those of the $4d$ elements). Not that both Eu and Yb have anomalously large volumes compared to the rest of the $4f$ series. Figure reprinted from Ref. [3]

The $4f$ electrons in the rare-earths are highly localized, a result of strong correlations between the $4f$ electrons, forming very narrow energy bands. Thus, they tend to screen the positive nuclear core charge acting on the valence electrons. This effect is illustrated in Fig. 1.2 (taken from Ref. [3]). Both Eu and Yb, which are divalent, display anomalously large atomic volumes compared with the rest of the trivalent $4f$ metals. It was therefore hypothesized that the sudden VCT transition in Ce was the result of a valence change from trivalent to tetravalent, resulting from the promotion of single $4f$ electron. The reduced screening of the core potential would increase the core-valence attraction, reducing the size of the Ce atoms.

Mott Transition

One commonality between the rare earth metals, post-collapse (with the exception of Ce), is their low symmetry crystal structures. These structures are in contrast to the high-symmetry, cubic structures that occur pre-collapse at low pressures. These low-symmetry structures are similar to those found in the $5f$ metals (the actinides) and are characteristic of f-electron bonding. This fact led physicist B. Johansson to believe that the $\alpha - \gamma$ transition in Ce was the result of a "metallization" of the $4f$ electrons by band broadening, i.e. a change in the f-f correlation resulting in a Mott transition within $4f$ orbitals [20]. The delocalized f electrons would then be able to participate in bonding, causing the very low symmetry structures seen post-collapse.

The Kondo VCT Scenario

A very different picture of the Ce volume-collapse was proposed by Lavagna *et al.* [21] in 1982 based on photoemission results on "chemically" compressed" Ce alloys obtained the previous year [22]. These results indicated not only that the binding energy of the single $4f$ electron was much too large for $4f$ promotion (this value needs to be ~ 0.1 eV in the promotional model, compared to the experimentally determined value of 2 eV) but also that the position and width of the $4f$ density of states is, for the most part, volume independent. This latter point is in disagreement with the Mott transition model which relies on the broadening of the narrow $4f$ band and the eventual overlap with the unoccupied $4f$ band.

In the Kondo volume-collapse picture the $4f$ electrons stay strongly localized in the collapsed phase and act as impurity states in a sea of conduction electrons. As the volume is reduced, the hybridization between the $4f$ and valence orbitals is enhanced. In this way, the net occupation of the $4f$ orbitals stays near their pre-collapse values, but

resonate between the $4f$ states and valence states.

Kondo VCT vs. Mott Transition

Despite the apparent disagreement between photoemission experiments and the Mott transition scenario for the rare-earth volume-collapse, recent theoretical calculations by McMahan *et al.* [23] suggest the two models used to simulate these transitions, namely the Hubbard model and the periodic Anderson model, are more similar than previously thought. These calculations show both models reproduce the Kondo resonance, which appears upon compression and represents screening of the $4f$ moment by the valence electrons.

How does one then decide which scenario is the correct description of the volume-collapse phenomenon? Although both models reproduce the Kondo screening effects, the two scenarios do differ in the way the $4f$ moment evolves across the transition. In the Mott transition scenario, the reduction in correlation between the $4f$ electrons would result in a collapse of the $4f$ magnetic moment across the transition. In the Kondo VCT scenario the $4f$ electrons stay strongly localized and retain their moment. The models also differ in the abruptness of the transition. The Mott transition should result in an abrupt metallization whereas the Kondo VCT predicts a smooth increase in f-valence hybridization.

1.3 Experimental Approach

Ultrahigh pressures were generated using diamond anvil cells (DACs) (see Sec. 3.1). The DAC uses diamonds, the hardest material known to man, to apply a force over a very small area, thus generating very high pressures. The DAC is also compact (can fit in the palm of your hand) and the diamonds are optically transparent, making it ideal of optical experiments.

1.3.1 X-ray Spectroscopy at High Pressure

The introduction of 3rd generation synchrotron sources in 1994, and the Advanced Photon Source at Argonne National Laboratory in 1996, opened up the possibility of applying new experimental techniques to some of the longest standing problems in solid state physics. The device used to generate the high static pressures in this study (the DAC) usessamples on the order of 100 μm in diameter and 30 μm thick (see Sec. 3.1). Because of these microscopic sample sizes, a high brilliance x-ray source is needed to produce focused probe beams on the scale of our samples. The 3rd generation synchrotron sources available today, coupled with undulator insertion devices, can provide high flux x-ray beams in the hard x-ray region with diameters down to 12×12 μm.

1.3.2 Systems of Interest

The following sections introduce each material studied in this work. A more detailed background discussion is presented in Chapter 2.

MnO

Manganese oxide (MnO) is the lightest of the original $3d$ transition metal monoxides predicted to undergo a Mott transition. The pressure required for MnO to undergo a Mott transition should therefore be lower than that of FeO, NiO, and CoO since correlations between the $3d$ electrons become stronger with increasing d occupation. MnO also has a number of unresolved issues at high pressure including an unknown crystal structure between 90 and 120 GPa [4]. A search for the Mott transition in MnO at high pressure was conducted using x-ray emission spectroscopy (XES) to probe the magnetic moment of the $3d$ electrons. This was coupled with angle-dispersive x-ray diffraction (ADXRD) to resolve the crystal structure and to study the effects of electron correlation on the structural

properties.

Ce, Pr, Nd, Gd

Four of the first eight lanthanides (Ce, Pr, Nd, and Gd) were studied at high pressure using inelastic x-ray scattering to do determine which of the models described in Sec. 1.2 is most appropriate. Neodymium was chosen along with Ce, Pr, and Gd because, unlike those materials, Nd reaches the low-symmetry, f-bonding-like structures without undergoing a volume collapse.

Related Materials: Half-Metallic CrO_2

Even within the seemingly well understood class of metals there exists a subgroup of materials which show properties of both metals and insulators. These materials are named half-metals because the portion of electrons that are, say, spin up show metallic conductivity whereas the other portion of electrons that are spin down exhibit insulating behavior. This property makes half-metals a potential source of spin-polarized current and a crucial component in the fledgling field of spintronics, a field in which researchers try to take advantage of not only the electron charge in integrated circuits but also their spin.

Chromium dioxide (CrO_2) is unique among the transition-metal dioxides and is one of the most promising spintronics materials due to its wide availability and high spin polarization [24]. It also shares a very common, scientifically important crystal structure at ambient conditions; the rutile structure. This structure is shared with many other common materials including TiO_2, an important industrial colorant, and SiO_2, an important geological mineral making up approx 50% of the Earth's weight. It is therefore important to understand the link between these materials' electronic structure and its structural properties at ultrahigh pressures, like those found deep in the Earth's interior. How a material's

electronic structure influences its physical properties is also an important consideration in the electronics industry. The availability of high pressure data on similar rutile-structured materials presents a unique opportunity to study the effects of CrO_2's unique electronic strucuture on its physical properties. A high pressure structural study of CrO_2 was performed, using angle-dispersive x-ray diffraction and Raman spectroscopy, to investigate this most important question.

1.4 Dissertation Outline

The remainder of this dissertation is arranged into five chapters and two appendices. Chapter two introduces key concepts and provides a literature review of the materials discussed above. Chapter three includes details descriptions of the apparatus used in this study along with experimental details for each material studied. Chapters four and five describe our results and present analysis and discussions of those results. Conclusions are given at the beginning of Chapter six, which ends with an outline of outstanding questions and suggests future work that may provide answers to these questions. Appendix A presents a derivation of the Bragg condition for the diffraction of x-rays, a key equation for dealing with x-ray diffraction data, while Appendix B discusses the physical origin of the Raman effect

Chapter 2

Background Material

2.1 Important Concepts

2.1.1 Mott Insulators

The original picture put forth by N. F. Mott in 1949 to describe NiO and the other transition-metal oxides was one in which a finite amount of energy was required to remove an electron from one Ni atom, leaving Ni^{3+}, and place it on a *distant* Ni atom, forming a Ni^{1+} ion [17]. These pairs are required for conduction by electron transfer. However, unless the material is in an excited state, these pairs do not exist. Therefore, as the temperature is reduced, electrical resistance increases, in agreement with that of an insulator. It was then postulated that for those materials, such as NiO, in which the interatomic metal-metal distances are large, an atomic-like model such as the London-Heitler model, is appropriate.

However, it was noted that the London-Heitler model did not allow for an electric current. Mott realized that the explanation put forth by some that there would be present a small number of ionized states within the London-Heitler approximation could not be correct. He noted that, in fact, there would either be no ionized pairs, or a very large

number, such that the approximation would become invalid and one would need to apply a collective electron model like that of Wilson which used a collection of Bloch states to describe a solid. This is because a small number of pairs would result in a screening of the positive core potentials, altering the core potential into the form $-(e^2/\kappa r)exp\,(-qr)$. The screening constant, q, depends on the number of pairs. If q is large enough then no more bound states exist and the work required to create a Ni^{3+}-Ni^{1+} pair is removed. A sharp transition would then occur between the two regimes in which no conduction can occur (an insulating state) and one where conduction can occur freely (a metallic state). It was predicted by Mott that the application of pressure could drive NiO through this transition by reducing the inter-atomic spacing between the Ni ions. This transition became known as the Mott transition.

2.1.2 The Hubbard Model

A modern view of the Mott insulator came in 1963 with the introduction of the Hubbard model [25]. Based on the tight-binding approximation, the Hubbard model describes conduction as the hopping of electrons from their atomic-like orbitals, a departure from the current theories at the time which used a free-electron gas to describe the conduction band of solids. This hopping picture allowed Hubbard to describe the onsite electron correlation which, in the $3d$ metals, plays a larger role in determining the transport properties than does the conduction band.

The Hubbard model can be best illustrated by considering a 1D chain of hydrogen atoms. Since the model is based on the tight-binding model, we consider that each electron occupies a 1s orbital. The hamiltonian for the system can then be written as

$$H = -t \sum_{<i,j>,\sigma} c^{\dagger}_{i,\sigma} c_{j,\sigma} + U \sum_{i=1}^{N} n_{i\uparrow} n_{i\downarrow} \tag{2.1}$$

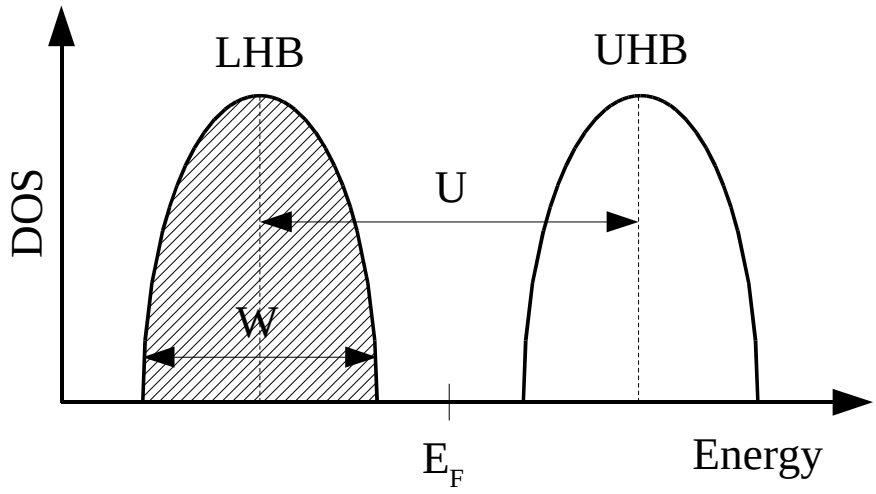

Figure 2.1. A schematic density of states for the 1D Hubbard model at half-filling for $U/W > 1$. The addition of a non-zero U causes a splitting of the $1s$ band into upper (UHB) and lower (LHB) Hubbard bands. The hopping integral t is related to the bandwidth by $W = 4t$.

where U is a measure of the Coulomb interaction between electrons occupying the same orbital. It is this U which gives rise to electron correlation. The hopping integral, t, is determined by the orbital overlap and represents the kinetic energy of the hopping electrons. At half filling, *i.e.*, the number of electrons equals the number of sites N, band theory predicts this 1D chain to form a partially filled band and be metallic. In fact, the 1D Hubbard model at half-filling is exactly solvable for $U = 0$. The energy eigenvalues $e_k = -2t\ cos\ k$ represent an idealized energy band of width $W = 4t$, forming a metallic state. However, the addition of the onsite coulomb interaction term U creates a competition between the kinetic energy and the onsite replusion. Figure 2.1 shows the density of states for the 1D hubbard model at half-filling for $U/W > 1$ and $T = 0$. For large values of U the $1s$ band is split into upper (UHB) and lower (LHB) Hubbard bands, each able to hold N electrons.

The Mott Transition

Figure 2.1 shows that the ratio U/W determines whether the system will behave like an insulator (strongly correlated) or a metal (weakly correlated). When $U/W < 1$ the UHB and LHB overlap, causing an abrupt transition to the metallic state. The Hubbard U is relatively volume-independent since it mostly depends on what happens on a single ion. However, the bandwidth W is sensitive to temperature and pressure. Pressure increases W by reducing the interionic distances, thus increasing the orbital overlap integral t. When the pressure is increased to the point where $U/W < 1$, a Mott transition occurs. It should be noted that Lieb and Wu [26] proved there is no Mott transition in the 1 band Hubbard model for any positive, non-zero value of U. However, real materials must be treated in 2 or 3 dimensions.

The main physical manifestation of a Mott transition is an abrupt increase in conductivity resulting from the UHB and LHB band overlap. It is often difficult, however, to determine whether an insulator-metal transition is indeed a Mott transition because other mechanisms of metallization exist. Changes in the crystal field surrounding the metal ions in a material sometimes occur as a result of structural phase transitions. These changes often lead to insulator-metal transitions. In a Mott transition, however, the metallization is due to a change in electron correlation and is punctuated by a signature in the local moment on the correlated orbital. In general, metallization due to changes in correlation is accompanied by such signatures. This is because the same strong correlations that lead to the Mott insulator are also responsible for the formation of local moments. In a mean field picture, the metallization during a Mott transition is accompanied by a the loss of the local moment.

2.1.3 The Kondo Lattice Model

The simplest hamiltonian used to describe the Kondo lattice is more complicated than the 1D Hubbard model used in Sec. 2.1.2 due to the multiple orbitals necessary to describe the model, i.e. a highly correlated $4f$ impurity orbital and the valence orbitals. It is based on the periodic Anderson impurity model (PAM) where the $4f$ electrons are treated as the impurities. The strong correlations between the $4f$ electrons split the $4f$ band into upper and lower bands, similar to the UHB and LHB in the Hubbard model. Consequently, they are also often referred to as the UHB and LHB. The relevant parameters of the Kondo lattice model are also analogous to those of the Hubbard model: D, equal to $1/2$ the width of the conduction band, and the exchange parameter J, which describes the hybridization between the $4f$ states and the valence states, are analogous to W and U from the Hubbard model. The ratio $|J|/D$ described the degree of hybridization and depending on its value, determines whether the $4f$ states are metallic or insulating [27].

However, the Kondo lattice model differs from the Hubbard model in the way the $4f$ electrons interact from site to site. In the Kondo model, the $4f$ electrons are treated as highly localized, with little to no orbital overlap. Thus, they can only interact inter-site indirectly, through hybridization with the valence orbitals. This indirect interaction is known as the RKKY interaction and gives rise to the ferromagnetic behavior of the rare-earth metals. Because they are so highly localized, the $4f$ electrons form strong Hund's rule moments. In the RKKY interaction, these moment develop long-range order by interacting with the valence electrons, which align their spins with spin of the $4f$ electrons. These valence electrons then interact with other valence electrons on adjacent sites, creating a correlation between $4f$ electrons on the adjacent sites.

The Kondo Volume-Collapse Model

In the Kondo volume-collapse model, pressure enhances the ratio $|J|/D$, driving the system into a "Kondo state" where the $4f$ moment is screened by the valence electrons. This differs from the RKKY interaction at low temperature, which aligns parallel with the $4f$ electrons, by forming a spin singlet with the $4f$ electrons. In contrast with the Hubbard model, in this Kondo state the $4f$ electrons stay highly correlated and do not delocalize in the way described in the Hubbard model, i.e. band overlap. Rather, the increased hybridization with the valence orbitals allows a $4f$ electron to "hop" to an adjacent site via this hybridization. The signature seen in the local moment for the Kondo volume-collapse model is a screening of the local moment. Hence, the Kondo state can be distinguished from the metallic state described within the framework of the Hubbard model using techniques that can probe local magnetic moments (see Sec. 3.2.3).

2.2 Materials Information

2.2.1 MnO

The Search for the Mott transition

Since the discovery of Mott insulators and the prediction that pressure could drive these correlated materials into the metallic state, much experimental and theoretical work has been performed to validate this prediction and to study the properties of insulator-metal transitions in general. In addition to the original materials considered by Mott, i.e. the transition-metal oxides, many other materials have been found to be Mott insulators and undergo a Mott transition. For example, the cuprate superconductor $La_{2-x}Sr_xCuO_4$ is an antiferromagnetic (Mott) insulator at $x = 0$ with one hole per Cu atom. The Mott transition is much easier to access in this material since it can be induced chemically by changing the

number of holes on the Cu atoms, *i.e.*, making $x \neq 0$. Not only does the system become metallic, it also becomes superconducting! Antiferromagnetic order is also lost, illustrating the strong connection between the Mott transition and magnetism suggested in Sec. 2.1.2.

Identifying and validating the Mott transition scenario in the transition metal monoxides under pressure is much more difficult. This is because the correlation is so strong that any correlation driven transition in these materials will only occur at pressures exceeding 1 MBar. A conductivity study in 1971 by Kawai *et al.* [28] claimed to have seen an insulator→metal transition in NiO at less than 20 GPa. A much more recent study, however, has proven this to be false. A structural study conducted in 2000 by Eto *et al.* [29] showed the $dB1$ structure to stable in NiO, with no addition phase transformations, to at least 147 GPa. An even more recent study by Rueff *et al.* [30] has shown that the $3d$ moment in NiO persists to over 1 MBar. Similar results have been obtained on FeO by Badro *et al.* [14] in 1999 who reported that FeO remains high-spin to at least 143 GPa.

Unfortunately, these upper limits to the Mott transition pressure in FeO and NiO are at the limit of what is achievable in a diamond-anvil cell. Although pressures exceeding 5 MBar have been reported (see Sec. 3.1), only a small number of experiments work at these extreme pressures due to the very small sample sizes required to achieve those kinds of pressures. MnO is the lightest of the Mott insulating transition metal monoxides. Since the electron correlations increase with increased d orbital filling, it is possible that the Mott transition pressure for MnO is lower than for FeO and NiO. For this reason, we chose to study the high pressure properties of MnO in search of the Mott transition in the transition metal oxides.

Ambient Pressure Properties

At ambient pressure and temperature MnO is an antiferromagnetic (AFM) Mott insulator with a Néel temperature of 118 K [31]. At $T = 300$K it takes the $B1$ rocksalt structure, shown in Fig. 2.2(a). This can be considered as a six layer structure made up of hexagonal layers of Mn^{2+} and O^{2-} ions in the arrangement A(Mn)b(O)C(Mn)a(O)B(Mn)c(O). This layered structure is is illustrated in Fig. 2.2(b) along the (111) direction. Below T_N, MnO undergoes a rhombohedral distortion along the (111) direction, taking the $dB1$ structure, as a result of the AFM arrangement. The classic AFM ordering in these rocksalt materials consists of planes of metal ions, which order ferromagnetically, that are coupled antiferromagnetically with the next metal layer. This inter-planar AFM interaction causes either a slight attraction or repulsion between planes resulting in a rhombohedral distortion of the cubic lattice along the (111) direction.

Behavior at High Pressure

An x-ray diffraction study was published in 2000 by Kondo *et al.* that described the ambient temperature structural behavior of MnO to 137 GPa as understood at the time [4]. Figure 2.3 reprinted from Ref. [4] summarizes this work. With increasing pressure MnO develops a rhombohedral distortion along the (111) direction at 39.4 GPa resulting in a transition to the $dB1$ structure. This kind of structural distortion is associated with the presence of antiferromagnetic (AFM) order in the transition metal monoxides (see above). The transition at 39.4 GPa in MnO is therefore interpreted as being the result of a pressure-induced increase in T_N.

Above 120 GPa MnO was found to take the $B8$ structure, another layered hexagonal structure also found in FeO at high pressure [4]. Similar to the six layer $B1$ structure at lower pressure, the $B8$ (NiAs) structure can be thought of as a four layer hexagonal

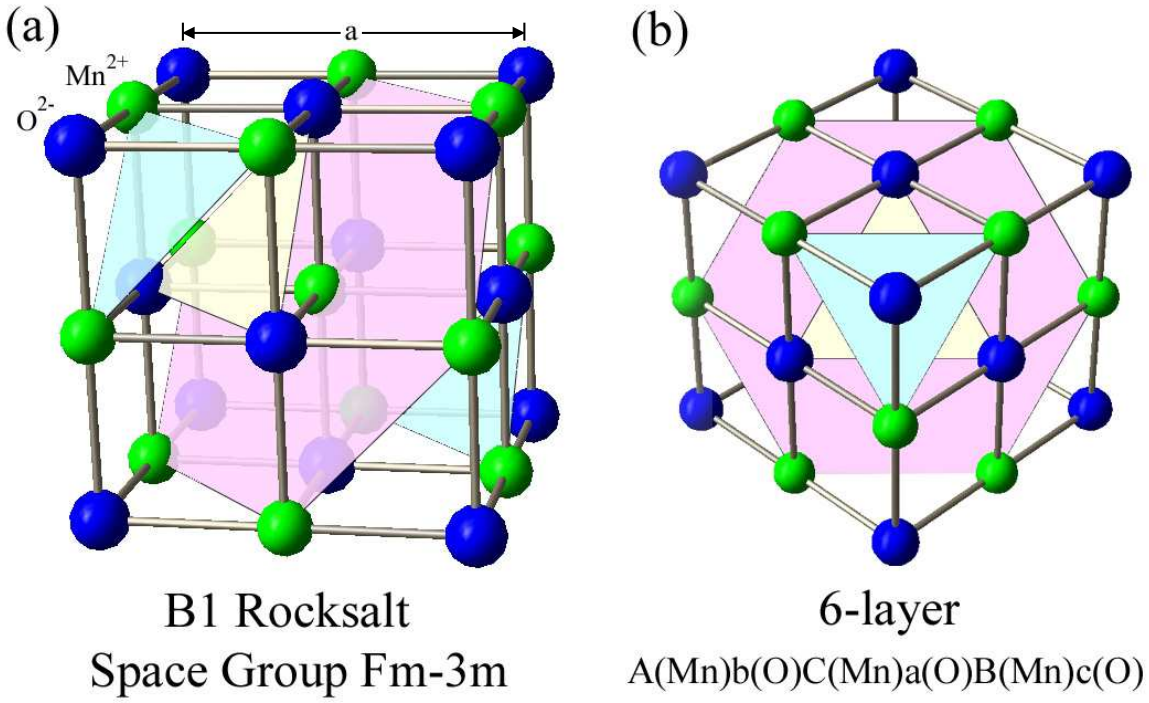

Figure 2.2. (a) shows an isometric view of MnO at ambient pressure and temperature ($B1$ structure, Space group $Fm-3m$) with lattice constant $a = 4.445$ Å. (b) shows an alternative view along the (111) direction illustrating the underlying six layer hexagonal structure in $B1$ MnO.

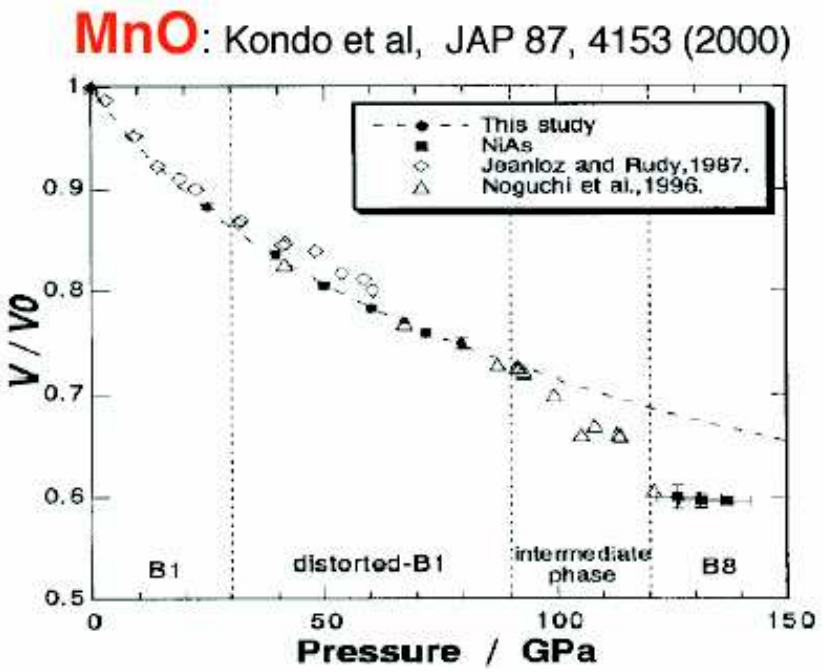

Figure 2.3. Figure taken from Ref. [4] summarizing high pressure structure of MnO to 137 GPa at $T = 300$K as understood at the time (2000). The intermediate phase at 90 GPa was not understood. It was noted, however, that diffraction lines from both the $dB1$ structure and the $B8$ structure were present in the diffraction pattern.

structure with the sequence A(Mn)b(O)A(Mn)c(O). Between 90 and 120 GPa an unknown "intermediate" phase was reported for MnO. The diffraction pattern in this region showed lines from both the lower pressure $dB1$ and the higher pressure $B8$ structure. Unfortunately, it was determined that a larger number of diffraction lines was needed to uniquely identify the structure. Nevertheless, it was stated that the sample clearly showed a "metallic luster" above 90 GPa.

Since the Mott transition in MnO should be accompanied by an insulator→metal transition, a direct measure of the resistivity of MnO under static high pressure was performed in 2004 by Patterson *et al.* at $T = 300$K using designer diamond anvil technology [5]. Figure 2.4 shows a reprint of their resistance data obtained up to 106 GPa. Four probe electrical resistivity measurements uncovered a five order-of-magnitude reduction in the resistance of their sample by 103 GPa. Temperature cycling at 106 GPa confirmed a positive, roughly linear response of the resistance with temperature. They interpreted their results as a metallization occurring around 90 GPa, the same pressure as a previously reported transition to an unknown intermediate phase. As a result, it was unclear whether the metallization seen in their study was indeed due to a Mott transition, where pressure drives the ratio U/W to the itinerant state, or due to a simple change in crystal structure.

Questions

There are a number of unanswered questions regarding the high pressure behavior of MnO. Despite repeated efforts, the Mott transition has yet to be seen in the transition metal monoxides, including MnO. The drop in resistance of MnO observed by Patterson *et al.* [5] could be an indication of a Mott transition, however more work is required to make an unambiguous identification. In addition, the crystal structure of MnO at high pressure is not fully understood, especially in the "intermediate phase" region from 90 to 120 GPa.

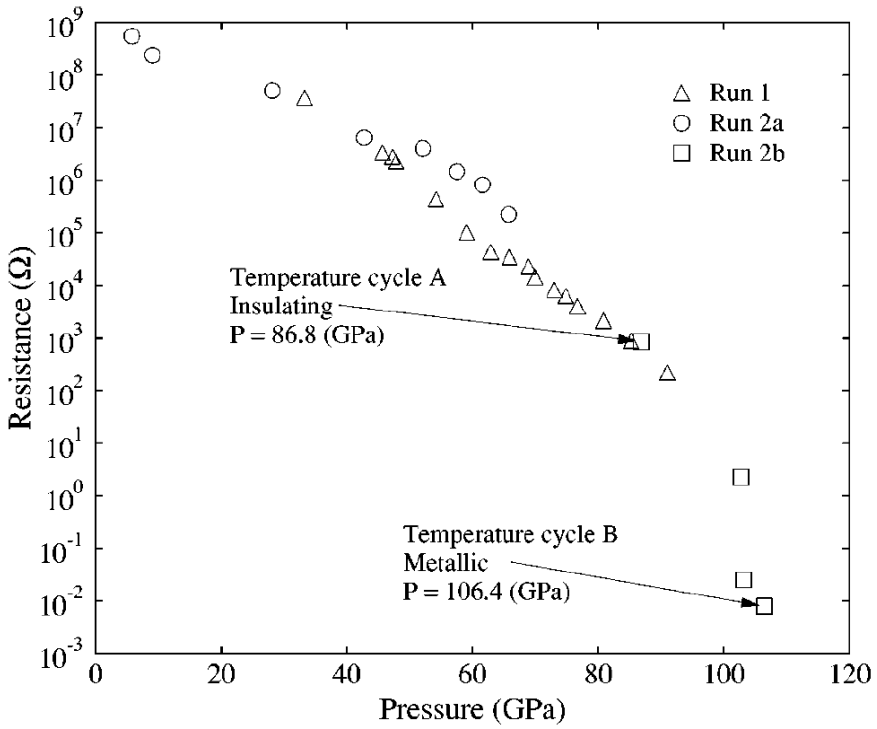

Figure 2.4. Figure taken from Ref. [5] showing a five order-of-magnitude drop in resistance of their MnO sample by 103 GPa.

We therefore set out to answer the following questions:

1. What is the crystal structure of the reported "intermediate" phase between 90 and 120 GPa?
2. Was the drop in resistance reported by Patterson *et al.* [5] the result of a Mott transition or a simple change in crystal structure?
3. At what pressure (if any) does MnO undergo a Mott transition?

2.2.2 Ce, Pr, Nd, and Gd

High Pressure Structural Review

The high pressure structural properties of the $4f$ metals, with the exception of the divalent metals Eu and Yb, are dominated not by the $4f$ electrons but by the $5d$ electrons, which lie farther from the nuclear core and are primarily responsible for bonding. They all share the common structural sequence $hcp \rightarrow Sm\text{-type} \rightarrow dhcp \rightarrow fcc \rightarrow d\text{-}fcc$ at high pressures (See Fig. 1.1 reprinted from Ref. [3]). This exact same sequence is observed in the $4d$ metal Y, which has no nearby f states [32]. The effects of pressure on the valence electrons can be mimicked by reducing the atomic number [33]. Therefore, the lighter rare-earths begin this structural sequence at a later stage at ambient pressure.

The rare-earths Ce, Pr, and Gd undergo volume-collapse transitions (VCTs) at 7 kbar [34], 20 GPa [35, 36], and 59 GPa [37] at ambient temperature, respectively. Cerium metal, which starts the above mentioned structural sequence with fcc $\gamma-$Ce at ambient pressure, undergoes an isostructural VCT where the atomic volume shrinks by 15% but retains the fcc structure. This same transition to α-Ce can be induced by lowering the temperature at ambient pressure. The metals Pr and Gd, which start with the *dhcp* structure and *hcp* structures at ambient pressure, undergo volume collapses of 10% and 5% respectively. Unlike Ce, however, these metals terminate the structural sequence with a complex, low symmetry structure immediately following the volume collapse. In Pr metal,

this collapsed phase has been shown to take the α-U structure. Nd, which also starts the structural sequence at *dhcp*, reaches the same α-U structure but without a measurable volume-collapse.

Electronic and Magnetic Structure

At ambient pressure, the $4f$ electrons in Ce, Pr, Nd, and Eu form very narrow, localized bands due to $f - f$ correlations. As a result, the $4f$ electrons form strong Hund's rule moments. At low temperature, these moments order ferromagnetically through an RKKY interaction. Because the $4f$ electrons are highly localized, the orbital overlap is small. However, they can develop long-range order by indirectly interacting with each other via the valence electrons.

Positron annihilation experiments performed in 1969 by Gustafson *et al.* were aimed at measuring the change in valence of cerium through the VCT at high pressure, and also at low temperature. The experiment was designed to test the promotional model, proposed by Coqblin *et al.* in 1968 [19], which described the VCT in Ce as a promotion of the $4f$ electron to the valence orbitals. An analysis of the width of the angular correlations in the positron annihilation experiments indicated the presence of trivalent Ce in the collapsed α phase. This disproved the promotional model which predicted a transition to tetravalent, or Ce^{4+}, through the collapse.

Magnetic susceptibility measurements in 1978 across the γ-α VCT in Ce showed the temperature dependence change from Curie-Weiss behavior to a temperature-independent Pauli-paramagnetic behavior [38]. The Curie-Weiss law describes the temperature dependence of a ferromagnetic material above the Curie point as $\sim 1/(T - T_c)$ and indicates the presence of local moments. Since the magnetism in the rare-earths is due to the $4f$ electrons and the RKKY interaction mediated by the valence electrons, the switch to Pauli-

paramagnetic behavior in the collapsed phase was significant and seemed to indicate a loss of the magnetic moment in the collapsed phase of Ce. This result supported the idea that the γ-α VCT transition in Ce was indeed a Mott transition [20], which requires the loss of the local moment of the $4f$ electrons due to a change in $f - f$ correlation.

However, a photoemission experiment in 1981 by Croft *et al.* [22] on "chemically compressed" Ce alloys seemed to contradict the results from magnetic susceptibility obtained a few years earlier. These results indicated not only that the binding energy of the $4f$ electron was much too large for $4f$ promotion (this value needs to be ~ 0.1 eV in the promotional model, compared to the experimentally determined value of 2 eV) but also that the position and width of the $4f$ density of states was, for the most part, volume independent. This latter point was in disagreement with the Mott transition model which relies on the broadening of the narrow $4f$ band and the eventually overlap with the unoccupied $4f$ band.

In 2005, a high energy neutron scattering of Ce at experiment performed at low temperature on the collapsed phase of Ce also seemed to contradict the susceptibility measurements on Ce by comparing the experimentally determined magnetic form factor as a function of scattering vector with theoretically calculated form factors for Ce^{3+}, with a well localized $4f$ moment, and for Ce with an itinerant $4f$ band [39]. The results showed that the experimental form factor matched best with that of Ce^{3+} and indicated that the collapsed phase of Ce retained a strongly localized $4f$ electron, a result that supported the Kondo VCT model.

Questions

The above mentioned experimental work leaves a serious question as to whether the $4f$ electrons stay strongly localized, as in the Kondo VCT model, or delocalize, as in the

Mott transition, across the $\gamma - \alpha$ VCT transition in Ce. Recent theoretical investigations only serve to complicate matters by showing that the two models used to describe the Kondo VCT scenario and Mott transition scenario, namely the Anderson impurity model and the Hubbard model, both reproduce the spectral features associated with Kondo screening, a hallmark of the Kondo VCT model [23]. We are left with the following question:

1. Which model, the Mott transition model or the Kondo VCT model, is appropriate to describe the changes in electron correlation in the rare-earths?

2.2.3 CrO_2

Half-Metallic Ferromagnet

Chromium dioxide (CrO_2) has many properties of interest to both the scientific community and industry. Due to its relatively high coercivity, CrO_2 was introduced as a magnetic recording media in 1974 and quickly became the most widely used medium in audio cassette tapes. At ambient pressure, CrO_2 is a ferromagnet with a Curie temperature of $T_c = 390$ K. However, little was known about its electronic structure despite its widespread use in the recording industry. The first model of the electronic structure of CrO_2 was proposed by Goodenough [40]. But, it was not first principles calculations by Schwarz [41] in 1986 that CrO_2 was correctly predicted to be half-metallic.

A schematic view of this half-metallic electronic structure is shown in Figure 2.5. In CrO_2 the Cr atoms have a charge of roughly 4+ making them d^2 Cr^{4+} ions. The octahedral arrangement of O^{2-} ions around each Cr^{4+} ion splits the five-fold degenerate $d-$orbitals into a lower energy three-fold degenerate t_{2g} orbital and a higher energy, doubly degenerate e_g orbital. This splitting is shown in Fig. 2.5 as ΔE_{cf}. The d-d exchange interaction produces a local moment on the t_{2g} orbital by splitting the spin up and spin down $d-$orbitals by an amount ΔE_{ex}. Normal ferromagnetic metals such as Ni and Co also

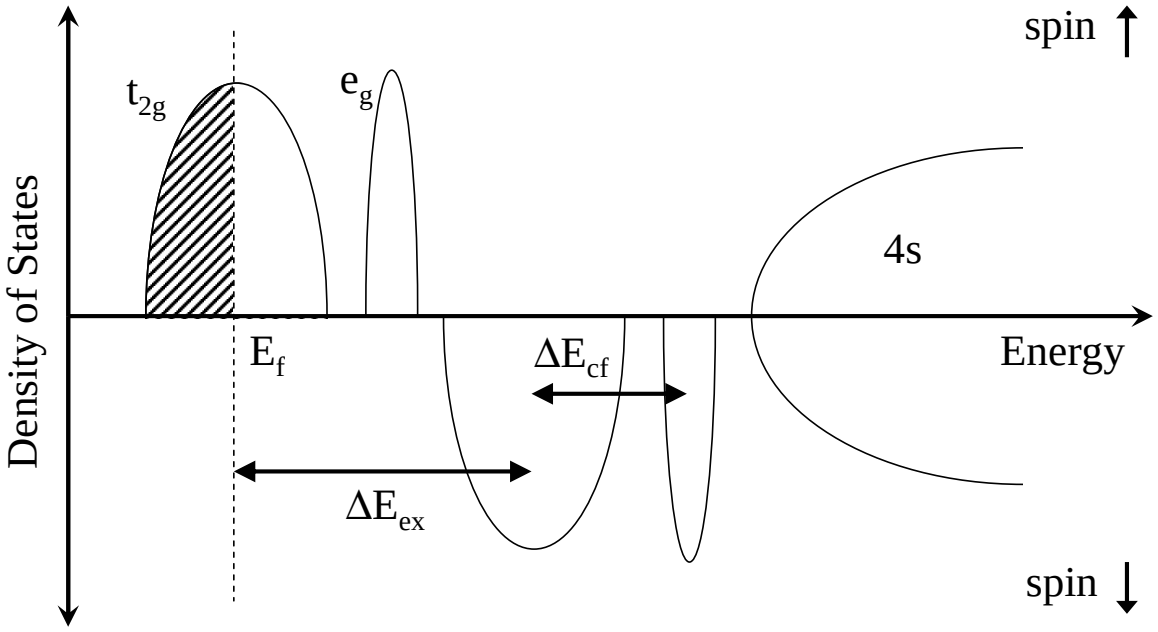

Figure 2.5. A schematic representation of the d-density of states of d^2 CrO_2 showing how the half-metal behavior arising as a result of the strong exchange splitting ΔE_{ex}. The splitting ΔE_{cf} is due to the octahedral crystal field surrounding the Cr^{4+} ions.

have fully spin-polarized $d-$bands. However, these materials are not half-metals because the Fermi level also crosses the $4s$ band which introduces a finite number of spin up and spin down carriers. To form a half-metal it is necessary to raise the energy of the $4s$ band above the Fermi level through hybridization. This is why all half metals are compounds and not pure elements. In CrO_2 the $Cr(4s)$ states hybridize with the $O(2p)$ state pushing them well above the Fermi level, as shown in Fig. 2.5.

An initial photoemission experiment by Kämper *et al.* in 1987 [42] at ambient temperature quickly confirmed a near 100% spin polarization of the $3d$ band 2 eV below E_F. However, they found no spectral weight at the Fermi level, in contradiction with the metallic nature of CrO_2. A later experiment by Tsujioka *et al.* [43] confirmed the metallic nature, but it was not until 2001 that Strijkers *et al.* [24] used point-contact Andreev reflection to accurately determine a spin polarization of 0.96 ± 0.01 at E_F. The half-metallic behavior

of CrO_2 also gives rise to relatively low electrical resistivity for an oxide, 300 $\mu\Omega$-cm and hence it is commonly referred to as a "bad metal" [44].

Crystal Structure

At ambient conditions α-CrO_2 crystallizes into the rutile structure, space group $P4_2/mnm$, with lattice parameters $a = b = 4.421$ Å and $c = 2.916$ Å and atomic positions of Cr(2a) at (0,0,0) and O(4f) at (u,u,0) with $u \sim 0.301$ [11]. The rutile structure, shown in Fig. 2.6(a)(b), consists of chains of distorted edge-sharing CrO_6 octahedra along the c-axis with the Cr ions forming a body-centered tetragonal lattice. This distortion can work to either flatten (apical bonds are shorter than the equatorial bonds) or elongate (apical bonds are longer than the equatorial bonds) the CrO_6 octahedra along their axes. The positions of the oxygen atoms are determined by the fractional coordinate u which sets the Cr-O distances and determines the size and nature of the distortion. At the ambient pressure values of a, b, c, and u the oxygen octahedra are flattened along the apical direction with Cr-O distances of 1.882 Å and 1.917 Å for the apical(2) and equatorial(4) lengths, respectively.

The rutile structure, a structure commonly found in many metal dioxides (MO_2; M = Ti, Cr, Mn, Sn, Ge, Pb, etc.) makes CrO_2 one of the simplest known half-metals. The rutile structure consists of tetragonally distorted edge-sharing MO_6 octahedra (see Fig. 2.6(a)), one of the most fundamental building blocks of covalently bonded network structures found in hard materials and earth minerals like stishovite. Larger metal ions, (*i.e.*, M = W, Re, Mo, etc), however, tend to form an eight-fold coordinated CaF_2 structure while smaller ions (M = C, Si, etc.) crystallize into a four-fold coordinated tetrahedral structure. At high pressures, the rutile structure typically transforms to another six-fold coordinated structure, $CaCl_2$, or the α-PbO_2 structure found in shock compressed SiO_2 and known as a post-stishovite structure [45]. The smaller four-fold coordinated SiO_2 transforms into

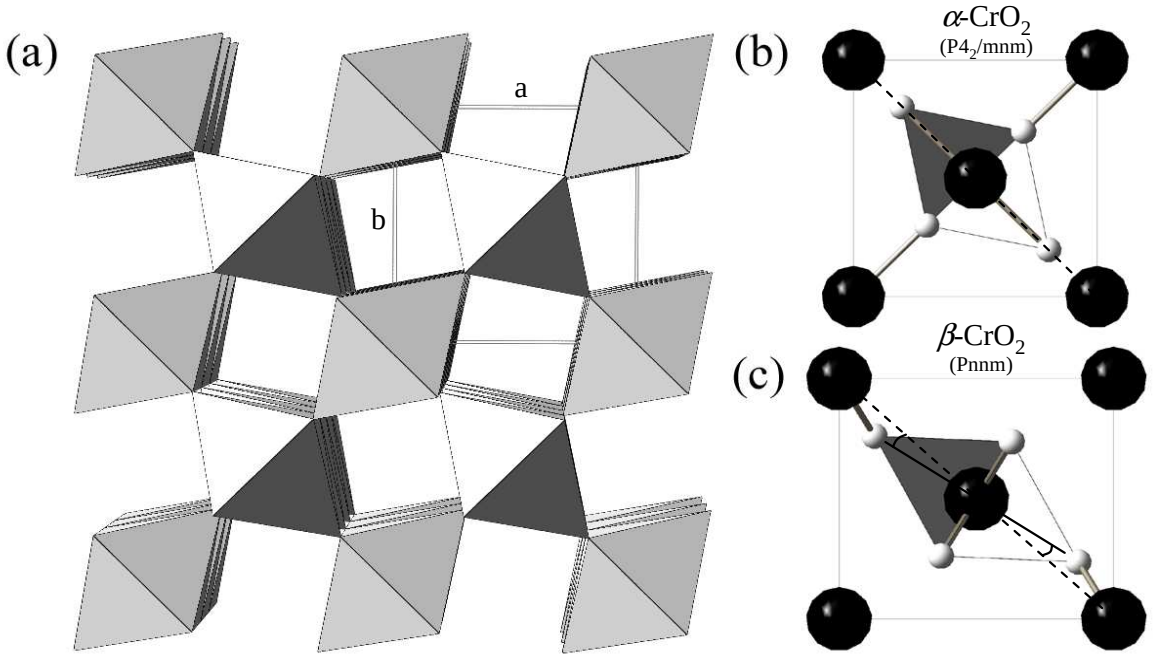

Figure 2.6. (a) The edge-sharing octahedra of the rutile structure along the c-axis. (b) Shows rutile-structured α-CrO_2 ($P4_2/mnm$, $Z = 2$, $a = b = 4.421$ Å $c = 2.916$ Å $u = .301$) at ambient conditions projected onto the ab-plane with Cr^{4+} ions in black and O^{2-} ions in white. (c) Shows β-CrO_2 (Pnnm, $Z = 2$, $a = 4.425$, $b = 3.987$, and $c = 2.683$, and $u_x = 0.371$ and $u_y = 0.263$) at 50.4 GPa. The transition from α-CrO_2 to β-CrO_2 involves an orthorhombic distortion and a rotation of the CrO_6 octahedra about the c-axis (see Sec. 4.3.1).

the six-fold rutile structure, stishovite. Therefore, to first approximation these pressure-induced structural transitions may be understood in the simple view of topological packing of hard spheres, i.e. an increase in the coordination number and the associated electrostatic interaction at high densities. At high pressures, however, the electronic structure also changes in a significant way and so does the nature of electron interaction. As a result, the characteristics of these MO_2 transitions could be more complex than is evident from their rather continuous manner, occurring without any structural or volume discontinuity. The rutile structure has even been found in the molecular solid CO_2-II at high pressures and temperatures [46]. Furthermore, the electronic contribution to structural stability is significant in transition metal oxides at high pressures, as is evident from the Mott insulator-metal transitions [5, 47] charge transfer transitions [48], valence transitions, etc.

Questions

As previously mentioned, the electronic structure of a material has significant influence on its physical and structural properties. Because CrO_2 is the only rutile-structured dioxide that is half metallic, its behavior at high pressure may significantly deviate from the behavior of other rutile-structured dioxides. In addition, because one spin channel is insulating in a half metal it is possible that the application of pressure could induce a half-metal to metal transition where the Fermi level crosses the edge of the minority spin band edge. Therefore, we set out to answer the following questions:

1. What are the high pressure phase/phases of CrO_2?
2. What effect, if any, does the half-metallic character of CrO_2 have on its physical properties at high pressure?
3. Does CrO_2 undergo a half-metal to metal transition at high pressure? If so, what effect does this transition have on the physical properties of CrO_2?

Chapter 3

Experimental Methods and Materials

3.1 High Pressure Techniques

Very high static pressures can be generated by applying a force over a very small area. This is the fundamental principle of all static pressure devices and directly follows from the definition of mechanical pressure $Pressure = Force/Area$. The first pressure devices used tapered "anvils" made of hard metal alloys such as steel or tungsten carbide. The sample to be studied was placed between the anvils and a force applied, forcing the anvils together. However, these devices were large and the anvils opaque. This limited experiments to non-optical ones such as resistance measurements or temperature measurements. It wasn't until the introduction of x-ray transparent anvils such as Be that structural measurements and phase determination were possible. The introduction of diamond to high pressure research in 1950 [49] and the invention of the diamond anvil cell (DAC) in 1959 [50] allowed optical experiments as well as x-ray diffraction.

The modern piston-cylinder DAC is capable of generating pressures exceeding 5 MBar [51] and was used in all experiments described in this work. Figure 3.1 illustrates the basic construction and operation of the DAC. The applied load, shown as white arrows, is transferred to two opposing diamond anvils whose tips have been polished flat to form circular culets. The diamonds are supported by sufficiently strong seats. These seats are typically made from tungsten carbide (WC), however beryllium (Be) and pressed cubic boron nitride (c-BN) are sometimes used when a low-Z, x-ray transparent seat is desired. The sample is positioned between the opposing anvils, in the center of the culets, and held in place by a gasket. The gasket also acts to support the sides of the anvils, increasing the maximum pressure above that obtained by dividing the total applied force by the sample area [52]. Along with the sample, a pressure transmitting medium such as mineral oil or Argon and a pressure calibrant are often placed inside the sample chamber. Typical culet diameters range from 500 μm to 50 μm, the smallest culets being required to achieve pressures in excess of 1 MBar.

3.1.1 Types of Pressure Cells

One important consideration in the design of any DAC is the diamond culets must remain as close to parallel as possible in order to achieve the maximum possible pressure. Early designs used hemispherical seats that allowed independent adjustment of each diamond anvil to correct for imperfections in the seat construction. However, modern machining techniques have rendered this all but obsolete. Most cells now employ tapered cylinder seats made of WC. Another equally important consideration is the diamond culets must be aligned and stay aligned as the load is increased to prevent premature failure of the diamond anvils or loss of sample containment. All cell designs use a number of set screws to position the diamonds and diamond seats so that the two diamond culets are

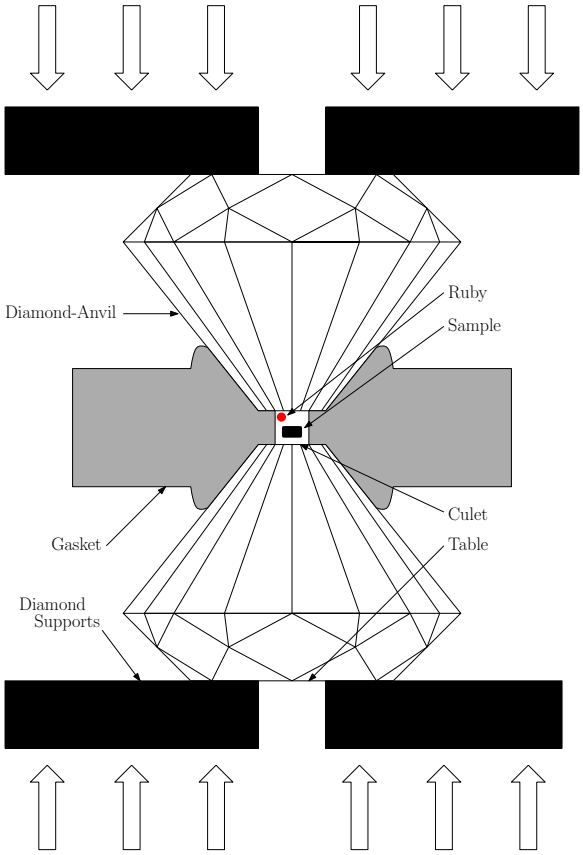

Figure 3.1. Schematic view showing the major parts of the diamond-anvil cell (DAC). The DAC is composed of two opposing diamond anvils whose tips were polished into flat culets. Between the culets is a metal gasket with a hole drilled down the center. A sample is placed inside this hole, typically along with a pressure transmitting medium and a pressure calibrant (in this case a Ruby chip). The diamonds are supported by seats typically made of tungsten carbide (WC). The white arrows show the direction of the applied load.

aligned along the axis of the cell. To keep the cell from shifting under applied load, cells like the triangular Merril-Basset cell use a guide pin arrangement [53]. However, for the highest pressures, the piston-cylinder design is considered the most effective. All cells used in this work were piston-cylinder style DACs designed by the High Pressure Physics Group at LLNL.

All experimental techniques used in this study are photon in/photon out experiments. However, each technique probes the sample using a different range of photon energies. The specific energy range and experimental geometry of each technique determined which DAC was used. All experiments performed in this study used one of the cell designs described below.

LLL Cell

Experiments requiring access to the sample either along the DAC axis (through the diamond anvils) or at exactly 90° from the DAC axis (through an x-ray transparent gasket) were conducted using a *LLL* cell. These experiments include Raman spectroscopy, which uses photon energies in the optical range, and all synchrotron x-ray experiments (with the exception of Eu x-ray emission spectroscopy. See Sec. 3.1.3). This cell has a relatively long body ($\sim$ 2.375") to prevent the piston from rocking too much inside the cylinder, destroying the alignment of the diamond culets. Four, equally spaced, 7 mm diameter ports are located around the sample allowing access to the sample from the side (through an x-ray transparent gasket). The cylinder end of the cell has a slot opening for collecting x-ray diffraction spectra or Raman signal. This slot provides a $\sim$30° opening in the vertical direction and $\sim$45° in the horizontal direction, depending on the height of the WC seat and the diamond anvil. Alignment of the diamond culets is accomplished by setscrews located on the piston and cylinder parts of the cell. The pressure at the sample chamber is

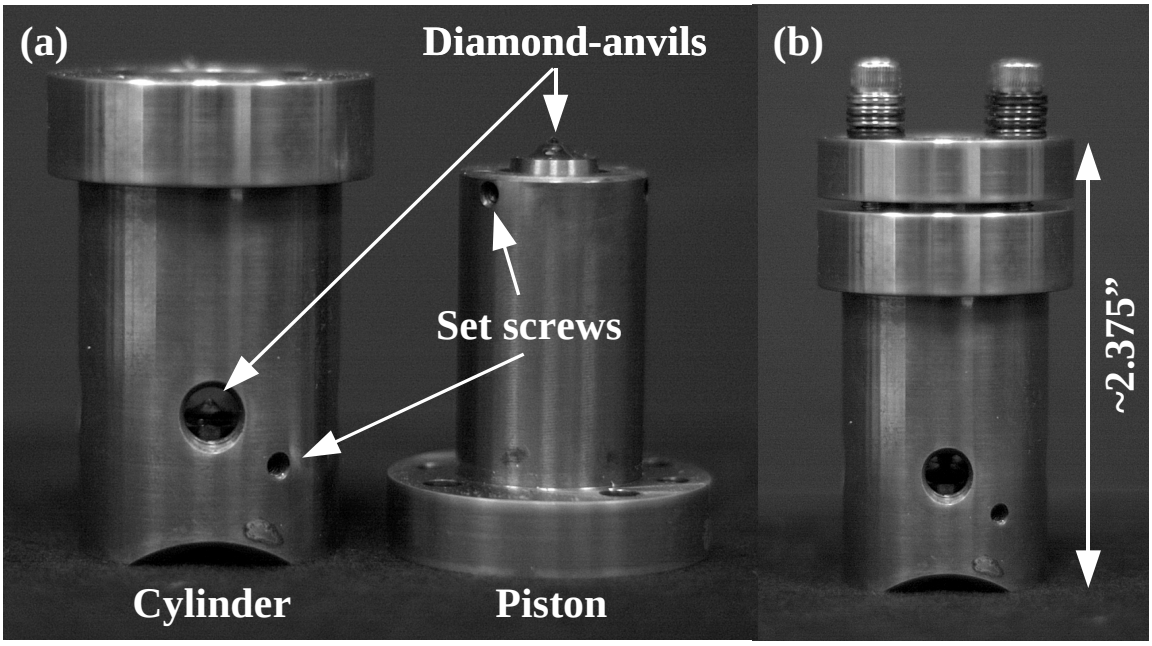

Figure 3.2. A picture of the *LLL* cell with diamonds (mounted on WC seats). The pressure is varied using four 6/32” screws. Access to the side of the sample (through an x-ray transparent gasket) is provided by four 7 mm ports spaced evenly around the cell. A slot opening on the anvil end of the cell provides access to the sample along the DAC axis of roughly 30° in the vertical direction and 45° in the horizontal direction (depending on the height of the WC seats and the diamond anvil).

varied by turning four 6/32” screws located at one end of the cell. Spring washers are used between the screws and the piston ($\sim$ 6 washers per screw), allowing for greater control when adjusting the pressure by requiring a greater number of turns to apply a given force.

SAX Cell

Experiments requiring access to the sample area at angles far from 90° employed a *SAX* cell, shown in Fig. 3.3(a). Alignment of the diamonds and the application of a load are accomplished in the same manner as the *LLL* discussed above. However, this cell has a longer body than the *LLL* cell to accommodate a very large 90° opening on the side, as shown in Fig. 3.3(b). Unfortunately, the remaining port holes on the side of the cell at

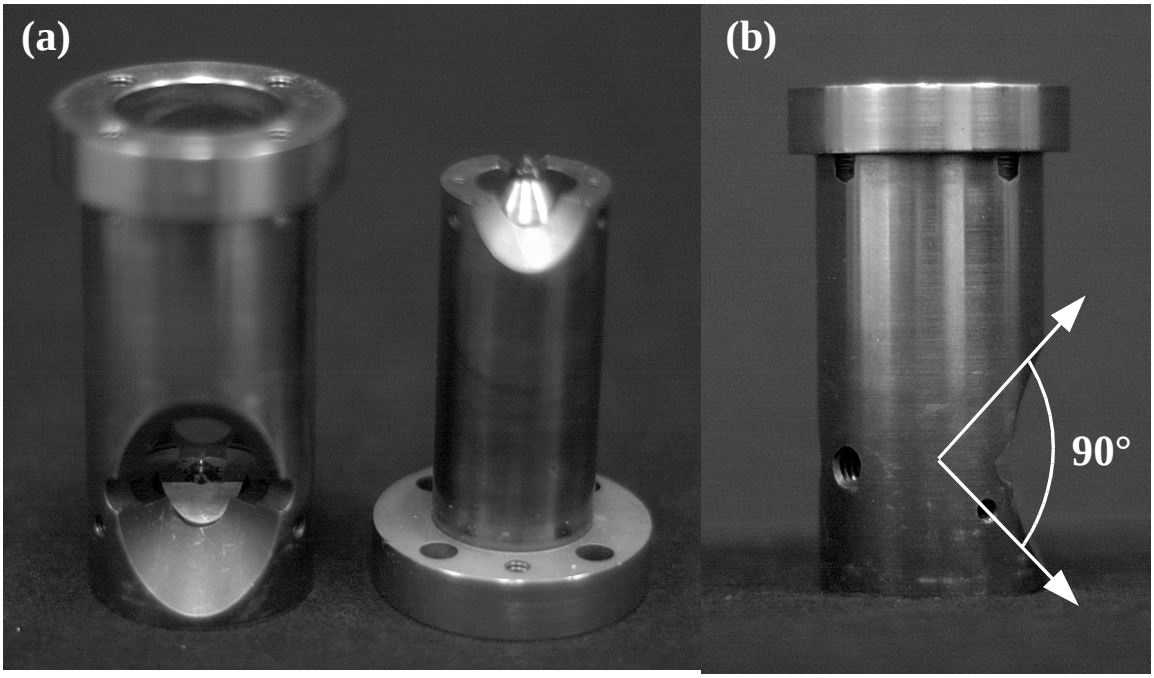

Figure 3.3. A picture of the *SAX* cell with diamonds (mounted on WC seats). The piston-cylinder arrangement is similar to the *LLL* cell shown in Fig. 3.2, with three set screws on each side for alignment and four 6/32" screws for varying the pressure. In addition to the standard slot-type opening at the end of the anvil side, the *SAX* cell has a 90° opening on the side of the cell for experiments that require access to the sample through the side at angles far from 90° (see Sec. 3.1.3).

90° are quite small. This limits this cell to experiments where the probe beam is along the axis and the signal is measured either out the slot at the end of the cylinder, as in Raman spectroscopy or x-ray diffraction, or out the large angle opening. For these reasons, this cell was only used for Eu x-ray emission spectroscopy (see Sec. 3.1.3).

3.1.2 Metallic Gaskets

Metallic gaskets for use in high pressure experiments were introduced by Alvin Van Valkenburg, one of the inventors of the DAC, in 1962 [54]. Prior to this time, only solid samples could be measured and were usually pressed between the two diamond culets into thin foils. Researchers also discovered that placing a sample in a metallic gasket and

surrounding the sample with a pressure-transmitting medium would produce hydrostatic conditions within the sample chamber DAC. By pre-indenting the gasket between the diamond anvils, the maximum achievable pressure could be increased due to the support provided by the plastic flow around the diamonds (see Fig. 3.1) [52]. In general, materials with a high compressive strength (bulk modulus) and sufficient coefficient of friction are used as gasket materials [52].

High-Z Metals

Stainless Steel foil (T301 alloy), with a bulk modulus of $B_0 = 160$ GPa, is commonly used for relatively low pressures ($<<$ 1 MBar) where the thickness of the sample is not a factor. For higher pressures or experiments where thick samples are desired, Rhenium (Re) foil ($B_0 = 371$ GPa [55]) is the most common gasket material and was used for all x-ray diffraction and Raman spectroscopy experiments in this study (also used for Eu x-ray emissions spectroscopy. See Sec. 3.1.3).

Beryllium

When access to the sample through the gasket is required, as in inelastic x-ray scattering, an x-ray transparent gasket is needed. Beryllium (Be) metal is the strongest of the low-Z metals (Z=4) and is used in many industries, such as the aerospace industry, when a low weight, high strength material is needed. Fig. 3.4 shows the relative transmissions for Be, Diamond, and Re at 2.5 mm, which is the height of most diamond-anvils and is also the radius of the standard Be gaskets used. Also shown are the energies of Mn $K\beta$ emission, the L_{III} edge of Gd, and the M_V absorption edge of Gd. Be is the only material which shows any appreciable transmittance through 2.5 mm at the energies of $K\beta$ emission and the L_{III} edge. The M_V absorption, which is commonly used to probe the unoccupied

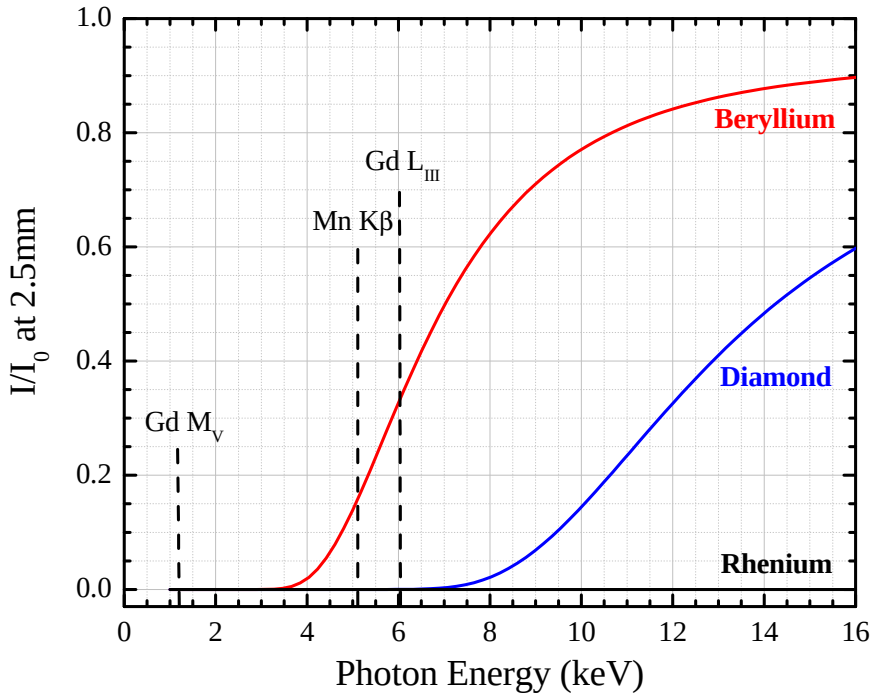

Figure 3.4. Relative transmission, I/I_0, for Be, Diamond, and Re through 2.5mm. Dashed vertical lines show energies of various x-ray emissions and absorptions studied in this work.

$4f$ levels in rare-earths, is too low in energy to penetrate any of these gasket materials and is therefore unsuitable for study at high pressure. The transmission through Rhenium metal is zero at all energies in this range. Thus, Be was used as the gasket material for all inelastic x-ray scattering experiments described in this study, with the exception of Eu x-ray emission spectroscopy (see Sec. 3.1.3).

Metal Gasket Preparation

Before a sample can be loaded into the gasket, one must be first pre-indent the gasket using the DAC. This is because the region of gasket materials outside the culet area contributes significantly to the ability of the gasket to generate and hold pressure [52]. Reference [52] also points out that a sample hole in a thick gasket will tend to expand. If the gasket is too thick it can "blow out" (the edges of the sample hole extend beyond the

culet), losing containment of the sample and putting the diamonds in jeopardy of touching. It is therefore recommended that the gasket be pre-indented with a force close to the final force that will be placed on the sample. In practice, for diamond culet diameters of 300 μm or less, the gaskets are pre-indented to a pressure of $\sim$ 25 GPa. For Re, this yields a thickness at the culet flat of around 25 μm. For larger culets (500 to 700 μm an indentation pressure of about 10 GPa is sufficient.

A sample hole is created by an electric discharge machining (EDM) device using copper wires of varying diameter as the drilling tool. The starting sample hole size is critical. A hole that is too large will cause undesired effects including a reduction in pressure with applied load which can cause premature diamond failure [52]. Therefore, a sample hole of radius $r_g \leq r_0/2$, where r_0 is the radius of the culet, is traditionally employed. It should be noted that because Be is a known carcinogen, special precautions must be taken to avoid contact with Be dust. These precautions include drilling under a fume hood and using copious amounts of dielectric fluid. In addition, the entire work area should be decontaminated and any Be debris created during the drilling process should be treated as Hazardous waste.

Impurities

The Be stock traditionally used for making gaskets contains transition-metal impurities that can cause problems when doing IXS experiments. For example, Eu Lγ_1 x-ray emission occurs at 7480.3 eV while the much stronger Ni Kα_1 x-ray emission occurs at 7478.15 eV [56], a separation of only 2.15 eV (see Secs. 4.2.2 and 6.4.1). Table 3.1.2 gives the impurity levels quoted from the manufacturer (Brush Wellman) of the standard Be stock showing levels of 400 ppm of Ni. If the Ni impurity concentration is too high, x-ray emission signal from Ni can overwhelm the relatively weak emission from Eu.

	Standard Be (I-250) (ppm)	High-Purity Be (IF-1) (ppm)
Be Purity	97.0%	99.74%
BeO	<25,000	200
Fe	<1500	60
Mg	600	5
Al	100	25
C	1500	800
Si	600	25
Cr	400†	5
Co	400†	<3
Cu	400†	5
Pb	400†	<5
Mn	400†	5
Mo	400†	<10
Ni	400†	30
Ca	400†	<20
Zn	400†	<10
Ag	400†	<3
Ti	400†	<5

Table 3.1. The level of various impurities measured in parts-per-million (ppm) for the standard Be gaskets (I-250, Brush Wellman) and for high-purity Be foil (IF-1, Brush Wellman). †Manufacturer quotes 400 ppm "other impurities" which includes Ni and Cu.

A striking example of this impurity problem is demonstrated by the $L\gamma_1$ XES spectrum of Pr shown in Fig. 3.5. The blue curve shows the XES spectrum obtained from a Pr sample loaded in a LLL cell using a standard Be gasket (Brush Wellman I-250). The peak at 6322 eV represents the main $L\gamma_1$ emission line (see Sec. 3.2.3). The strong peak at 6298 eV occurs at the same energy as the expected $L\gamma_1'$ satellite peak but is much more intense than expected, as shown by the red curve taken from an ambient pressure Pr ingot (no cell). The black curve in Fig. 3.5 shows an XES spectrum from the side of a standard Be gasket, far removed from the sample region. This series of spectra clearly demonstrate the presence of a contaminate in the Be gasket interfering with the spectrum from our sample.

Be foil can, however, be made with much lower impurity levels. Table 3.1.2 also gives the impurity levels for High-Purity Be foil showing levels of Cu and Ni of only 5 and 30 ppm. This opens the possibility of using high-purity Be foil as a gasket material, eliminating the problem of transition-metal contamination. Unfortunately, the high purity IF-1 grade Beryllium is not strong enough to support high pressure. The I-250 grade of Beryllium commonly used was chosen for its high strength resulting from the numerous impurities. Using the high purity IF-1 grade Be and pre-indenting to 25 GPa using 200 μm culet diamonds yielded a gasket thickness of only 7 μm. This indicated that the gasket thickness at higher pressures would be prohibitively thin and would cause premature diamond failure. Thus, it was necessary to devise new techniques if we wanted to apply $L\gamma_1$ XES to Pr or Eu. These techniques are discussed in Sec. 3.1.3.

3.1.3 Alternative Gasket Techniques

Gasket Inserts

One solution to the impurity problem mentioned in Sec. 3.1.2 is to create a buffer zone between the sample and the Be gasket using a gasket insert. The resulting buffer zone

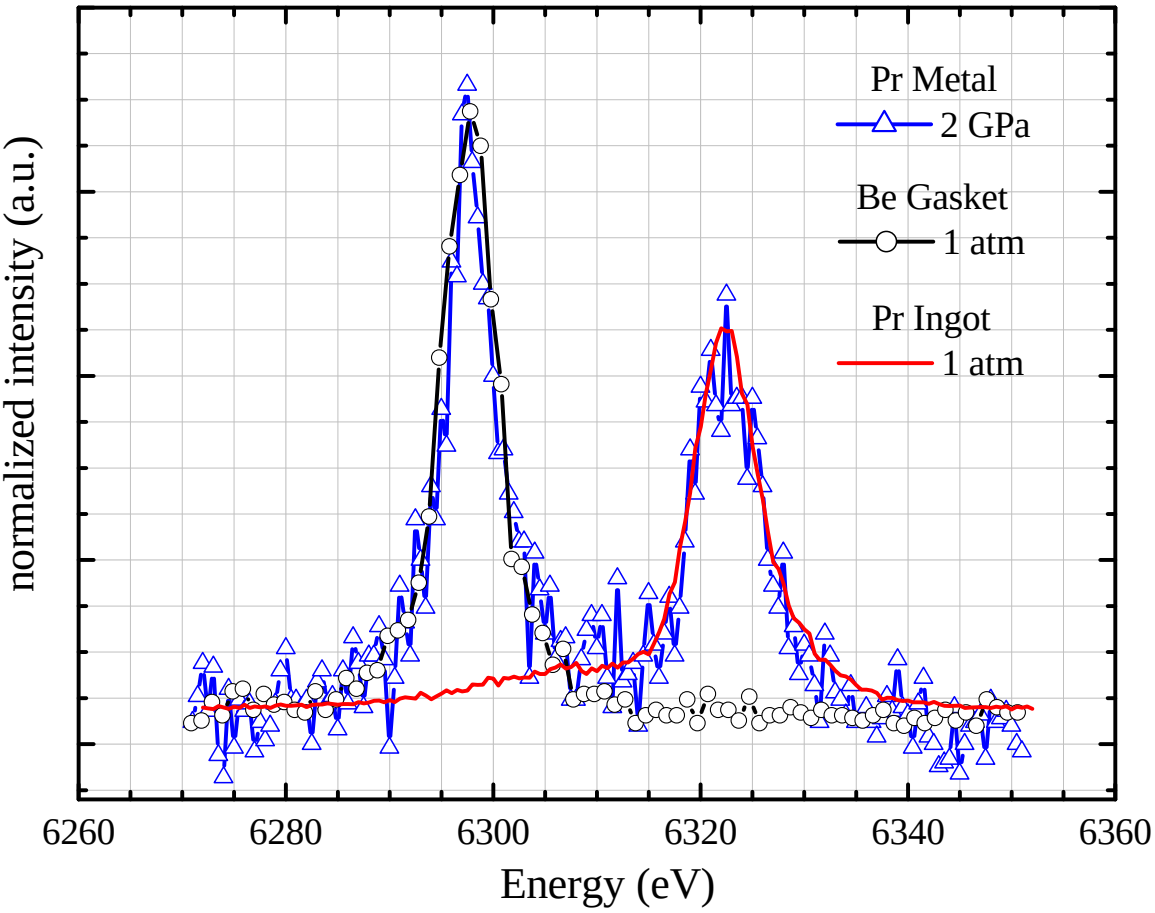

Figure 3.5. $L\gamma_1$ XES spectra of Pr, at 2 GPa (open triangles, taken in DAC) and ambient pressure (solid red line, taken from Pr ingot) showing an anomalous strong peak at 6298 eV from the 2 GPa Pr sample in the DAC. Also shown is an emission spectrum taken on the Be gasket with no Pr present (open circles) showing the same anomalous peak at 6298 eV. Hence, the peak at 6298 eV is from impurities in the Be gasket and not from our sample.

prevents the tails of the incident x-ray beam from clipping the Be. Because the gasket must remain x-ray transparent, a low-Z materials must be used. The material also must be strong. We chose c-BN as the gasket insert material for the following reasons:

1. It is one of the hardest materials known to man (second only to diamond). This is because c-BN has the same structure as diamond and therefore mimics many of its properties
2. It has a low atomic weight (Z=5 for B, Z=7 for N)

Gaskets were prepared by first pre-indenting 10 mil thick high purity IF-1 Be foil. The indentation should be slight, being only deep enough to allow one to use the indentation marks as a guide for drilling. A hole was then drilled in the center of the gasket indentation. The size of the hole depends on the culet diameter. A hole roughly 125% the size of the culet was found to work best. This works out to be 250 μm for the 200 μm culets used in this study.

The hole was then packed with the gasket insert material and pressed between the diamond anvils to form a cold-pressed solid insert. The insert material was prepared by mixing c-BN with an AB epoxy (P/N: 353ND Epotek) in the ratio 4:1 by weight. The mixture was then and allowed to cure at high temperature. The addition of a small amount epoxy ensures that when the material is compressed between the diamond anvils, the particles stick together sufficiently. The gasket/insert assembly was then indented to the same pressure as when using standard metallic gaskets, or around 25 GPa. The final thickness using this method was 19 μm, an increase of $\sim$ 300% over plain high-purity Be foil.

A sample chamber hole was then be created. Because the c-BN + epoxy is non-conducting, the hole was drilled mechanically. For 200 μm culets a hole 80-90 μm in diameter was drilled. Figure 3.6 shows a prepared sample using this insert technique. The 200 μm diamond culets are easily seen as the bright inner region while the outer, darker

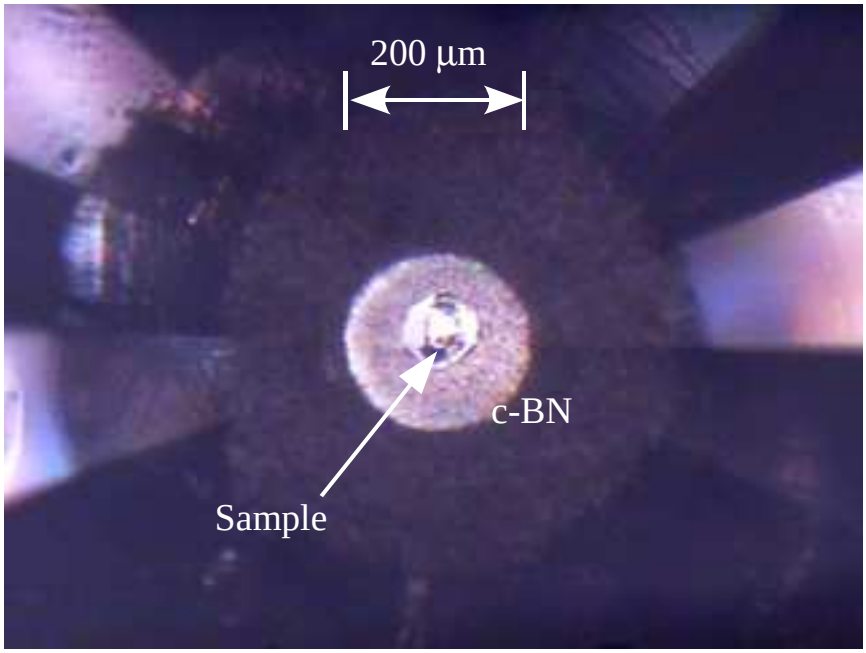

Figure 3.6. Picture of c-BN insert in a high purity IF-1 Be gasket. The bright center marks the 200 μm diamond culets while the darker outer circle shows the extent of the c-BN gasket. The sample is at the center.

region marks the extent of the c-BN insert. The sample hole, sample, and pressure medium are at the center.

Rhenium Gaskets for IXS

An alternative solution to the problem of transition-metal contamination in Be is to eliminate the need for an x-ray transparent gasket and instead use a high-Z metal such as Re. This was accomplished by measuring the outgoing inelastic x-ray scattering signal escaping the sample chamber between the gasket and the diamond anvil. This technique has many advantages over using Be. Re is much stronger than Be and thus can support much higher pressure. In addition, Be weakens considerably at moderately elevated temperatures, making externally heated samples where the entire cell is heated virtually impossible. Re gaskets have no such problem. Some labs also ban the use of Be as a gasket material due

to its toxic nature, preventing some researchers from performing inelastic x-ray scattering experiments. The high-Z nature of Re would also prevent any parasitic signals from reaching the spectrometer in the event the stock Re gasket material had any transition-metal contamination.

The sample configuration used is shown in Fig. 3.7(a). The incident x-ray was sent along the axis of the DAC, through one of the diamond anvils. The outgoing IXS signal was then collected at an angle ϕ through the side of a *SAX* cell (see Sec. 3.1.1). This was accomplished by rotating the spectrometer to an angle $90°+\phi$, relative to the incident beam and the axis of the DAC, rather than rotating the cell.

Using Fig. 3.7(b) we can calculate ϕ to be

$$\phi = tan^{-1}\left[\frac{t_0 - t}{d_1 + \frac{t_0 - t - (d_1 - d_2)\ tan\ \alpha_2}{tan\ \alpha_1}}\right] \tag{3.1}$$

For beveled diamond anvils, typical values for α_1 and α_2 are 40° and 7°, respectively. For non-beveled diamonds, $d_1 = d_2$ and Eq. 3.1 reduces to

$$\phi = tan^{-1}\left[\frac{t_0 - t}{d_1 + \frac{t_0 - t}{tan\ \alpha_1}}\right] \tag{3.2}$$

where α_1, the girdle-pavilion angle, is typically 40°. One immediate consequence of Eqs. 3.1 and 3.2 is a thinner starting gasket thickness will yield significantly smaller values for ϕ. This is an important consideration since there is a maximum angle of 45° imposed by the *SAX* cell. Additionally, the background signal increases as one moves away from 90°. We therefore recommend using 10 mil stock Re foil, or $t_0 = 125\ \mu m$. It is also essential to remove the plastically deformed gasket materials (the "creep") from the side of the gasket where the signal is to be measured.

For 300-100 bevels ($d_1 = 300\ \mu m$, $d_2 = 100\ \mu m$, 10 mil Re stock) with a typical gasket thickness at loading of $t = 25\ \mu m$, the calculated angle is $\phi = 14.38°$. In practice, this angle was $\sim 18°$. Figure 3.7(b) only shows the idealized case where the indentation

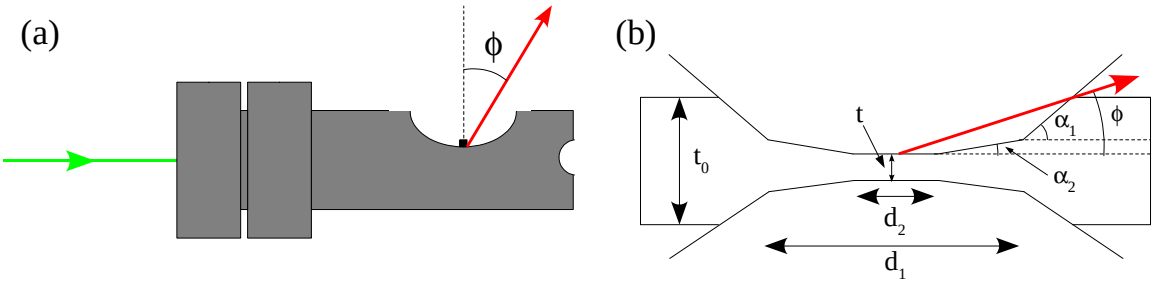

Figure 3.7. (a) Sample geometry for XES using a Re gasket. (b) Schematic drawing of generalized diamond and gasket for use with Eq. 3.1.

of the gasket occurs symmetrically and only considers signal coming from the center of the culet, on the surface away from the incident beam. In addition, the plastic deformation of the gasket around the diamond (the "creep"), is not taken into account. However, Eqs. 3.1 and 3.2 give a good initial estimate of this angle. It should be noted that this technique works best for x-ray emission spectroscopy where the incident x-ray energy is high enough to penetrate the diamond-anvils (See Sec. 3.2.3).

3.1.4 Pressure-transmitting Media and Cryogenic Loading Techniques

An ideal pressure-transmitting medium would have zero shear strength, *i.e.*, a liquid. Most liquids, however, solidify at pressures below 2 GPa making them unsuitable for use as a pressure transmitting medium. High pressure researchers discovered that a 4:1 mixture of methanol and ethanol remains a liquid up to 10 GPa [57] at room temperature. One potential drawback of this mixture is a glass transition above 10 GPa which allows the buildup of large shear stresses on the sample. However, it is readily available in a lab and easy to load into the sample chamber. Unfortunately, both methanol and ethanol are reactive and an alternative pressure media needed in order to study the lanthanides. Thus, mineral oil was used as a pressure-transmitting medium for all of the inelastic x-ray scattering experiments in this study. Mineral oil is easily loaded by using a small needle to

position a drop over the sample chamber. It is also chemically inert at ambient temperature.

Some samples, however, are very sensitive to non-hydrostatic stresses (CrO_2 for example). In these cases, a medium that stays quasi-hydrostatic at higher pressures is required. Mineral oil also fluoresces under Raman laser excitation. This fluorescence can sometimes overwhelm the weak Raman light and is therefore unsuitable for use during Raman spectroscopy experiments. The noble gases make very good hydrostatic pressure media because their solid phases are still very soft. They are also chemically inert and do not readily fluoresce under Raman laser excitation. However, they are gases at ambient conditions and must be loaded as a liquid, cryogenically, to obtain a sufficient density. Alternatively, pressurized gas can be loaded, however the pressures required to reach liquid density at ambient temperature are around 30,000 psi which is very difficult, and dangerous to achieve. Thus, cryogenic loading techniques were used when loading noble gases.

Argon is the most common noble gas used as a pressure-transmitting medium because it is much less expensive than Xe and liquifies above liq.-N_2 temperature, at ambient pressure. Thus, Argon was used as a pressure media in all Raman spectroscopy experiments described in this study. Helium stays liquid to the highest pressure of all the noble gases. It also forms the softest noble-gas solid. For these reasons, Helium makes the ideal pressure-transmitting medium and was used as the pressure medium during XRD experiments on CrO_2 since the rutile-$CaCl_2$ transition has been shown to be highly sensitive to non-hydrostaticity. Unfortunately, liq.-He is very difficult to work with due to its extremely low boiling point (4.2 K vs 87.3 K for Ar). It is therefore necessary to use a liq.-He cryostat to achieve the necessary low temperatures to liquify He. The cryogenic techniques used to load the noble gases as pressure media are described in the following section.

liq.-Ar

Argon gas was loaded using a gas "bomb" (a sealed chamber used to condense pure Ar) designed for the *LLL* cell. This device is shown in Fig. 3.8. This method was preferred over the "dunk" method which involves immersing the cell in a bath of liq.-Ar which can introduce contaminants such as ice into the sample chamber. The *LLL* cell was placed inside the loader with 2 of the 4 pressure screws of the cell coupled to the outside using feed-through allen wrenches. The loader was connected to a gas bottle through a regulator and flushed with Ar gas for at least 60 seconds by opening the vent valve. This step is crucial and ensures that as the loader is cooled, water ice does not formed inside, contaminating the sample. The vent valve was then closed and the loader immersed in either liq.-Ar or liq.-N_2. The temperature inside the loader was monitored using a K-type thermocouple mounted just above the cell. When liq.-Ar temperature was reached, the cell was opened, allowing liq.-Ar to enter the sample chamber, and then closed by turning the screws using the feed-through allen wrenches.

Using liq.-N_2 to cool the gas loader is less expensive, and faster than using liq.-Ar. However, because the boiling point of N is 6.3° lower than the freezing point of Ar at 1 atm, one must be careful not to let the liquified Argon freeze inside the chamber. Freezing of the liq.-Ar creates a layer of solid Ar between the diamond culets and the gasket, causing premature gasket failure. To prevent overcooling and the subsequent freezing of the liq.-Ar, the Ar gas pressure was increased to 30 psi during cooling. Figure 3.9 shows the PT phase diagram of N and Ar. The dashed line at ambient pressure (14.7 psi) illustrates the very small range of liquid temperatures at this pressure. Because the freezing point is relatively unaffected compared to the boiling point, 30 psi significantly increases the range of liquid temperatures as shown by the upper dashed line. By increasing the liquid temperature range, more time was allowed for opening and closing the cell, thus preventing freezing of

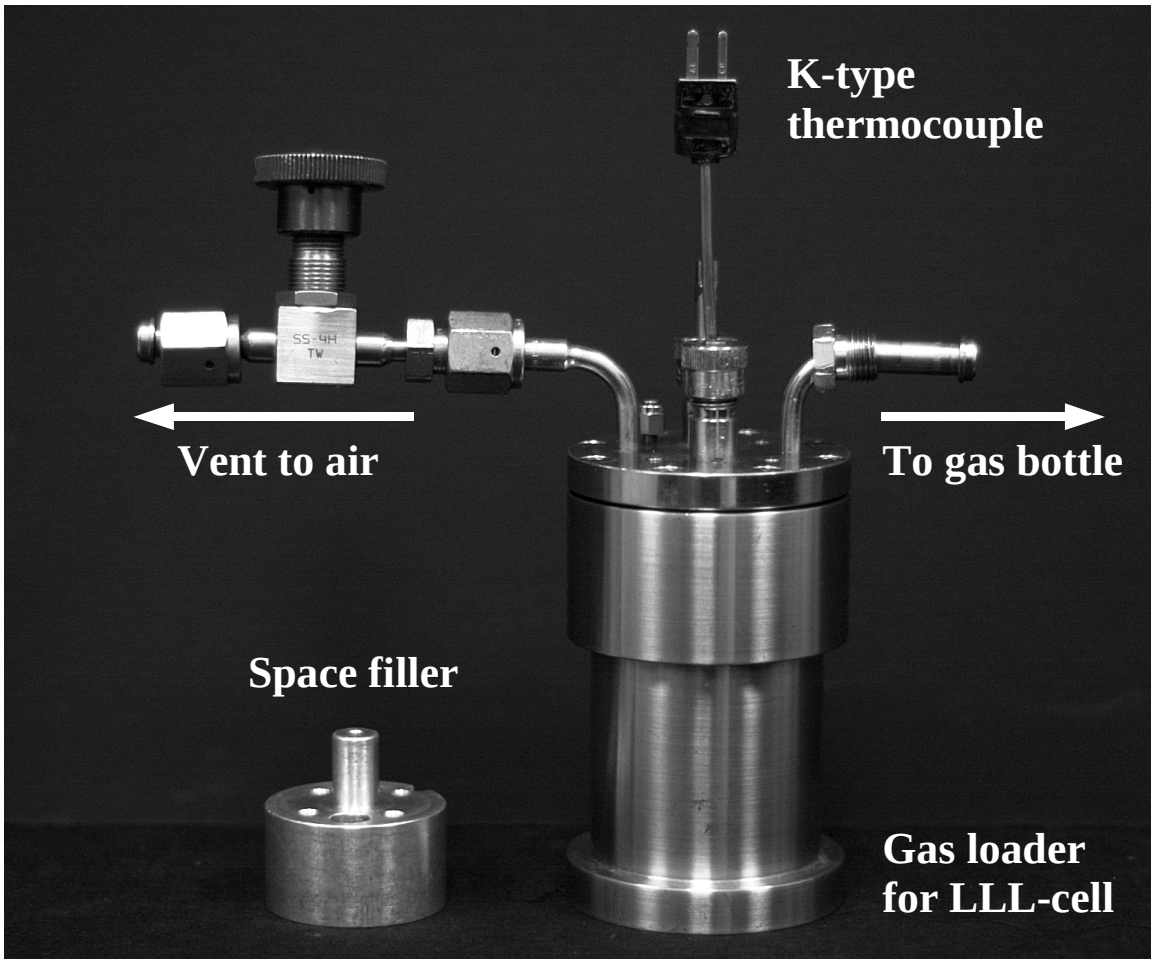

Figure 3.8. Picture of gas loader for use with *LLL* cell. The *LLL* was placed inside the loader, with the optional aluminum space filler to minimize the volume. The cell was coupled to the outside via two feed-through allen wrenches with teflon seals. The temperature was monitored using a K-type thermocouple. The loader was brought to cryogenic temperatures by immersing the entire unit in liquid cryogen (either liq.-N_2 or liq.-Ar).

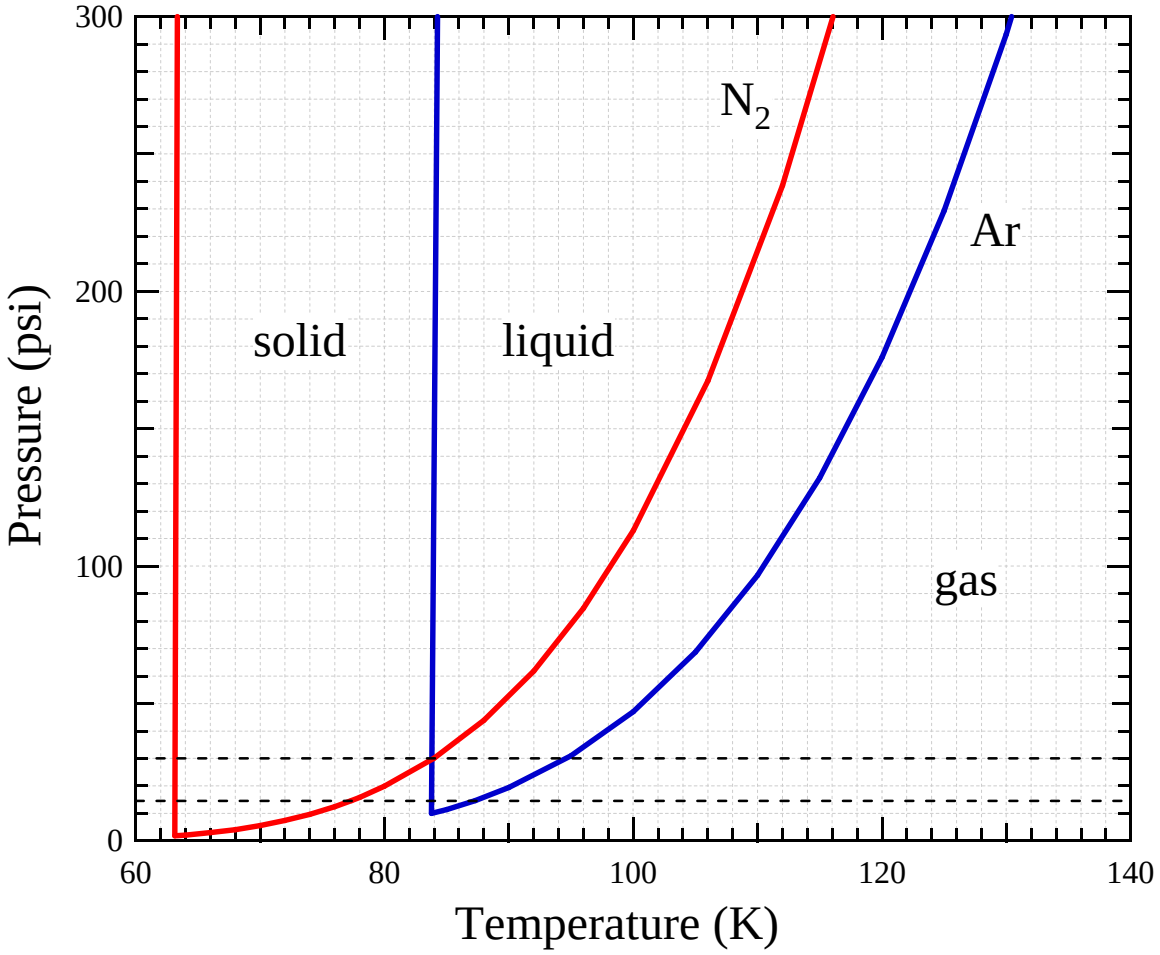

Figure 3.9. Phase diagram of N_2 and Ar. The lower dotted line denotes ambient pressure and the upper dotted line shows 30 psi. Increasing pressure dramatically increases the stability range of the liquid phase of Ar (N_2 to a smaller extent), an important consideration when loading using the cryogenic gas loading device shown in Fig. 3.8

the Ar medium.

liq.-He

Due to its extremely low boiling point (4.2 K), liq.-He is much more difficult to load and requires a continuous-flow liq.-He cryostat. Figure 3.10(a) shows a Janis Research cryostat modified for loading He into a *LLL* cell. The cryostat was used to cool the cell to liq.-He temperatures and to collect liq.-He, immersing the cell. A mount was made,

shown in Fig. 3.10(b), to hold the *LLL* cell and to support the long feed-through allen wrenches. The temperature of the cell body was monitored by a thermocouple diode. When the temperature reached the liq.-He range, a superconducting liq.-He gauge was used to measure the depth of liq.-He collected at the bottom of the cryostat. Once the level of liq-He reached the top of the cell, the cell was opened to allow liq.-He to flow into the sample chamber. The cell was then closed while monitoring light that was transmitted through the cell in order to ensure the feed-through allen screws were engaged.

The accumulated liq.-He is very turbulent and often times a sample is washed away when the cell is opened. Additionally, bubbles often times get trapped in the sample chamber instead of liq.-He. To combat these problem, superfluid ^{4}He was formed before opening the cell. This was accomplished by lowering the pressure using a roughing pump. Reducing the pressure also reduces the temperature inside the chamber by evaporative cooling. Once the temperature of the thermocouple diode read around 1.7 K superfluid would form. Because the turbulence disappears abruptly at the superfluid transition, the process of forming superfluid He could be visually monitored by observing the turbulence of the liq.-He through a Sapphire window on the bottom of the cryostat.

3.1.5 Pressure Determination

In general, the pressure inside a DAC is determined by measuring some pressure-calibrated property of a material (called a "pressure standard") placed in the sample chamber along with the sample. One common property is the unit cell volume of a crystalline material. The pressure can then be calculated from the known equation of state of the pressure standard. However, the unit cell volume can only by obtained through x-ray diffraction. This method is not useful for optical spectroscopy. It is also not useful for experiments where there is no access to an x-ray diffractometer. Also, during x-ray diffraction

Figure 3.10. Picture of He loading dewar designed for use with *LLL* Cell.(a) shows Janus Research cryostat. Connected to the inside via feed-throughs a diode temperature sensor and superconducting l-He level sensor.(b) shows holder for cell which is place inside the cryostat. The *LLL* cell is attached at bottom (cell not shown). The cell is open/closed via long feed-through allen wrenches.

experiments the additional diffraction lines from the pressure standard often times overlap with lines from the sample.

Fluorescence spectroscopy offers a more convenient way of measuring pressure without the need for an x-ray diffractometer. Piermarini *et al.* [58] published the first calibration of the R1 fluorescence line of Ruby (up to about 19.5 GPa) in 1975 using the known EOS of NaCl. Ruby fluorescence was a revolution in DAC physics, allowing pressure measurement with only a small Ruby chip (1-2 μm) placed in the sample chamber. The pressure-induced shift of the R1 fluorescence line, $\Delta\lambda_{R1}$, was later calibrated to almost 1 MBar by Mao *et al.* [59]. They found that, under quasi-hydrostatic conditions, the pressure can be calculated as

$$P = A/B[1 + (\frac{\Delta\lambda_{R1}}{\lambda_{R10}})]^B - 1 \tag{3.3}$$

where $A = 1904$ GPa and $B = 7.665$ [59]. The accepted value for the zero-pressure wavelength of the R1 lines is $\lambda_0 = 694.271$ although, this value can change slightly due to different concentrations of Cr^{3+}. It is good practice to experimentally measure λ_0 from the same stock of Ruby which was used in your experiment.

The ruby fluorescence method also allows one to qualitatively determine the degree of hydrostaticity in the sample chamber by observing the line widths of the R1 and R2 lines. Fig. 3.11 shows the Ruby fluorescence spectrum at 4 and 20.6 GPa. At ambient conditions the R1 and R2 peaks are well resolved. However, when large pressure gradients are present in the sample the ruby fluorescence lines broaden, as illustrated in Fig. 3.11. This is a qualitative measurement, however, and a more informative method of determining the condition in the sample chamber would involve placing multiple pieces of Ruby at the center of the sample and near the edges to determine the pressure gradient across the sample.

The fluorescence of Ruby is quite strong under 514 nm excitation and below 50 GPa. Above 50 GPa, however, the excitation mechanism shifts to higher energy. At this

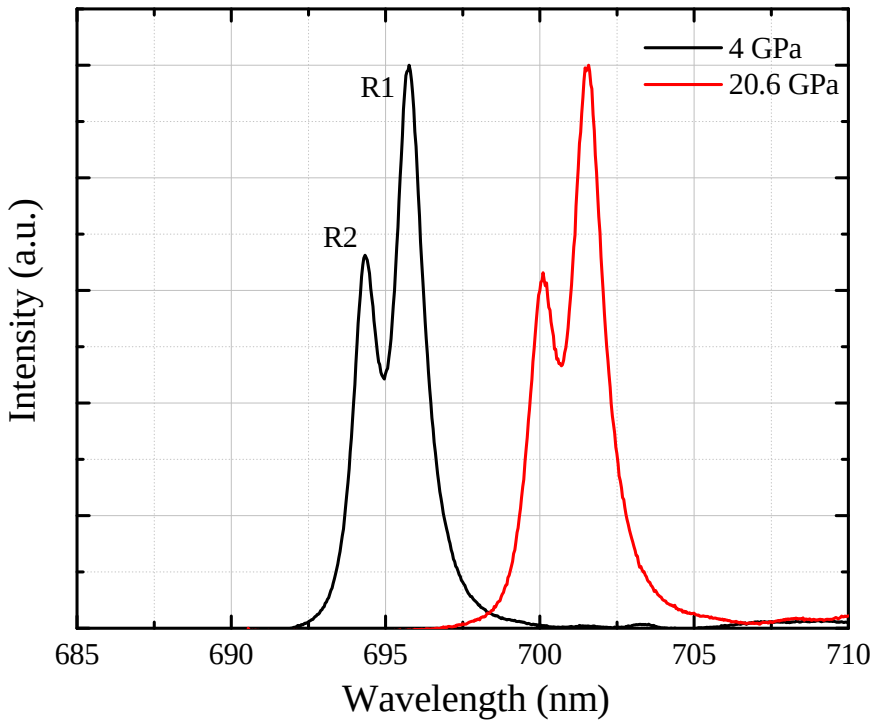

Figure 3.11. Sample Ruby fluorescence spectra at 4 GPa and 20.6 GPa showing the pressure-induced shift of the R1 and R2 fluorescence lines.

pressure, the fluorescence intensity under 514 nm excitation begins to rapidly decrease, making pressure determination difficult if not impossible. For pressures above 50 GPa excitation the 457.9 nm Argon Ion laser line, or shorter, should be used [60]. At very high pressures ($P \gg 1$ MBar), the most efficient pumping mechanism shifts back to longer wavelengths due the attenuation of shorter excitation wavelengths by the diamond anvils.

3.2 3^{rd}-Generation Synchrotron X-ray Techniques

Pressures exceeding 1 Mbar are only achieved by using very small diamond culets ($\leq$ 100 μm. See Sec. 3.1). Consequently, samples are typically $\sim$ 50 μm, or smaller, in diameter. Successful x-ray studies of such minute samples require a highly collimated, brilliant x-ray source. The 3^{rd}-generation synchrotrons such as the Advanced Photon Source (APS) at Argonne National Lab, built in 1996, are ideal for high-pressure materials research on minute samples. Their brightness (flux/area at the sample) can be three orders-of-magnitude (or more) higher than the brightest 2^{nd}-generation source. And, because they are high brilliance (highly collimated, high flux), 3^{rd}-generation synchrotron beams can be focused to submicron sizes.

These advances in synchrotron technology, combined with state-of-the-art DAC technology (see Sec. 3.1) provide new, or improved, capabilities critical to studying electronic phase transition at high pressure. The following sections describe the three synchrotron x-ray techniques used in this study and the beamline at which they were performed. These techniques are: (i) *in-situ* angle-dispersive x-ray diffraction (ADXRD) to explore the phase diagrams of materials, (ii) non-resonant x-ray emission spectroscopy (XES) to study the magnetic moments of transition metal monoxides, and (iii) resonant inelastic x-ray scattering (RIXS, also known as resonant x-ray emission spectroscopy) to probe the electronic

structure of correlated f-electron metals.

3.2.1 The HP-CAT Beamline

Sector 16 of the APS at Argonne National Lab is home to the HP-CAT (High Pressure Collaborative Access Team) beamline and represents a collaboration between the Carnegie Institution, DOE, LLNL, the University of Hawaii, and the University of Las Vegas. Completed in 2003, HP-CAT provides a unique synchrotron x-ray facility dedicated to high pressure studies and is comprised of two sets of experiments hutches fed by an undulator insertion device and a bending magnet, respectively. The bending magnet provides a broad-spectrum x-ray beam suitable for energy-dispersive diffraction experiments at high pressure. The undulator device generates a narrow-band, high brilliance x-ray beam ranging from 6 keV to 13 keV (first harmonic) which services both the ADXRD hutch (16 ID-B) and inelastic x-ray scattering (IXS) hutches (16 ID-D, 16 ID-E). All sychrotron x-ray experiments described in this work were performed at either 16 ID-B or 16 ID-D

Front-end Optics

The undulator x-ray beam is monochromated by a diamond double-crystal monochromator. The beam is first Bragg diffracted by the first diamond crystal and then intercepted by the second crystal. The resulting diffracted beam is both parallel to, and offset from the original undulator beam. In this way, part of the original beam is diverted to beamlines 16 ID-D and 16 ID-E for IXS experiments while the remainder of the original beam passes through the first diamond crystal unchanged and is used for diffraction experiments at beamline 16 ID-B. By changing the angles of the diamond crystal pair in relation to the undulator x-ray beam it is possible to tune the energy of the resulting monochromated beam while leaving the remaining portion of the beam unchanged.

16 ID-B

Angle-dispersive x-ray diffraction requires monochromatic x-rays. The bandwidth of an undulator beams is $\sim 1/N$ where N is the number of periods. The undulators used at the APS typically have $N \simeq 72$ periods. $\lambda = .4133$ Å (30 keV) this gives an uncertainty of $\delta\lambda = .0057$ Å. This uncertainty is too large for high-resolution ADXRD. Hence, the undiverted beam is further monochromated using a Si (220) single crystal monochromator. The beam is then microfocused by a pair of 0.3 m Kirpatrick-Baez bimorph mirrors, with a focal length of 750 mm, before entering the 16 ID-B hutch. The focus size varies from run to run due to changes in temperature and undulator beam quality. The typical x-ray focal spot is rectangular, with dimensions $\sim 15 \times 10$ μm.

The diffracted x-rays are collected using a Mar345 image plate detector which uses an x-ray sensitive plate to record the x-ray pattern. This works by trapping photoelectrons in lattice defects which were introduced into the image plate during the manufacturing process [61]. When an incoming x-ray photon strikes the plate, a photoelectron is generated by ionizing a Eu^{2+} ion to form Eu^{3+}. In this way, the image plate stores a record of the x-ray pattern using these defects in the form of trapped electrons. After an exposure ranging from 5s to over 60s, the pattern is read by using a laser to excite the trapped electron into the conduction band. The electron then recombines with the Eu ion to form Eu^{2+} giving off a photon at around ~ 400 nm. These photons are then collected by a photo-multiplier tube.

3.2.2 Angle-Dispersive X-ray Diffraction

The 1914 Nobel Prize in Physics was awarded to Max von Laue for *"his discovery of the diffraction of X-rays by crystals"*. A year later, Sir William Henry and William Lawrence Bragg won the Nobel Prize for their contribution to the understanding of crystals

structures using x-rays. This important technique has since become the primary technique for determining the structural properties of materials. It works by taking advantage of the coherence properties of certain x-ray beams. The predominant process when an x-ray strikes an atom is Rayleigh scattering whereby an atom absorbs the photon and re-emits another photon at the same energy. When an x-ray photon strikes an atom the outgoing spherical wave interacts with similar outgoing waves from neighboring atoms, generated by other, coherent photons. The superposition of these waves produces constructive and destructive interference depending on where in the lattice they originate. This collective process is known as x-ray diffraction.

For a crystalline material, the condition for diffraction is given by the Bragg equation

$$n\lambda = 2d_{(hkl)}\ sin\ \theta_B \tag{3.4}$$

where λ is the wavelength of the x-ray beam, $d_{(hkl)}$ is the spacing between the (hkl) set of lattice planes, and θ_B is the angle between the lattice planes and the incident x-ray beam. ADXRD uses a single, monochromatic x-ray beam to project an x-ray diffraction pattern onto a plate detector. This is in contrast to energy dispersive x-ray diffraction, originally used by Man von Laue, which uses a broadband x-ray beam and an energy-resolving detector. However, ADXRD is better suited for high pressure experiments due to the strong preferred orientation present in many high pressure samples (see Below). Additionally, the energies typically used ($\sim 30keV$) easily penetrate the diamond anvils (see Fig. 3.4). For a derivation of the Bragg condition and an explanation of the (hkl) nomenclature see Appendix A.

Powder Diffraction

Most single crystals do not survive to high pressure. One reason is the sample chamber thickness decreases with increasing pressure. At high enough pressure all single crystals will be crushed by the diamond anvils. Additionally, all crystals break into many pieces during a structural phase transition due to changes in volume and atomic arrangement. Some materials cannot easily be grown into single crystals. Because of these difficulties all ADXRD experiments discussed here were performed on powdered samples.

We define "powdered" as a sufficiently finely-grained sample whose distribution of crystal orientations is continuous [62]. The resulting x-ray diffraction pattern is made up of rings of diffracted rays, called the Debye-Scherrer rings, instead of individual spots as in single-crystal diffraction. Figure 3.12 shows a sample powder diffraction pattern from CrO_2 at 6.87 GPa. The top image shows a portion of the raw diffraction image illustrating the Debye-Scherrer diffraction rings. The large, dark spots are single-crystal diffraction from ruby inside the sample chamber.

Samples often develop preferred orientation, or a partial alignment of small powder particles along a certain crystallographic orientation, at high pressure. This manifests as non-uniformities in the Debye-Scherrer rings. In ambient pressure experiments the entire diffraction rings are collected and the preferred orientation can be modeled during data analysis to correct for the altered intensities produced by preferred orientation. However, only partial Debye-Scherrer rings were collected for the materials in this study due to the slotted design of our DACs. This introduced large errors in the internal coordinates of CrO_2.

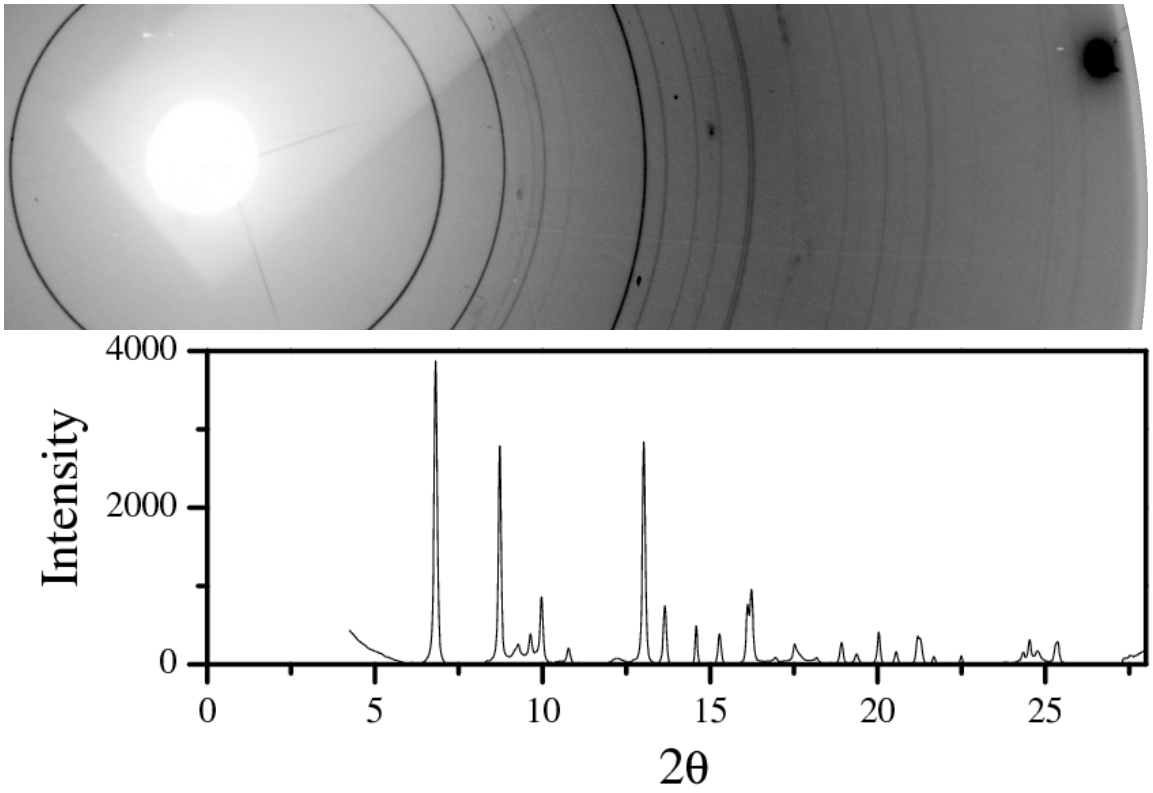

Figure 3.12. Sample powder diffraction image of CrO_2 at 6.87 GPa and $T = 300$K. Top image shows raw diffraction pattern illustrating the Debye-Scherrer rings produced during powder diffraction. Bottom image shows the integrated 1D diffraction pattern derived from the top image. The two images have been aligned along the x-axis. Large dark spots are single-crystal diffraction spots from Ruby (they were masked during integration and do not appear in the 1D diffraction pattern). Note that only partial Debye-Scherrer rings are collected due to the slotted design of the DAC.

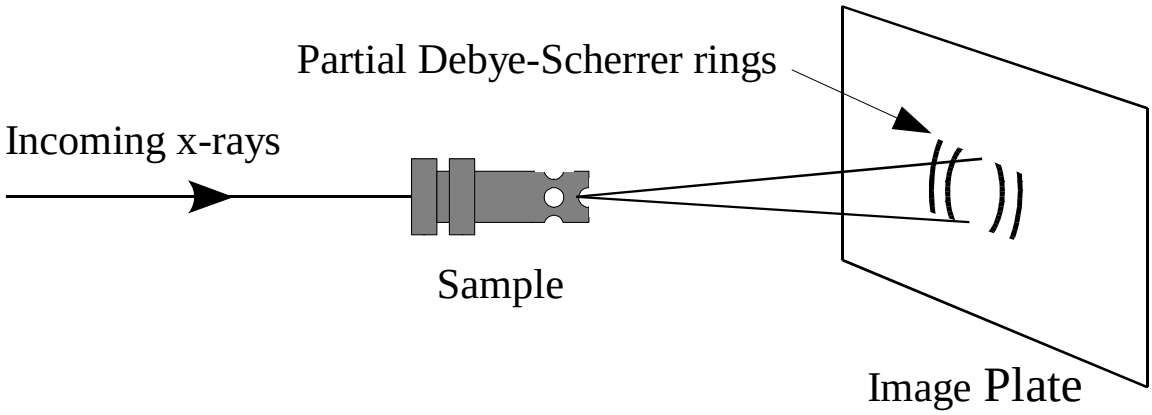

Figure 3.13. Sample geometry for angle-dispersive x-ray diffraction (ADXRD) at high pressure. A monochromatic x-ray beam is incident along the axis of the DAC (*LLL* cell shown) through one of the diamond anvils. The Debye-Scherrer rings are then collected through the opposing diamond anvil out a slotted port in the DAC. Not that this slotted design only allows partial rings to be collected.

Experimental Geometry

The sample geometry used in these experiments is shown in Fig. 3.13. The monochromatic x-ray beam was incident along the axis of a *LLL* cell, through the piston-side diamond anvil. The diffracted x-rays were then collected from the opposite diamond anvil through the opening on the anvil end of the DAC. The Livermore-designed *LLL* cell we used for x-ray diffraction (see Sec. 3.1.1) has a slotted opening which matches the slotted opening on the tungsten carbide seat. This limits the maximum usable $2\theta_B$ to $\sim 25^\circ$ in the horizontal direction, and even less in the vertical direction. The result is a rectangular diffraction pattern containing only partial Debye-Scherrer rings (see Sec. 3.1.1).

Data Analysis

Powder diffraction patterns were analyzed by first integrating the 2D diffraction image to produce a 1D diffraction pattern. This was performed using the fit2D program [63]. Using the size of the image plate and the distance from the diffraction source to the

image plate as input, fit2D computes values of $2\theta_B$ and integrates the diffraction pattern in concentric rings, producing a 1D spectrum. The bottom plot in Fig. 3.12 shows a 1D diffraction pattern derived from the top image using this program. The two images have been aligned such that the diffraction peaks in the bottom image line up with their corresponding diffraction ring.

Because the diffraction image from a powder sample is an average of all crystal orientations, some information is lost compared to single crystal diffraction. For example, in the simple cubic lattice the (100), (010), and (001) lattice planes all have the same lattice spacing, $d_{[100]}$. An x-ray beam incident along the (111) direction would yield a 3-fold symmetric pattern of spots corresponding to the 3 distinct sets of lattice planes. However, during powder diffraction, all three sets of planes would overlap to produce one diffraction ring. Hence, the analysis of powder diffraction data can be much more difficult than for single-crystal diffraction and often times, a unique solution can be difficult to find. Thus, the GSAS program was used to aid in the analysis of our powder diffraction data. This program employs the Rietveld method which fits an integrated powder diffraction spectrum with a calculated spectrum using values such as the internal atomic coordinates as well as the overall lattice constants as variables [64].

3.2.3 X-ray Emission Spectroscopy

Magnetic moments in d- and f- electron metals are the result of electron correlations. Changes in the strength or nature of the correlation are often reflected in these moments. It is therefore important to study these moments at high pressure if we are to understand the nature of many electronic phase transitions. Since the magnetic moments are formed out of electrons, spectroscopies which can probe the occupied valence states of materials are often used. X-ray photoemission spectroscopy (XPS) uses x-rays to eject

valences electrons whose properties such as energy, momentum and spin are then measured. This technique, however, cannot be applied to high pressure samples in a DAC. This is because the photoelectrons cannot penetrate neither the diamond anvils nor any known gasket materials.

Non-resonant x-ray emission spectroscopy (NXES, or just XES) is an IXS technique that also uses x-rays to probe the valence states of materials. However, instead of measuring the properties of photoelectrons as in XPS, XES measures secondary photons emitted from the decay of this excited state. In XES, high energy x-rays are used to excite core-level electrons into continuum states, well above the absorption threshold. This core hole quickly decays and, in the process, emits a photon. These photons are then collected and analyzed. Because it is a photon in/photon out experiment, XES is ideally suited to high pressure experiments. Additionally, the incident and emitted photon energies are high enough to penetrate diamond anvils and x-ray transparent Be gaskets (see Sec. 3.1.2).

XES in the Transition Metals

In 1968, Tsutsumi *et al.* showed that a mysterious satellite peak in the $K\beta$ XES spectrum of transition metal compounds resulted from the exchange interaction between the $3d$ magnetic moment and the $S = 1/2$ moment left over from the core hole decay. The $K\beta$ emission process is illustrated in Fig. 3.14 for the Mn^{2+} ion. The initial state is shown on the left-hand side. An incident x-ray photon, with energy Ω, excites a $1s$ electron into continuum states. The intermediate state (not shown) then contains a core-hole in the $1s$ orbital. This excited state decays through a number of dipole allowed transitions. However, $K\beta$ emission is the decay through a $3p \rightarrow 1s$ transition and occurs at 6490.45 keV. The final state of $K\beta$ XES, shown on the right hand side of Fig. 3.14, contains a $S = 1/2$ hole in the $3p$ orbitals. For XES, which is non-resonant, Ω should be much greater than the

absorption threshold. For the Mn^{2+} ion $\Omega \gg 6539$ eV.

High-spin Mn^{2+} contains five spin-aligned $3d$ electrons forming a $S = 5/2$ moment. The exchange interaction between the $3d$ electrons and the $3p$ hole produces two final state configurations with total spin $S_{Total} = 2$ and $S_{Total} = 3$ [65]. The total orbital moment is just $L_{Total} = 1$ and comes from the $3p$ hole since $L = 0$ for a half-filled $3d$ orbital. We can then write down the two final state configurations, in spectroscopic notation, as ^7P and ^5P corresponding to a parallel and anti-parallel alignment of the $S = 5/2$ moment from $3d$ electrons and the $S = 1/2$ moment from the $3p$ hole, respectively. These two final states are separated by 16 eV [6]. The spin-orbit coupling further splits these states into $^7P_{4,3,2}$ and $^5P_{3,2,1}$ levels, separated by ~ 1 eV.

The ambient conditions $K\beta$ emission spectrum of the Mn^{2+} ion is therefore comprised of the main $K\beta$ line and the $K\beta'$ satellite peak, corresponding to the $^7P_{4,3,2}$ and $^5P_{3,2,1}$ final states described above. An atomic multiplet calculation of the XES spectrum of Mn^{2+} , reprinted from Peng *et al.* [6]) confirms this argument. Tsutsumi also showed that the exchange splitting ΔE and intensity ratio I'/I (branching ratio) between the $K\beta$ and $K\beta'$ peaks can be written as

$$\Delta E = J(2S - 1) \tag{3.5}$$

and

$$\frac{I'}{I} = \frac{S}{S+1} \tag{3.6}$$

where S is the magnitude of the $3d$ spin moment. Equations 3.5 and 3.6 show that a reduction in S, such as that resulting from a Mott transition, will manifest in the $K\beta$ XES spectrum as a reduction of the branching ratio as well as a reduction in the exchange splitting.

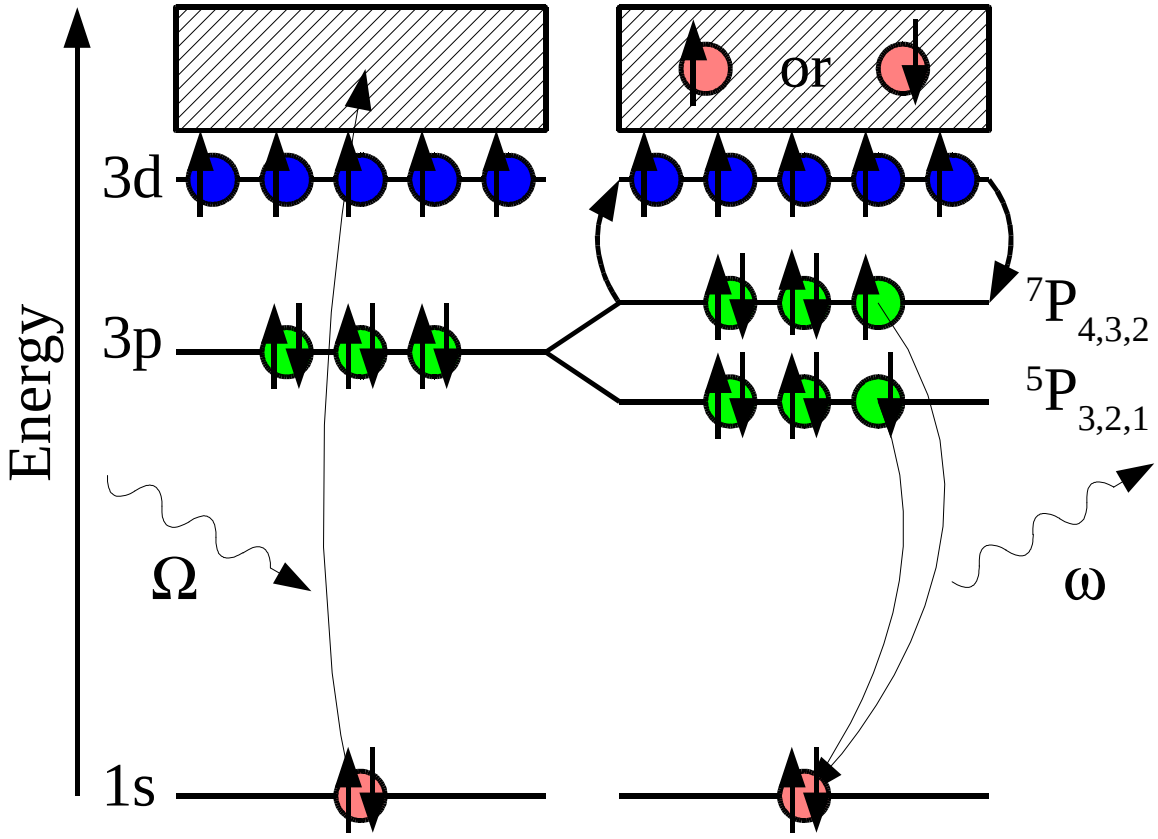

Figure 3.14. X-ray emission process for $K\beta$ emission in the transition metal oxides (MnO). An incident x-ray photon of energy Ω excites a $1s$ core electron into the continuum states, well above the absorption edge. The $1s$ core hole decays through $K\beta$ $3p \rightarrow 1s$ emission leaving a $3p$ hole in the final state. The exchange interaction between the $S = 5/2$ moment of the spin aligned 3d orbitals with the $S = 1/2$ moment left on the $3p$ orbital produces a splitting in the final state with configurations $^7P_{4,3,2}$ and $^5P_{3,2,1}$ depending on whether the $S = 5/2$ and $S = 1/2$ moments are aligned or anti-aligned.

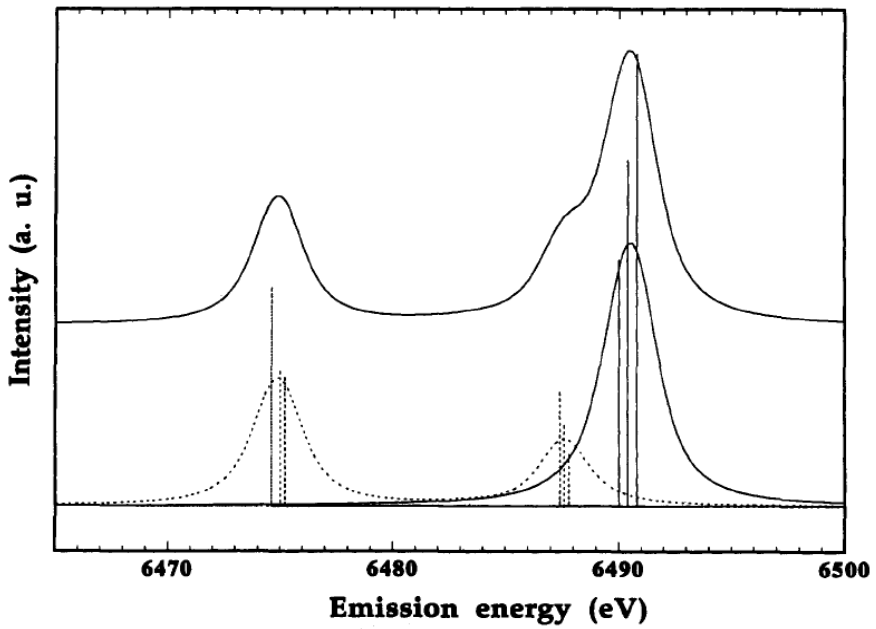

Figure 3.15. Calculated XES spectrum reprinted from Fig. 1 of Peng *et al.* [6] for the Mn^{2+} ion. Bottom curve shows spectra calculated for $^7P_{4,3,2}$ (solid curve) and $^5P_{3,2,1}$ (dotted curve) final states. Top curve shows the combined spectra. Vertical lines show the energy positions of the individual term states.

XES in Rare Earths

Similar arguments can also be applied to $4d \rightarrow 2p$ $L\gamma_1$ XES in the $4f$ metals. At ambient conditions, their $4f$ electrons are highly correlated. These electrons form the spin moments responsible for ferromagnetism in the rare-earths. Figure. 3.16 is reprinted from Jouda *et al.* [7] and shows $L\gamma_1$ XES spectra for a number of rare-earth compounds. The exchange interaction between the $4f$ spin and the $4d$ $S = 1/2$ moment gives rise to a splitting in the $L\gamma_1$ emission spectra.

According to Eq. 3.6 the branching ratio should be maximal at half-filling. However, the DyF_3 $L\gamma_1$ XES spectrum (bottom curve in Fig. 3.16) exhibits a branching ratio larger than that of GdF_3 despite being f^9 ($S = 5/2$) compared to half-filled f^7 Gd ($S = 7/2$). This discrepancy is due to different dominant decay processes in the heavy vs. the light rear-earths [66]. Calculations by Tanaka *et al.* confirm this explanation (solid line in DyF_3 XES plot shown in Fig. 3.16) [8]. However, a collapse of the $4f$ magnetic moment (pairing of spins), as is expected during a Mott transition, would still be detected as a strong reduction in the branching ratio.

3.2.4 Resonant-Inelastic X-ray Scattering

Until recently, x-ray absorption spectroscopy (XAS) has been the dominant technique used to probe the unoccupied states of a material. These states can provide information such as the ground state valency of atoms, as well as their crystal environment (EXAFS), inside a material. In XAS, the incident x-ray beam is tuned through an absorption edge of a material. A detector is then placed behind the sample to measure the transmitted x-ray intensity. $M_{IV,V}$-edge XAS ($3d \rightarrow 4f$) is used to probe the ground state valency of rare-earths and rare-earth compounds [67]. Ground state valency is important in correlated systems and can be used to measure not only the degree but also changes in

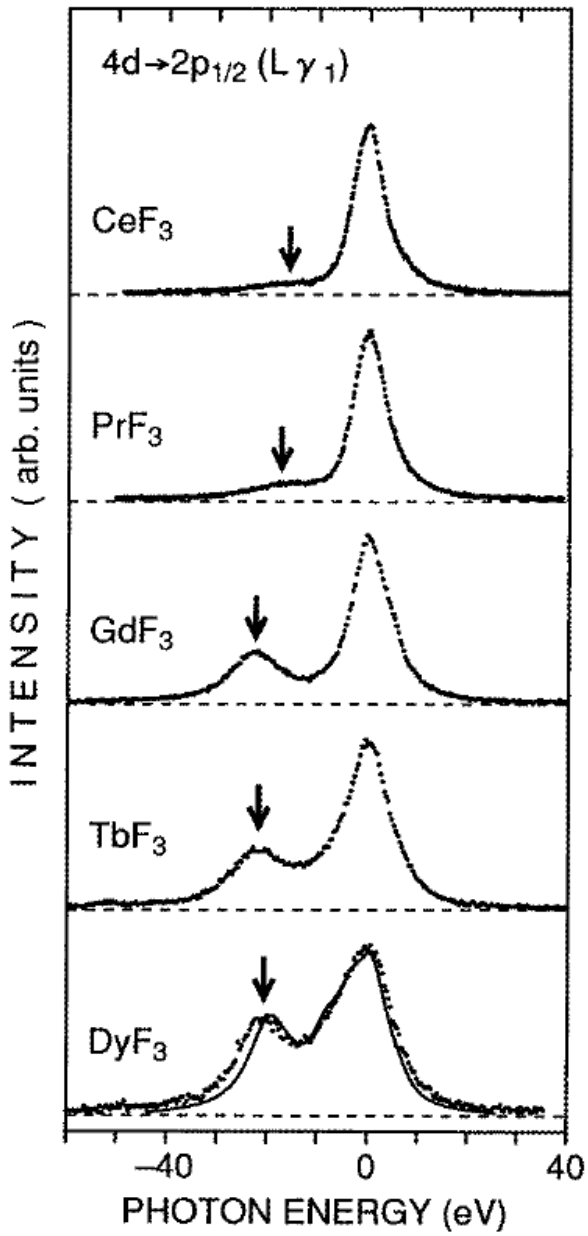

Figure 3.16. $L\gamma_1$ ($4d \rightarrow 2p$) XES spectra for a series of lanthanide compounds reprinted from Jouda *et al* (Fig. 1) [7]. The satellite structure is a result of the exchange interaction between the $4f$ moment and the $S = 1/2$ spin moment on the $4d$ orbitals in the final state of the XES process. The solid line in the bottom (DyF_3) plot is a calculated spectrum from Tanaka *et al.* [8].

electron correlation. However, the $M_{IV,V}$ edges of the lanthanides range from 853 eV in Ce to 1333 eV in Dy. These energies penetrate neither diamond anvils nor any know x-ray transparent gasket materials (see Sec. 3.1.2). Thus, $M_{IV,V}$-edge XAS is unsuitable for use in high pressure experiments. L_{III} edge XAS ($2p \rightarrow 5d$) is high enough energy (7243 eV in Gd) to penetrate both the diamond anvils and beryllium gaskets and contains a low energy $2p \rightarrow 4f$ feature which may be used to study ground state valence properties. However, $2p$ core-hole lifetime broadening obscures any information on the $4f$ states contained within the XAS spectrum, a situation made worse at high pressure.

Resonant-inelastic x-ray scattering (RIXS), also known as resonant x-ray emission spectroscopy (RXES), overcomes the $2p$ core-hole broadening present in L_{III} XAS by measuring the photons emitted during the $2p$ core-hole decay process. Figure 3.17 shows the the $2p3d$ RIXS process for Gd metal with ground state electron configuration $4f^n(5d6s)^v$, where n is the f occupancy and v is the valence ($n = 7$ and $v = 3$ for Gd). Incident x-rays, with energy Ω, tuned to the L_{III} edge at 7243 eV, strike the sample. These x-ray photons excite $2p$ core electrons into unoccupied conduction states leaving a $\underline{2p}$ core hole. The incident energy is stepped through the L_{III} edge, exciting core electron first into the lower-lying $4f$ states and then into high energy hybridized ($5d6s$) states with intermediate state electron configurations of $\underline{2p}4f^{n+1}(5d6s)^v$ and $\underline{2p}4f^n(5d6s)^{v+1}$, respectively.

At each value of Ω, the inelastic $\underline{2p}$ core hole decay through $3d \rightarrow 2p$ $L\alpha_1$ emission is collected and analyzed as a function energy. The final state of the RIXS process is shown on the right hand side of Fig. 3.17. A $3d$ electron has filled the $2p$ core hole, emitting $L\alpha_1$ x-rays of energy ω, creating the two final state configurations $\underline{3d}4f^{n+1}(5d6s)^v$ and $\underline{3d}4f^n(5d6s)^{v+1}$.

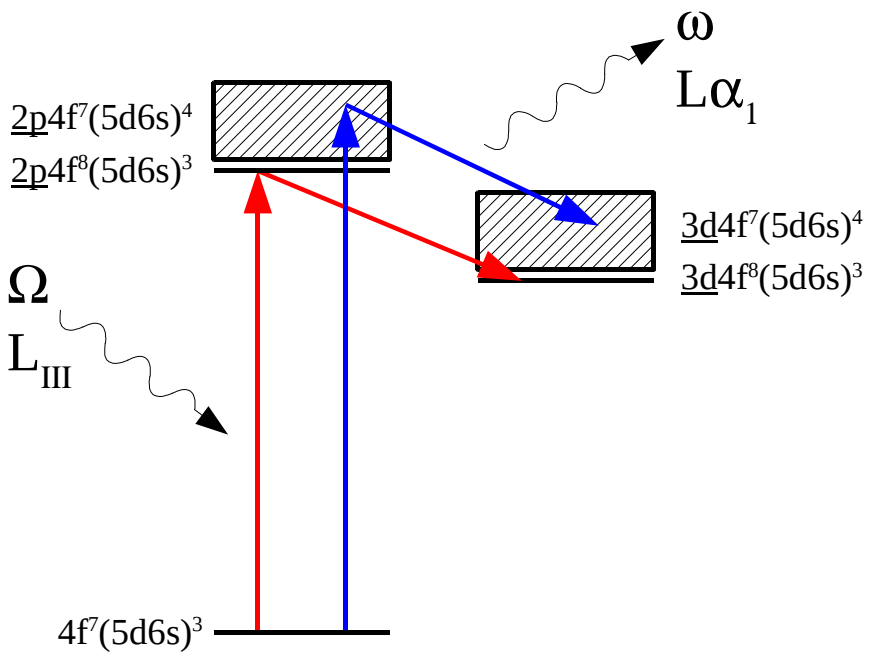

Figure 3.17. Schematic diagram illustrating the RIXS process in the lanthanides, specifically Gd metal. An incident x-ray with energy Ω, tuned to the L_{III} absorption edge, resonantly excites a $2p$ core electron into unoccupied valence states. By monitoring the core-hole decay through $3d \rightarrow 2p$ emission we are able to obtain information normally hidden in L_{III} x-ray absorption due to lifetime broadening caused by the short lifetime of the $2p$ core hole.

Data Analysis

In our experiments, Ω was typically scanned through a range of 30 eV in steps of 2 eV. The resulting dataset was a 2-dimensional array of intensities as a function of incident and emission energy. It is common to convert the emission energy axis to energy transfer, $(\Omega - \omega)$, corresponding to the $3d \rightarrow 4f$ and $3d \rightarrow (5d6s)$ absorption energies normally inaccessible at high pressure using standard XAS techniques. A 2D RIXS dataset of Gd at 5.5 GPa is shown in Fig. 3.18. Because the low energy unoccupied valence levels have a fixed energy, the peaks in the resulting spectrum stay at fixed $\Omega - \omega$. This is similar to the way Raman peaks occur at the same value of the Raman shift regardless of the excitation laser wavelength (see Sec. 3.3.1). The two resonances, $2p \rightarrow 4f$ and $2p \rightarrow (5d6s)$ are shown by the vertical white lines. When the incident energy is tuned above the $2p$ absorption threshold, the emission peaks no longer stay at fixed energy transfer but instead stay at fixed emission energy. This non-resonant x-ray emission (NXES) is identified by the diagonal line in Fig. 3.18.

Various 1D reductions of the full 2D RIXS dataset are possible. A constant energy (CE) scan is obtained by taking a vertical slice through the 2D plot shown in Fig. 3.18. These 1D CE scans show the precise resonant energy for each RIXS peak. A partial fluorescence spectrum can be derived by extracting intensity values at a fixed emission energy ω as a function of incident energy Ω. In Fig. 3.18, this would correspond to vertical slice provided the horizontal axis was converted back from $\Omega - \omega$ to just ω. If this slice is taken at the peak emission value for $L\alpha_1$ emission, the resulting 1D spectrum is roughly equivalent to a line-narrowed L_{III} XAS spectrum. Alternatively, one can analyze each 1D emission spectrum separately. This was done for Gd. The results are are presented in Sec. 4.2.1.

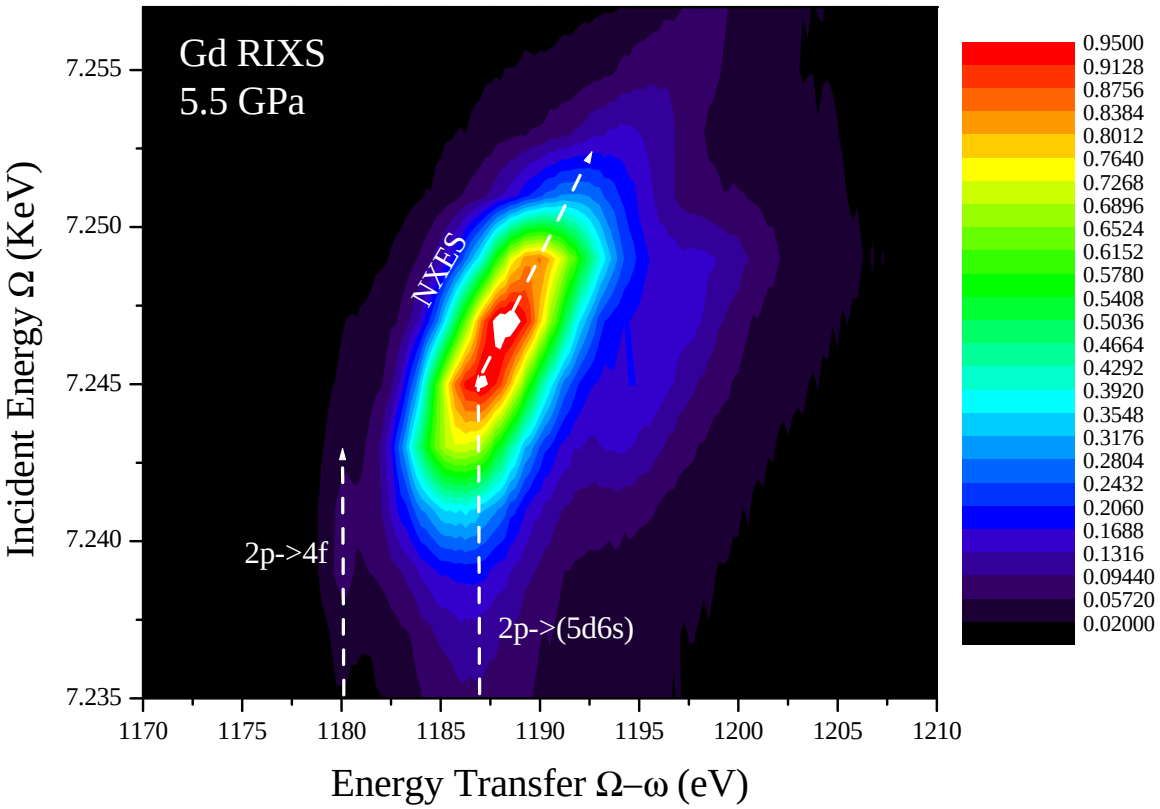

Figure 3.18. Contour plot of a 2D RIXS dataset of Gd at 5.5 GPa as a function of incident energy, Ω, and energy transfer, $\Omega - \omega$. The vertical dotted lines show the positions of the $2p \rightarrow 4f$ and $2p \rightarrow (5d6s)$ resonances. The NRIXS is shown as the diagonal line representing normal x-ray emission produced by excitation above the absorption edge.

3.2.5 IXS at High Pressure

This section gives an overview of the IXS setup at sector 16 ID-D (HP-CAT) of the Advance Photon Source at Argonne National Lab. Both XES and RIXS use the same basic experimental setup consisting of an incident synchrotron x-ray beam, sample mount, x-ray spectrometer, and detector. The main difference in setup between the two techniques is the way the sample was mounted.

Experimental Geometry

Samples were mounted either parallel, with axis of the DAC parallel with the incident x-ray beam, or perpendicular, with the axis of the DAC perpendicular to the x-ray beam, depending on the experiment. These two configurations are shown in Fig. 3.19. During XES experiments, Ω was tuned well above the absorption threshold of the material, between 10-14 keV. Because diamond is fairly transparent at these energies, the incident x-ray beam was sent through one of the diamond anvils (see Sec. 3.1.2), as shown in Fig. 3.19(a). The outgoing XES signal was then collected at 90° from the incident beam, through a Be gasket. One exception was Eu XES, where a rhenium gasket was used. In this case, the signal was collected from between the diamond and the gasket, at an angle slightly larger than 90° relative the incident beam and the axis of the cell, to avoid the gasket ($\sim$ 108 ° see Sec. 3.1.3).

For 2p3d RIXS on the lanthanides the incident x-ray energy was tuned to the L_{III} absorption edge. This energy ranges from 5732 eV in Ce to 7790 eV in Dy. At these energies, the attenuation length of diamond ranges from 350 μm to 900 μm. At a typical diamond thickness of $\sim$ 2 mm, the incident flux would be reduced by at least a factor of four (see Sec. 3.1.2). Hence, the incident x-ray beam was sent through a Be gasket. The RIXS signal emitted from the sample was then collected at 90° relative to the incident

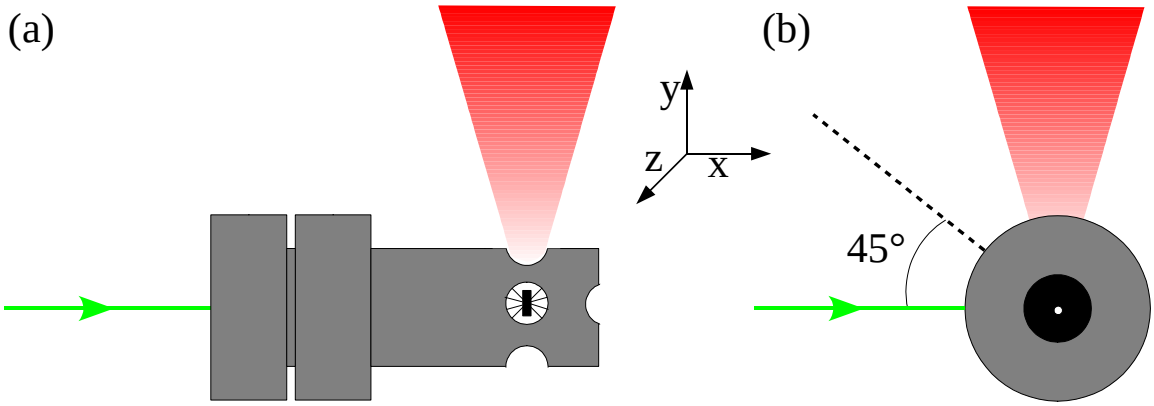

Figure 3.19. The two sample mounting configurations used for IXS. (a) shows the geometry used for XES with the incident beam coming through one of the diamond anvils and the XES signal collected at 90° through a Be gasket. (b) shows the geometry used for RIXS with the incident beam coming through the Be gasket and the RIXS signal collected at 90° through the gasket. In addition, during certain RIXS experiments the cell was tilted along the 45° (see dashed line) toward the beam to minimize the x-ray path through the diamond and to reduce the effects of self-absorption.

x-ray beam, through the same gasket. This configuration is shown in Fig. 3.19. Because the incident energy was tuned to the L_{III} absorption edge, however, the penetration depth of the x-ray beam into the sample is very small. For Gd the attenuation length at $\Omega = 7243$ eV is $\sim 3\ \mu m$. As a result, only a very small section of the sample, approximately one absorption length from the surface, closest to the exit side of the cell would be probed unless the geometry of the experiment was refined.

This problem was partially solved by tilting the cell by $\sim 4 - 8°$ along the 45° (see dashed line in Fig. 3.19) toward the incident beam. By angling the sample toward the crystal analyzer, we were able to collect the emitted RIXS signal from the entire top surface of the sample, increasing the physical cross-section of the sample and minimizing the effects of self-absorption. Tilting the cell also minimized the x-ray path length through the Be gasket, thus increasing not only the total flux reaching the sample but also the number of emitted photons reaching the detector.

X-ray Spectrometer and Detector

High energy x-rays interact weakly with matter and, thus, they cannot be collected by ordinary optical methods (lenses and mirrors). However, the principle of Bragg reflection allows efficient collection of x-rays using a single-crystal analyzer (see Sec. A). High resolution (below 1 eV) is possible due to the extreme sensitivity of Bragg reflection with respect to the angle of incidence for a specific crystal plane. A side effect of this extreme sensitivity, however, is that a flat crystal would only be able to collect a very small solid angle of x-rays. This is because the outlying x-rays would quickly exceed the Darwin width, or the range of angles for a given lattice plane and x-ray energy for which Bragg reflection will occur. It is also necessary to focus the collected x-rays onto a detector, which a flat crystal would not do.

The Rowland circle geometry, shown in Fig. 3.20 represents an approximate solution to the simultaneous problems of specular reflection and the Bragg condition that need to be met in order to collect and focus x-ray rays. This geometry consists of the sample, crystal analyzer, and detector all lying on a circle of radius of R_0 arranged in the vertical plane. The x-ray analyzer is a spherically bent single crystal oriented along a specific (hkl) and bent to a radius $R_c = 2R_0$ [68]. Since, however, this is only an *approximate* solution, an aberration is introduced that is proportional to the size of the crystal analyzer. The diameter of the crystal analyzers used during these experiments was ~ 4" . At this size, only aberrations smaller than the intrinsic resolution of the crystal were introduced and were not problematic.

High quality bent silicon crystals were used, however the specific (hkl) orientation used depended on the energy range to be analyzed. There are many possible lattice spacings to choose from that would satisfy the Bragg condition for a given energy within the Rowland circle geometry. It is, however, very difficult to perfectly bend a single crystal. Lattice strain

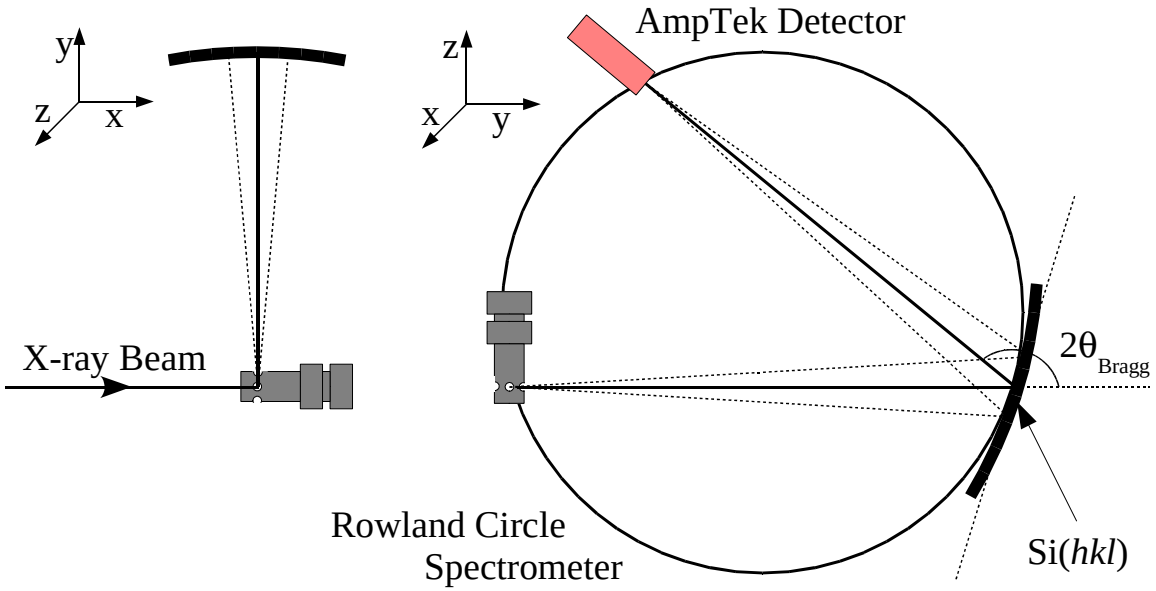

Figure 3.20. A schematic of the IXS setup at 16 ID-D of the APS. The x-rays emitted from the sample are collected at 90° from the incident beam and analyzed using a Si crystal analyzer bent to 2× the radius of the Rowland circle. The resulting signal was detected using a Si-PIN Photodiode (AmpTek).

resulting from the bending alters the spacing of the crystal planes causing deviations from in the angle, from the ideal θ_B, between the IXS such that $2\theta_B$ was closest to 180°. This is because the Darwin width, or acceptance angle of a given Bragg reflection, is maximal at $2\theta_B = 180°$. This ensured that the maximum number of photons were collected despite imperfections in the crystal analyzer. Table 3.2.5 lists the Si(hkl)s used for each material along with the target energy.

A Si-PIN Photodiode (AmpTek), connected to a multichannel analyzer, was used as the detector. A Si-PIN detector works by generating a current proportional to the energy x-ray photons which enter the detector area. An average of one electron-hole pair is created per 3.62 eV energy deposited in the Si [69]. A 100-250 V bias voltage is also applied across the Si to collect the electrons/holes. This bias voltage requires active cooling to prevent excess current leakage which would lead to noise in the signal. The efficiency of the detector

Material	Emission line	Energy eV	Si(hkl)	$2\theta_B$
Gd	$L\alpha$	6057.2	(333)	156.56°
Pr	$L\gamma_1$	6322.1		139.49°
MnO	$K\beta$	6490.45		123.07°
Nd	$L\gamma_1$	6602.1		127.89°
Gd	$L\gamma_1$	7758.80		99.24°
Ce	$L\gamma_1$	6052	(422)	134.81°
Eu	$L\gamma_1$	7480.3	(620)	149.65°

Table 3.2. Emission lines, line energies, Si (hkl), and Bragg angles for various materials used in this study.

at a given photon energy depends on the thickness of the Si. A thickness of 500 μm was used in all the experiments described in this dissertation.

3.3 Optical Spectroscopy at High Pressure

3.3.1 micro-Raman Spectroscopy

The 1930 Nobel Prize in Physics was awarded to Indian physicist Chandrasekhara Venkata Raman for his work on the scattering of light in liquids and gases. By chance, he discovered that incident monochromatic light passing through certain materials was shifted to lower energy, an effect which become known as the "Raman effect". This shifted light is due to the interaction between the incoming photons and the normal modes of vibration in the material.

Raman spectroscopy is ideally suited high pressure experiments using a DAC. Diamond is an insulator with a band gap of $E_g = 5.5$ eV[70]. It is therefore transparent in the visible light region of the electromagnetic spectrum where the optical Raman process takes place. However, the birefringence inherent to diamond rotates the polarization of the incoming and emitted light. This birefringence also changes with pressure. Hence

all Raman spectroscopy conducted at high pressure in a DAC is unpolarized. Thus, Raman spectroscopy is most useful for mapping the phase diagram of materials by observing the disappearance or appearance of Raman bands as a function of pressure. Structural determination would require single crystal, polarized Raman spectroscopy.

The Raman Effect

Figure 3.21 shows a schematic diagram of the Raman process. Monochromatic light with energy $h\nu_0$ is incident on a material with vibrational energy levels $k_1..k_\infty$ separated by ΔE. When a photon interacts with an atom in the crystal lattice, the photon is partially absorbed, causing the atom to transition to a short-lived excited state (see dashed lines in Fig. 3.21). In normal Raman, this photon does not have enough energy to cause a transition to the next highest electronic energy level. For this reason, the short-lived excited state is called a virtual state. This excited state decays by either emitting a photon of the same energy, $h\nu_0$, or shifted by an amount $h\nu_k$ corresponding to the frequency of the vibrational level. This inelastic scattering process is called Raman scattering.

The energy of the outgoing photon is $h(\nu_0 \pm \nu_k)$. If the energy is lower than the incident photon then energy was transferred to the lattice. This is called Stokes scattering. If the energy of the outgoing photon is higher than the incident photon then energy was absorbed from the lattice. This process is called anti-Stokes scattering. Both processes have the same cross section. However, the scattered intensity for the anti-Stokes process depends on the thermal occupation of the vibrational energy level. As can be seen from Fig. 3.21 the system must be in an excited vibrational energy state in order to transfer energy from the lattice to the photon.

Not all normal modes of vibration in a solid are produced Raman shifted light. In a molecule, only vibrations which produce a change in the polarizability of the molecule

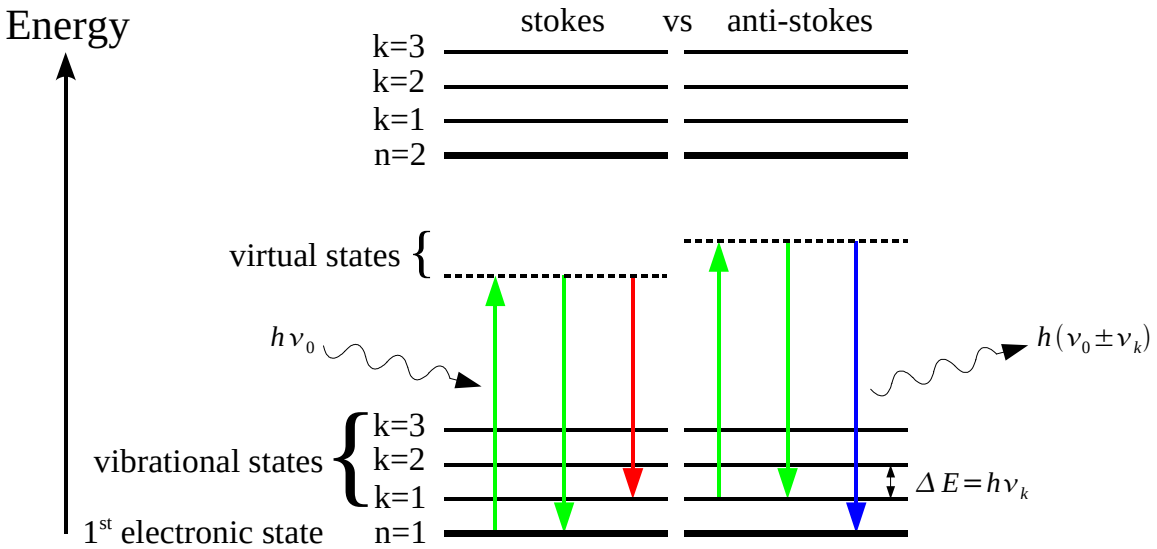

Figure 3.21. A schematic diagram of the Raman process.

along the normal mode direction produce this light (see Sec. B). These modes are called "Raman active" modes. In a crystal, it is not always intuitive which vibrations will be Raman active. However, group theory gives us a convenient method for determining the Raman active modes in a crystal of known symmetry. An in-depth review of group theory is beyond the scope of this work. However, a simple method using the character tables and correlation tables for the various symmetry elements is given in Ref. [71].

3.3.2 Instrumentation

Sir V. C. Raman had the luxury of large, macroscopic samples. His instrumentation was therefore rather simple and consisted of a 7" refracting telescope used to collect sunlight which was then monochromated with filters, collimated, and sent toward the sample. The resulting Raman light was analyzed *visually* using more filters to remove the incident monochromated sunlight. Despite using large samples and the sun as his illumination source, it took Sir Raman anywhere from 2 to 100 hours to collect a single spectrum,

depending on the material being studied. This is because only about $1X10^{-6}\%$ of the incident light is shifted by the Raman process.

However, sample sizes in a DAC are microscopic and typically range from 100 μm down to less than 50 μm in diameter. Such small samples require microscope optics to not only focus the incident beam down below the sample size but also to collect the Raman scattered light. This adds significant complexity. Additionally, samples where the penetration depth of the excitation source is small, *i.e.*, metals, require an efficient optical system able to collect as many emitted photons as possible while rejecting unwanted light generated by fluorescence (from diamond and sample/hydrostatic media). This is especially critical at high pressure since pressure normally reduced the band gap of insulating materials.

In general, an optical spectroscopy system can be broken down into four main sections: (i) illumination, (ii) beam preparation and delivery optics, (iii) signal collection and sample viewing optics, and (iv) analysis and detection. Figure 3.22 shows a schematic diagram of the con-focal micro-Raman system designed and build for this study. This system was designed for maximum signal throughput. Part of this design was to use the minimum number of components for section (iii) since each optical component placed in the path of the signal either reflects or absorbs a small percentage of the signal. The following sections describe this system in detail. It should be noted that this same system was used for fluorescence spectroscopy (Ruby fluorescence) and, with the proper choice of grating, can also be used for othe types of optical spectroscopy.

(i) Illumination Source

The ability to change the excitation wavelength is critical for both Raman spectroscopy and ruby florescence spectroscopy:

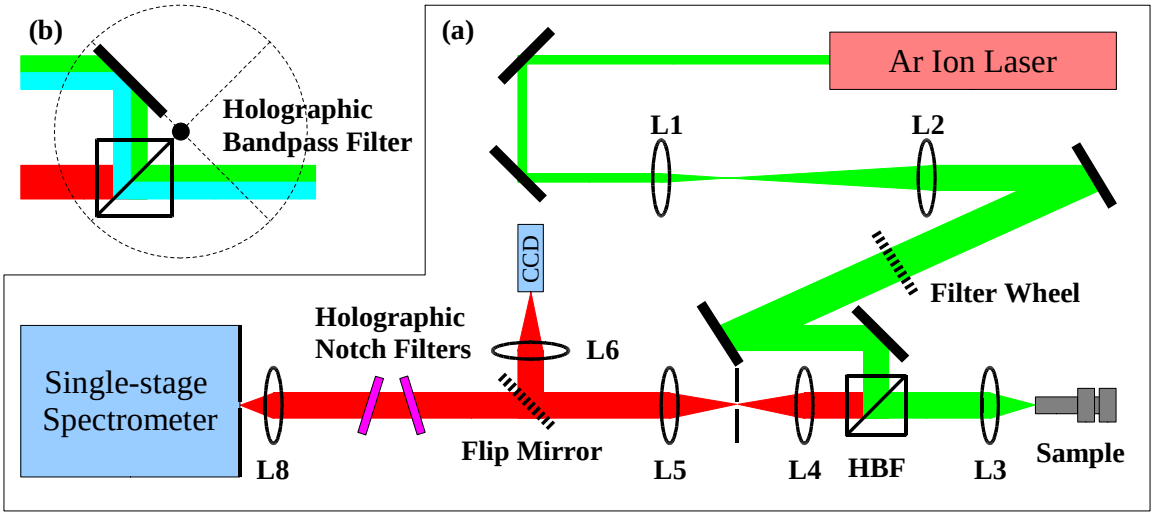

Figure 3.22. (a) A schematic diagram of the high throughput Raman spectroscopy system used in this work. (b) Shows an expanded view of the Holographic Bandpass Filter (HBF) used to send the incoming beam down the axis of the DAC and to partially remove the elastic scattering.

1. Identification of Raman peaks vs. fluorescence peaks can be performed using two difference excitation wavelengths. If a peak occurs at the same wavelength regardless of excitation wavelength then it is a fluorescence peak. If it occurs at fixed Raman shift then it is a Raman peak.

2. The Raman scattered intensity goes as $\sim 1/\lambda^4$ where λ is the excitation wavelength. Thus, signal can be increased by moving to higher energy (shorter wavelength) excitation

3. The ruby fluorescence excitation mechanism shifts to higher energy with pressure.

Hence, a Spectra Physics Stabilite 2017 Argon Ion laser was used as our excitation source. A variety of lasing wavelengths can be selected by rotating a prism on the back of the laser head. The possible wavelengths of operation are listed in Table 3.3.2 along with the maximum output in single-line mode for each wavelength [72]. In addition to the increase in Raman signal from using a shorter wavelength excitation, the ability to choose higher energy excitations is advantageous when measuring ruby florescence for pressure

Wavelength	Max. Power
454.5 nm	100 mW
457.9 nm	200 mW
465.8 nm	120 mW
472.7 nm	170 mW
476.5 nm	450 mW
488.0 nm	1.5 W
496.5 nm	600 mW
501.7 nm	300 mW
514.5 nm	2.0 W
647.1 nm	500 mW
676.4 nm	120 mW

Table 3.3. Available single-mode wavelengths along with the maximum output power at that given wavelength for the Spectra-Physics Stabilite 2017 Argon Ion Laser.

determination (see Sec. 3.1.5).

(ii) Beam preparation and delivery optics

The output beam of the Stabilite 2017 at 514nm has very low divergence (0.5 mrad) and for our purposes is considered collimated [72]. However, it was necessary to expand the beam to achieve a smaller focus. The beam waist, w, of a Gaussian beam of diameter D focused by a lens of focal length f is given by the expression

$$w = \frac{1.27\lambda f}{D} \tag{3.7}$$

where λ is the wavelength of the beam. Equation 3.7 shows that both a shorter focal length objective and a larger diameter beam will produce a smaller beam waist. Unfortunately, the dimensions of the *LLL* DAC put limitations on f. To achieve the desired spot size (< 5 μm) it was necessary to increase D from its initial value of 1.4 mm [72]. This was accomplished using a pair of achromatic lenses (L1 and L2 in Fig. 3.22) of focal lengths f_1 and f_2, respectively. An expanded, collimated beam was produced by spacing the lenses such that the focal point of L1 lay in the focal plane of L2. This will happen when the

distance between L1 and L2 is $f_1 + f_2$. The magnification of the beam is then $m = f_2/f_1$. The condition $m > 1$, *i.e.*, enlargement, is satisfied when $f_2 > f_1$. We chose f_1 and f_2 such that $m = 4$, producing a collimated beam of diameter $D = 5.6$ mm.

We used a 180° backscattering geometry, *i.e.*, the incident beam was coaxial with the collection optics. This is opposed to the common 135° backscattered geometry where the incident beam enters at an angle of 45° to the axis of the cell. This latter method has some benefits. Much of the elastic scattered light from the table of the diamond and from the sample never makes in into the collection optics, making removing the Rayleigh scattered line from the Raman spectra much easier. Also, because the incident beam enters off-axis, less of the fluorescence generated in the diamond anvil makes it into the collection optics. However, this method produces an elongated illumination spot. Due to the limited space between the cell and the collection optics, this method also prevents using the short focal length objectives needed to produce a small laser spot. The 180° backscattering geometry produces a very small, circular spot by sending the collimated incident beam through the collection optics. Using a Mitutoyo infinity corrected 20X microscope objective for signal collection (L3 in Fig. 3.22), with a working distance of 20.0 mm, an approximate spot size of $w = 2.3\ \mu m$ was achieved (see Eq. 3.7).

The 180° geometry required an additional set of optics to position the collimated laser beam along the axis of the main objective. The 30/70 beam splitter typically used for this purpose reflects 30% of the laser beam and allows 70% to pass through. However, this means that 30% of the collected signal is also reflected out of the collection optics path. This is unacceptable for use in a system designed for maximum signal collection. For this reason, we used a holographic bandpass cube (Kaiser Optical Systems, Inc.) to diffract the incoming laser down the axis of the main objective. The configuration shown in Fig. 3.22(b) allowed the selection of different laser lines by rotation of the mirror/cube assembly.

The bandbass cube also removed the laser plasma lines and much of the Rayleigh scattered light from the sample (the spectral bandpass is < 2 nm).

(iii) Signal collection and sample viewing optics

The signal collection lens (L2 in Fig. 3.22) was an infinity corrected Mitutoyo 20X microscope objective. An infinity corrected lens is optimized for producing collimated light behind the objective, forming an image at infinity. This is opposed to a standard microscope objective that forms an image 16cm to 21cm behind the objective. Infinity corrected optics allow the freedom to place optics behind the objective that were designed to work with collimated light, such as filters and beam splitters, without needing a collimating lens. This is especially critical when using the 180° backscattered geometry, sending the laser through the microscope objective. One could form an image of the laser at the image plane of a standard microscope object to achieve the same results. However, this is cumbersome and difficult to align.

A flip-mirror was used to divert the signal light onto a standard CCD video camera when visual inspection of the sample was needed. The mirror was flipped out of the optical path when taking Raman spectra. This configuration is more efficient than the commonly used fixed beam splitter which typically diverts as much as 30% of the signal for viewing. Because the light coming out of the microscope objective is parallel, a secondary lens (referred to as a "tube lens") was needed to form an image onto the CCD (L6 in Fig. 3.22). The Mitutoyo objective used only achieves a 20X magnification when coupled with a 200 mm focal length tube lens. A longer focal length tube lens can be used to achieve a greater magnification, and vice versa. At 20X magnification, a 300 μm culet would appear 6 mm in diameter, very close to the 6.096 mm (1/4") CCD used. Therefore, we used the standard magnification and employed a 200 mm focal length tube lens.

Low fluorescence diamonds are helpful, but not always sufficient, in reducing the background during optical spectroscopy experiments at high pressure. Hence, a spatial filter was used to discriminate against diamond fluorescence. This consisted of a pair of achromatic lenses (L4 and L5 in Fig. 3.22) of focal lengths f, placed a distance $2f$ apart to preserve collimation. An adjustable aperture was then placed at the focal point between L4 and L5. A ray diagram showing this device and how it rejects stray light is shown in Fig. 3.23. Parallel light coming from the in-focus sample is focused by the first lens, through a narrow aperture. Light coming from in front of and behind the object plane, i.e. fluorescence from the diamond anvils, will not be in focus. These non-parallel rays of light are focused either behind or in front of the aperture. In this way, most of the light entering the microscope objective, not emanating from the sample, is blocked by the aperture. A smaller aperture rejects more stray light at the expense of sample signal. The spatial filter was positioned before the flip mirror, making sure the image of the sample and aperture are in focus at the same time. The aperture size was set by closing the aperture until only the sample region we wish to probe was visible in the CCD image.

A pair of holographic notch filters (Kaiser Optical Systems, Inc. Holographic Supernotch) were used to remove as much of the Rayleigh scattered light as possible. This is especially important when using the 180° backscattered geometry. Each filter has an optical density of > 4.0 for a combined optical density of > 8.0 at 514.5 nm. The wavelength of the central notch can be tuned by changing the angle of the filters with respect to the incoming beam. In this way, one can tune the pair as close to the Rayleigh line as possible. The experimentally determined limit for our system is ~ 120 cm^{-1} and is dictated by the edge width of the filter (the steepness or sharpness of the notch). The factory determined edge width for the Holographic Supernotch is < 150 cm^{-1} which is consistent with our results.

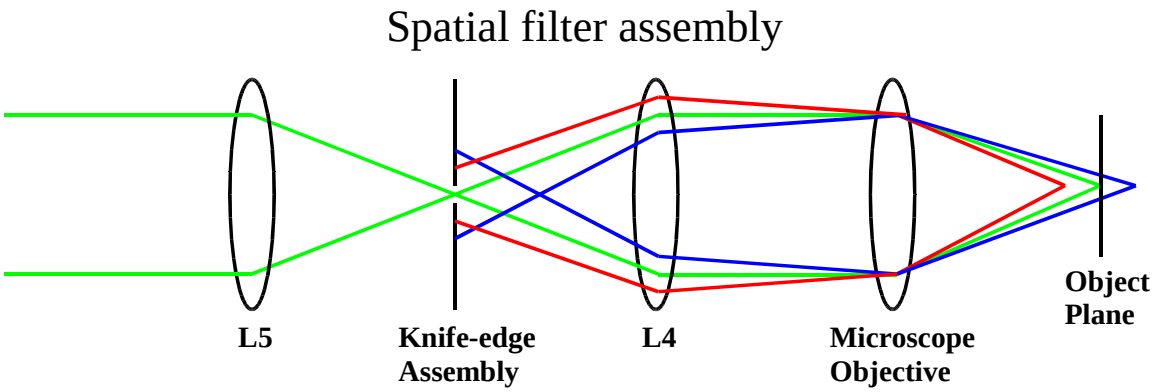

Figure 3.23. A schematic diagram of the spatial filter assembly used in the high sensitivity Raman system. Non-parallel light rays, coming from outside the sample plane resulting from diamond fluorescence, are focused by L4 and sent through a knife-edge assembly. These rays come to a focus at different points. As a result, only rays coming from the object plane are able to pass. The signal is then re-collimated by L5.

(iv) Signal Analysis and Detection

We used an HR460 single spectrometer coupled to a liq.-N_2-cooled CCD detector (Princeton Instruments) for signal analysis and detection. The word "single" refers to the number of dispersive elements. We used a holographic grating blazed at 500 nm. A double spectrometer has two dispersive elements in succession to achieve a higher resolution. A triple spectrometer is really a single spectrometer with the addition of a bandpass filter stage. The two additional gratings are used (one using $m = 1$ order reflections and the other using $m = -1$ order, such that the net dispersion is zero) to filter the Rayleigh scattered light, usually getting as close as 50 cm^{-1} from the Rayleigh line. However, the efficiency of a triple spectrometer is much lower than that of a single spectrometer due to the additional gratings. This is because a typical holograph grating is only 50% efficient. Therefore, a single grating spectrometer, together with a pair of holographic notch filters (with a typical transmittance of $> 85\%$ a piece) is preferred when very low Raman-shift information is not required.

3.4 Experimental Details

All experiments described in this work were performed at either Lawrence Livermore National Laboratory or the APS at Argonne National Laboratory. Raman spectroscopy was done at Livermore in the Raman Lab of the High Pressure Physics Group. Synchrotron x-ray diffraction and IXS experiments were done at sectors 16 ID-B and 16 ID-D, respectively. Sample loading was done primarily in Livermore except in cases where the samples prepared in advance failed at the beam line and were reloaded, as was the case for Nd and Eu. The following sections describe each individual experiment as well as sample loading details.

3.4.1 MnO

ADXRD

Angle-dispersive x-ray diffraction was performed on MnO (99%, Alfa Aesar) up to 161 GPa using 0.3678 Å x-rays focused to $\sim 10 \times 10\ \mu m$.

One sample of powdered MnO (99%, Alfa Aesar) was loaded into a LLL cell fitted with 300-100 μm beveled culet diamonds. A Re gasket with a 50 μm sample chamber was used. Mineral oil was loaded as the pressure medium and ruby chips were used as pressure standards.

XES

X-ray emission spectroscopy was performed on MnO to 161 GPa using $\Omega = 10.225$ keV x-rays, focused to $\sim 20 \times 50\ \mu m$ at the sample, incident along the axial direction. The $K\beta$ XES signal at 6490.45 eV was then collected though a Be gasket at 90° from the incident x-ray. The x-ray analyzer was a bent Si crystal oriented along the (333) direction

giving a value of $2\theta_B = 123.07°$ at 6490.45 eV.

One sample of powdered MnO (99%, Alfa Aesar) was loaded into a LLL cell fitted with 300-100 μm beveled culet diamonds. A standard Be gasket with a 50 μm sample chamber was used. Mineral oil was loaded as the pressure medium and ruby chips were used as pressure standards. The pressure gradient was estimated to be ~ 3 GPa across the 20 μm (shrunk from 50 μm) sample at 100 GPa.

3.4.2 Gd

RIXS

Resonant inelastic x-ray scattering was performed on Gd to 113 GPa. The incident x-ray energy was tuned through the L_{III} edge from $\Omega = 7235$ eV to 7257 eV in steps of 2 eV, incident through a Be gasket. The $L\alpha_1$ emission at 6057.2 eV was then collected 90° from the incident beam through the same Be gasket. The cell was also tilted to $\sim 7°$ from the horizontal plane to increase the physical cross section of the sample and to minimize the effects of self-absorption. The x-ray analyzer was a bent Si crystal oriented along the (333) direction giving a value of $2\theta_B = 156.56°$ at 6057.2 eV.

Two samples of Gd foil (99%, Alfa Aesar) were loaded into LLL cells fitted with either 300 μm culet diamonds (for pressures < 60 GPa) or 300-100 μm beveled culet diamonds (for pressures > 60 GPa). A standard Be gasket with either a ~ 120 μm sample chamber (for 300 μm culets) or a 50 μm sample chamber (for 300-100 μm beveled culets) was used. Mineral oil was loaded as the pressure medium and ruby chips were used as pressure standards. Samples were loaded in air, under oil, and cut from the foil using a stainless steel blade.

XES

X-ray emission spectroscopy was performed on Gd to 106 GPa using $\Omega = 12$ keV x-rays, focused to $\sim 20 \times 50\ \mu m$ at the sample, incident along the axial direction. The $L\gamma_1$ XES signal at 7785.8 eV was then collected though a Be gasket at 90° from the incident x-ray. The x-ray analyzer was a bent Si crystal oriented along the (333) direction giving a value of $2\theta_B = 99.24°$ at 7785.8 eV.

Two samples of Gd foil were loaded into LLL cells fitted with either 300 μm culet diamonds (for pressures $<$ 60 GPa) or 300-100 μm beveled culet diamonds (for pressures $>$ 60 GPa). A standard Be gasket with either a $\sim$ 120 μm sample chamber (for 300 μm culets) or a 50 μm sample chamber (for 300-100 μm beveled culets) was used. Mineral oil was loaded as the pressure medium and ruby chips were used as pressure standards. Samples were loaded in air, under oil, and cut from foil using a stainless steel blade.

3.4.3 Nd

XES

X-ray emission spectroscopy was performed on Nd to 108 GPa using $\Omega = 12,005$ keV x-rays, focused to $\sim 20 \times 50\ \mu m$ at the sample, incident along the axial direction. The $L\gamma_1$ XES signal at 6602.1 eV was then collected though a Be gasket at 90° from the incident x-ray. The x-ray analyzer was a bent Si crystal oriented along the (333) direction giving a value of $2\theta_B = 127.89°$ at 6602.1 eV.

Two samples of Nd were loaded into LLL cells fitted with either 300 μm culet diamonds (for pressures $<$ 60 GPa) or 200 μm culet diamonds (for pressures $>$ 60 GPa). Standard Be gaskets with 80 μm sample chambers were used for both cells. Mineral oil was loaded as the pressure medium and ruby chips were used as pressure standards. Samples

were loaded in air, under oil, and obtained by using a stainless steel razor blade to shave pieces of metal from the ingot. Care was taken to remove the surface oxide layer from the ingot before obtaining sample shavings.

3.4.4 Pr

XES

X-ray emission spectroscopy was performed on Nd to 21 GPa using $\Omega = 12,005$ keV x-rays, focused to $\sim 20 \times 50\ \mu m$ at the sample, incident along the axial direction. The $L\gamma_1$ XES signal at 6322.1 eV was then collected though a Be gasket at 90° from the incident x-ray. The x-ray analyzer was a bent Si crystal oriented along the (333) direction giving a value of $2\theta_B = 139.49°$ at 6322.1 eV.

Two samples of Pr were loaded into LLL cells fitted with either 300 μm culet diamonds or 200 μm culet diamonds. One cell (300 μm culets) used a Standard Be gasket with a sample chamber of 80 μm. The second cell (200 μm culets) used an amorphous boron gasket insert to prevent the tails of the x-ray beam from clipping the sides of the Be gasket (see Sec. 3.1.3). Mineral oil was loaded as the pressure medium and ruby chips were used as pressure standards. Samples were loaded in air, under oil, and obtained by using a stainless steel razor blade to shave pieces of metal from the ingot. Care was taken to remove the surface oxide layer from the ingot before obtaining sample shavings.

3.4.5 Ce

XES

X-ray emission spectroscopy was performed on Ce to 21 GPa using $\Omega = 14.432$ keV x-rays, focused to $\sim 20 \times 50\ \mu m$ at the sample, incident along the axial direction. The

$L\gamma_1$ XES signal at 6052 eV was then collected though a Be gasket at 90° from the incident beam. The x-ray analyzer was a bent Si crystal oriented along the (422) direction giving a value of $2\theta_B = 134.81°$ at 6052 eV.

One sample of Ce was loaded into a LLL cell fitted with 500 μm culet diamonds. Large culets were used to allow fine control of pressures below 1 GPa ($\gamma \rightarrow \alpha$ transition in Ce occurs at 0.7 GPa) and to maximize the thickness of the sample. A small diameter (3 mm) standard Be gasket with a 180 μm sample chamber was also used. A wide sample chamber and thick gasket maximized the XES signal. Mineral oil was loaded as the pressure medium and ruby chips were used as pressure standards. Samples were loaded in air, under oil, and obtained by using a stainless steel razor blade to shave pieces of metal from the ingot. Care was taken to remove the surface oxide layer from the ingot before obtaining sample shavings.

3.4.6 CrO_2

ADXRD

Angle-dispersive x-ray diffraction was performed on CrO_2 up to 50 GPa using $\lambda = 0.3680$ Å x-rays focused to $\sim 12 \times 12$ μm. LeBail whole-profile fitting was used to obtain lattice parameters and profile coefficients. A Rietveld refinement was then performed to obtain internal oxygen coordinates. Background removal was done manually due to a very irregular amorphous background that was difficult to fit.

Two samples of powdered CrO_2 (Magtrieve by duPont) were loaded into LLL cells fitted with 300 μm culet diamonds. Both cells used Re gaskets with either a 130 μm sample chamber or a 160 μm sample chamber. The first cell (130 μm sample chamber) used mineral oil as a pressure medium and Au powder as the pressure standard. The second sample used cryogenically loaded He as a pressure medium (see Sec. 3.1.4) and ruby chips as pressure

standards. A larger sample hole was used to allow for the 30% volume compression of the liq.-He upon loading.

Raman Spectroscopy

Raman spectroscopy was performed on CrO_2 to 42 GPa using the confocal micro-Raman system described in Sec. 3.3.2. Previous Raman attempts using a conventional Raman setup produced sample heating due to the high (100-200 mW) laser powers required and caused oxidation from CrO_2 to Cr_2O_3 [73]. The con-focal Raman system described in Sec. 3.3.2 reduced the collection time to five minutes using only < 30 mW at 514.5 nm.

One sample of powdered CrO_2 (Magtrieve by duPont) was loaded into a *LLL* cell fitted with 300 μm culet diamonds. A Re gasket with a 140 μm sample chamber was used. Cryogenically loaded Ar was used as the pressure medium and ruby chips were used as pressure standards. Mineral oil was not used due to a broad, amorphous background generated during previous Raman attempts. Helium was also not used due to the high initial loading pressures required to ensure liq.-He capture.

Chapter 4

Results

4.1 MnO

4.1.1 XES

Results from $K\beta$ XES on MnO are shown in Fig. 4.1, overlaid in three groups depending on pressure. The first group shows all spectra below 30 GPa. These spectra agree well with ambient condition $K\beta$ emission on MnO [74] and consist of the main $K\beta_{1,3}$ peak at 6492 eV and a low energy $K\beta'$ satellite peak at 6477 eV, a separation of 15 eV. The second group of spectra were taken between 40 and 98 GPa and show a noticeably reduced, but still apparent $K\beta'$ intensity. The third group of spectra were taken 108 GPa and above. This last group of spectra show no identifiable $K\beta'$ peak. A 2 eV shift to lower energy is also seen for the $K\beta_{1,3}$ peaks as one moves from one group to another. A similar shift of the $K\beta_{1,3}$ peak was also observed in FeO, but was unexplained [14].

Figure 4.2 shows the pressure dependence of both the $K\beta_{1,3}$ peak position and the normalized $K\beta'$ peak intensity I'/I, or the branching ratio. The branching ratio was obtained by subtracting the 132 GPa spectrum from each lower pressure spectra after

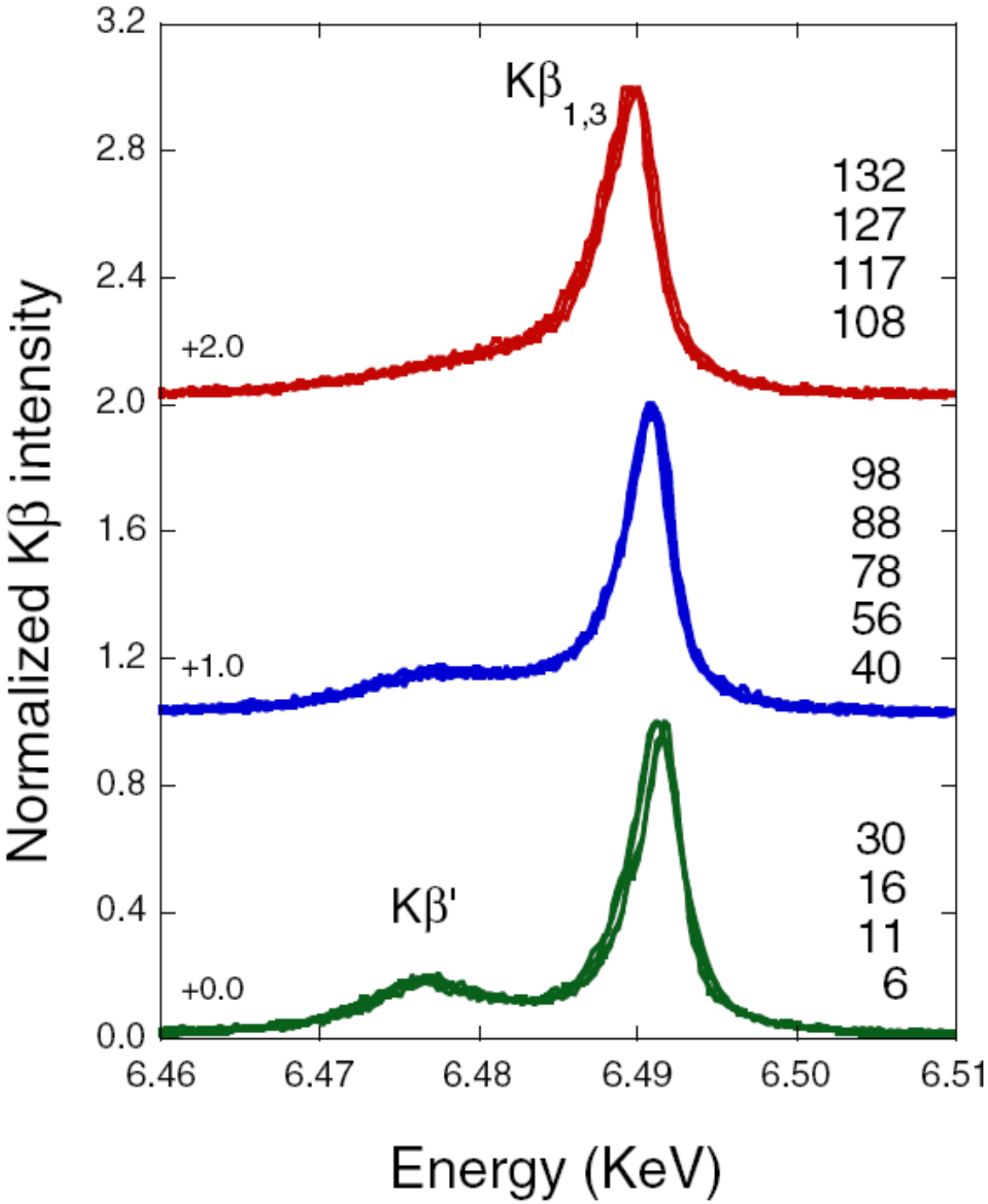

Figure 4.1. $K\beta$ x-ray emission branches of MnO at high pressures (all in GPa), showing subtle spectral changes in the $K\beta_{1,3}$ peak positions and the $K\beta'$ intensities above 30 GPa and 98 GPa (also see in Fig. 4.2). The absence of a $K\beta'$ peak above 108 GPa is consistent with a loss of the magnetic moment.

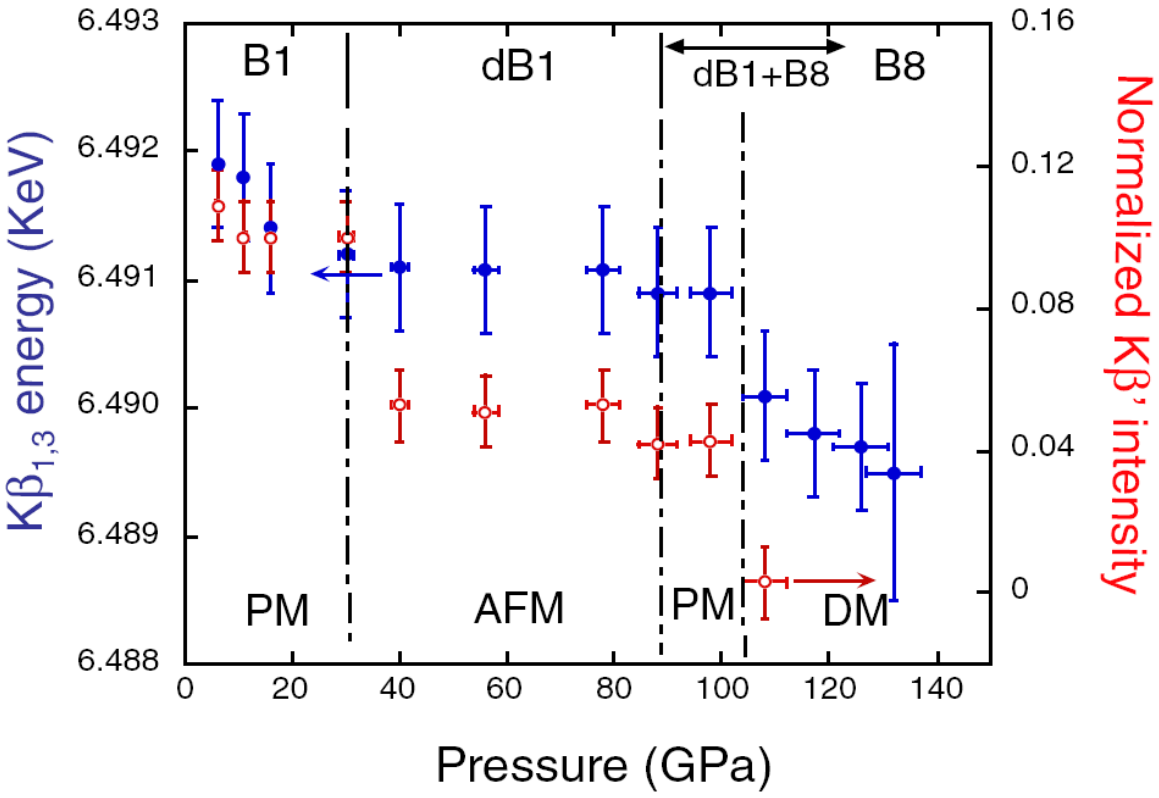

Figure 4.2. The pressure-induced spectral changes of MnO, illustrating three first-order electronic phase transitions at 30, 90, and 108 GPa. The first two correspond to the $B1$ (PM) to $dB1$ (AFM) and the $dB1$ to $B8$ (PM) transitions, respectively, whereas the third occurs within the $B8$ structure and corresponds to a transition to a Pauli paramagnetic state at 108 GPa.

first normalizing all spectra by the $K\beta_{1,3}$ peak intensity. Three discontinuous changes are evident in both diagnostics: the first near 30 GPa at the onset of the $B1$ (PM) to $dB1$ (AFM) phase transition, then near 90 GPa, and finally 108 GPa representing the vanishing of the $K\beta'$ peak. The third electronic phase transition near 108 GPa occurs above the 90 GPa transition reported in Ref. [4], where the $dB1$ phase transforms to an unknown intermediate phase, but below 120 GPa, where the intermediate phase transforms to the $B8$ phase. The resolution of this apparent discrepancy between our data and those from the literature will require proper characterization of the intermediate phase region.

Considering Eqs. 3.5 and 3.5 from Sec. 3.2.3, the vanishing $K\beta'$ peak intensity

at 108 GPa in MnO is consistent with a loss of the $3d$ magnetic moment. We also suggest that the 90 GPa signature in our data and in Ref. [4] corresponds to the AFM to PM transition as described for FeO [14]. Hubbard model calculations [75] show that the local moment is reduced with increasing antiferromagnetic correlations (decreasing temperature) at strong coupling. At weak coupling, the local moment behaves the opposite way. If these correlations change discontinuously across the AFM phase lines, one would expect the moment for compressed MnO to drop both on entering the AFM region at 30 GPa (strong coupling) and again leaving the AFM region at 90 GPa (weaker coupling). This is indeed what we have observed in the $K\beta'$ intensity shown Fig. 4.2.

4.1.2 X-ray Diffraction

The high pressure x-ray diffraction results on MnO are summarized in Fig. 4.3. At low pressures, the diffraction pattern matches well with the $B1$ (rocksalt) structure, as demonstrated by the Reitveld refinement. At 30 GPa MnO transforms from the $B1$ to the $dB1$ structure. Around 120-130 GPa, MnO is entirely in the $B8$ structure. Both transitions are consistent with the previous high pressure work by Kondo *et al.* [4].

The intermediate phase, which was left unresolved in Ref. [4], occurs between 90 and 120 GPa. Our results reveal that this intermediate phase is actually a mixture between the $dB1$ and $B8$ phases. All diffraction lines present at 90 GPa are accounted for with either $dB1$ or $B8$ indexing. The one exception is a peak near the broad (102) reflection of $dB1$. However, this broad feature can be understood in terms of a superlattice reflection (1/2, 1/2, 5/2) near the (102) reflection, arising from lattice distortion across the displacive $dB1$ to $B8$ phase transition.

Figure 4.4 shows the specific volume and c/a ratio (inset) verses pressure for MnO, derived from our data. The lack of a discontinuity in the specific volume and c/a ratio in the

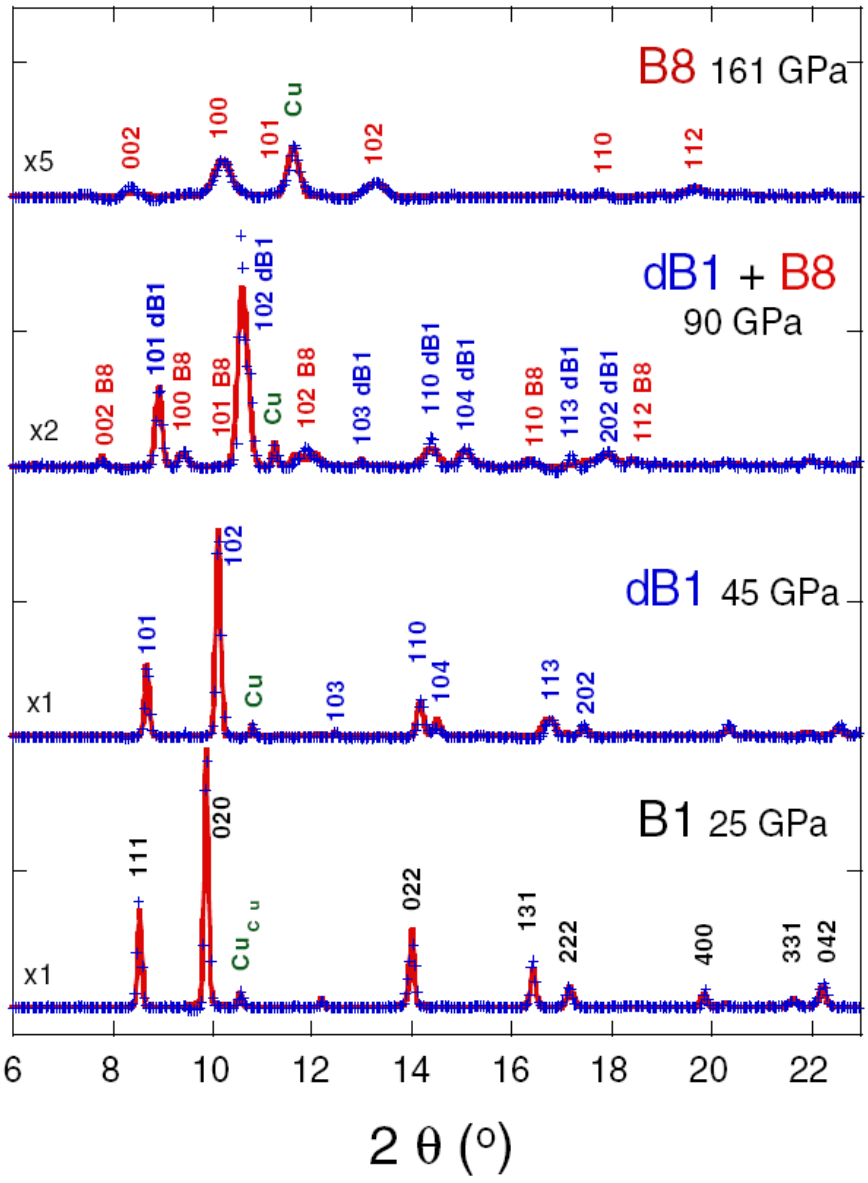

Figure 4.3. The measured (blue crosses) and refined (red lines) x-ray diffraction patterns of MnO phases. Miller indices are marked for each phase, together with the (111) reflection of the Cu used as an internal pressure marker.

$dB1$ structure at 90 GPa provides a stringent test of our interpretation of the mixed-phase region, and validates our conclusion. Note that the $B8$ phase has nearly the same specific volume as the $dB1$ to 90 GPa, becoming $\sim 4.5\%$ denser by 110 GPa. However, the most striking feature is a discontinuous volume change of $\sim 6.6\%$ at 110 GPa within the $B8$ phase, *i.e.*, a first-order isostructural volume-collapse transition. A similar discontinuous change is also seen in the c/a ratio of the $B8$ structure (Fig. 4.4, inset), providing further support for the isostructural nature of the transition.

4.2 Rare-earth Metals

4.2.1 Gd RIXS

The RIXS spectrum obtained at low pressure is qualitatively similar to that obtained by Krisch *et al.* on $Gd_3Ga_5O_{12}$ garnet at ambient pressure. Figure 4.5 shows one of these sets of spectra taken at 18 GPa, converted from emission energy to energy transfer $(\Omega - \omega)$ (see Sec. 3.2.4). The main features of the spectra are illustrated in Fig. 4.5(inset). The strongest peak (Peak B, blue shaded) resonates at $\Omega = 7247$ and occurs at $(\Omega - \omega) = 1186$ eV. This peak is the result of the strong dipole-allowed (often referred to as an E1 transition where $\Delta l = \pm 1$ [65]) $2p \rightarrow 5d$ (blue arrow) transition, which forms the $\underline{2p}4f^n(5d6s)^{v+1}$ intermediate state (see Sec. 3.2.4). The much smaller peak (Peak A, red shaded), occuring at $(\Omega - \omega) = 1180$ eV, resonates at a lower incident energy of $\Omega = 7239$ eV. This peak is due to the much weaker non-dipole allowed (E2) $2p \rightarrow 4f$ transition to the $\underline{2p}4f^{n+1}(5d6s)^{v}$ intermediate state. This latter feature illustrates the power of RIXS in resolving weak quadrupolar features normally hidden in x-ray absorption spectroscopy by the much stronger core-hole broadened $2p \rightarrow 5d$ absorption. The broad peak at $(\Omega - \omega) \sim 1191$ eV (Peak B*) exhibits the same resonance characteristics as peak B and is therefore part of

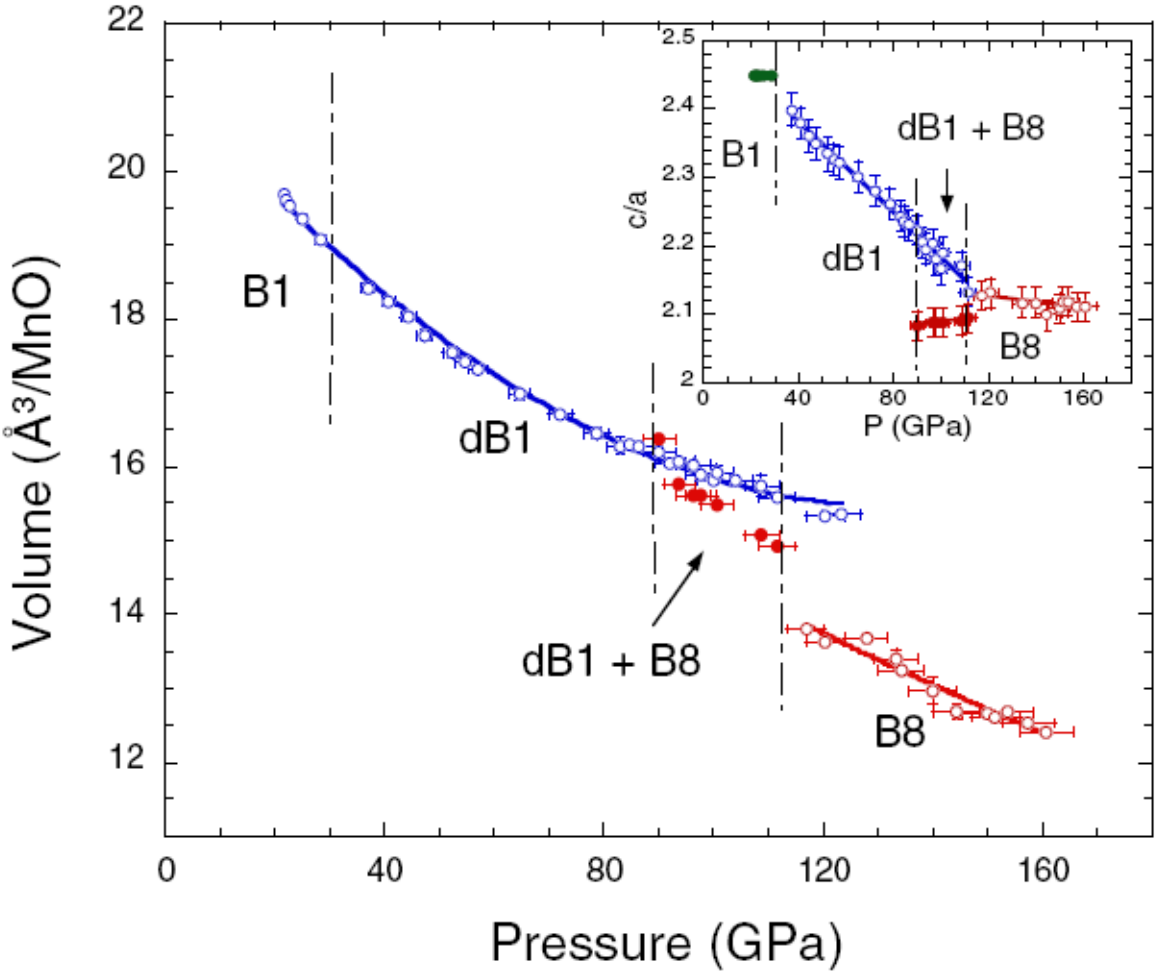

Figure 4.4. The specific volume and the c/a ratio (inset) of MnO phases as a function of pressure. Note the discontinuous changes of the specific volume and the c/a ratio at 110 GPa, indicating that MnO undergoes an isostructural phase transition with 6.6% volume collapse. This transition coincides within experimental uncertainties with the moment loss (see Fig. 4.2 and the insulator-metal transition in Ref. [5]).

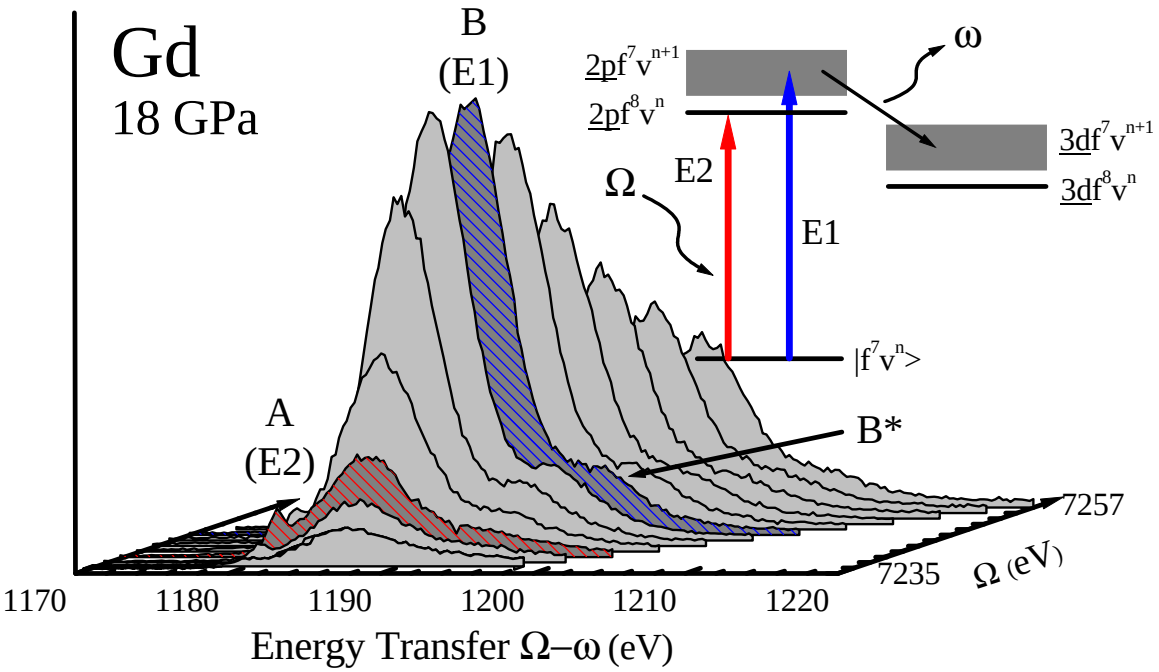

Figure 4.5. RIXS spectra of Gd at 18 GPa taken at a series of incident energies from $\Omega = 7235$ eV to $\Omega = 7257$ eV in steps of 2 eV. The inset shows a schematic energy diagram illustrating the RIXS process for the $2d \rightarrow 4f$ (E2, peak A) and $2p \rightarrow 5d$ (E1, peaks B and B*) features.

the same multiplet [76]. Peak B also shows a slight shift with increasing incident energy due to a strong crystal field. This crystal field produces two multiplet groups separated by ~ 1 eV which resonate at slightly different Ω. Incident energies above $\Omega = 7247$ eV correspond to excitations into continuum states and represent non-resonant XES.

However, significant changes in the RIXS spectra occur at increased compression . These changes are illustrated in Fig. 4.6(a) which shows a series of emission spectra taken at $\Omega = 7239eV$. Gaussian decompositions of these spectra reveal a new feature (peak C), positioned 4.96 eV below peak B, emerging at high pressure. The energy, intensity, and bandwidth characteristics of this new peak are strikingly similar to those observed during RIXS measurements of the pressure-induced valence change in YbS (f^{14} in Yb^{2+} and f^{13} in Yb^{3+}) [77], as well as during RIXS measurements of the γ-α transition in the Ce alloys

[9, 78].

The situation is illustrated by the ground-state wavefunction

$$|\Psi\rangle = \alpha|4f^7v^3\rangle + \beta|4f^8v^2\rangle + \gamma|4f^6v^4\rangle \tag{4.1}$$

of the rare-earths, where v represents the valence electrons. In the strongly localized limit, the occupation of the $4f$ shell in Gd is pinned at f^7. Under compression, however, the growing f-valence hybridization increasingly favors fluctuations of the $4f$ electrons into valence states, and vice versa. The result of this hybridization is growth of the f^6 and f^8 components of the wavefunction at the expense of the predominant f^7 character. This type of delocalization differs from ordinary intermediate valence, where one stays near the localized limit except that the energies of two different f occupations happen to move closer together as a function of a variable such pressure. Nevertheless, the RIXS process for these two phenomena are similar. The $4f$core-hole attraction in the intermediate state places the peak arising from dipole excitation of the component with larger f occupation ($\underline{2p}4f^8v^3$, peak C) at lower energy transfer than that of the smaller occupation ($\underline{2p}4f^7v^4$, peak B). Indeed, the interpretations and relative locations of all three peaks, A, B , and C, in the present study are consistent with the YbS intermediate valence case (Fig. 4b, [77]).

Using the ground state wavefunction given in Eq. 4.1, the progress of $4f$ hybridization can be quantified by the ratio $|\beta|^2/|\alpha|^2 \approx n(f^8)/n(f^7)$. This ratio can be approximately extracted from the RIXS data by subtracting the lowest pressure $\Omega = 7239$ eV spectrum from each of the higher pressure $\Omega = 7239$ eV scans, after first normalizing the total area of each spectrum. Figure 4.6(b) illustrates this procedure by showing the difference spectrum at 113 GPa along with the four $\Omega = 7239$ RIXS scans from Fig. 4.6(a), after normalization. The positive peak in the difference spectra was integrated to derive the area, $\mathcal{A}$, and the quantity $n(f^8)/n(f^7) \approx \mathcal{A}/(1-\mathcal{A})$ was then calculated. The results are plotted in Fig. 4.7

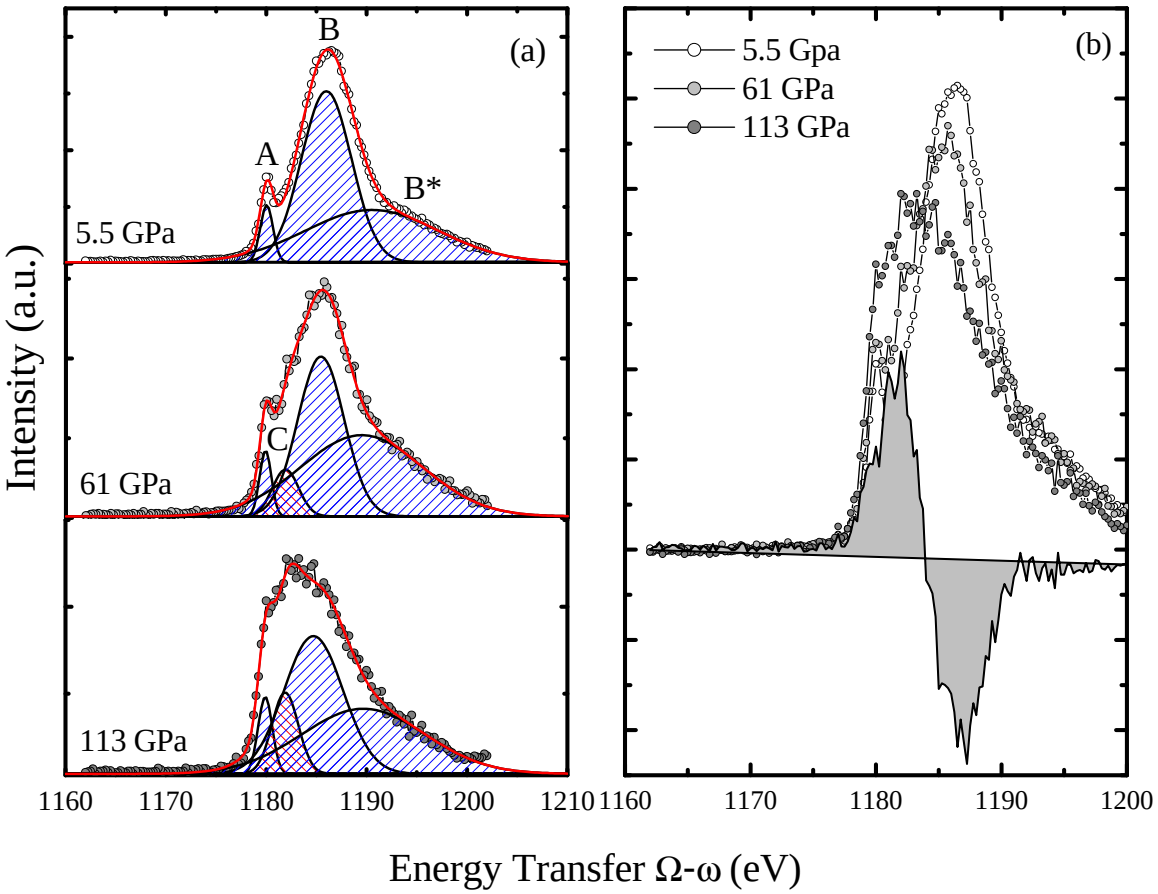

Figure 4.6. (a) RIXS spectra obtained at the $2p \rightarrow 4f$ resonance($\Omega = 7239$ eV) taken at 5.5 GPa, 61 GPa, and 106 GPa, together with Gaussian decompositions showing the emergence of a new feature (peak C) at high pressure. (b) normalized RIXS spectra at the same three pressures along with the difference spectrum (shaded) between 113 GPa and 5.5 GPa.

as a function of volume, along with recent dynamical mean-field theory (DMFT) calculation for Ce [10] and experimental values for the ambient- pressure α and γ phases of Ce alloys also obtained from RIXS [9]. In both cases (Gd and Ce alloys) the volume-collapse regions are shaded. Our data shows an approximately continuous, exponential dependence on volume as predicted by theory [10]. It is interesting to note that the $n(f^{n+1})/n(f^n)$ ratio for Gd ($n = 7$) lies far below that of Ce ($n = 1$) and its compounds. Our method of extracting the f-occupancy ratio ignores any f^6 contribution to the difference spectra, which would occur at higher energy. Unfortunately, this component could not be resolved from our data. Nevertheless, even if $|\gamma|^2 \approx |\beta|^2$, this would lead to at worst a 25% error in $n(f^8)/n(f^7)$. With only minor effects on a semi-log scale, this would have no impact on our conclusions.

4.2.2 XES on Gd, Ce, Pr, and Nd

Gd

We have also examined the f-electron moment using $4d \rightarrow 2p$ $L\gamma_1$ XES measurements on Gd at high pressure. The results are summarized in Fig. 4.8. At ambient pressure, the XES spectrum consists of the main $L\gamma_1$ line at 7786 eV, and the low energy $L\gamma_1'$ satellite peak at 7762 eV, a separation of 24 eV. We find no significant change in the $L\gamma_1$ emission spectra, *i.e.*, no changes in the branching ratio, up to our maximum pressure of 106 GPa. This result suggest there were no changes in the $4f$ moment up to this pressure and, in particular, no changes across the collapse transition at 59 GPa (see Sec. 3.2.3). This behavior is in contrast to the essentially complete loss of Mn $3d$ moment across the Mott transition in MnO as probed by similar $3p \rightarrow 1s$ $K\beta$ XES measurements (see Sec. 4.1.1) [47]. Figure 4.8(inset) shows the relative height of the satellite peak to the main peak obtained from *ab initio* atomic calculations by M.-H. Chen (LLNL) of the XES process for Gd, carried

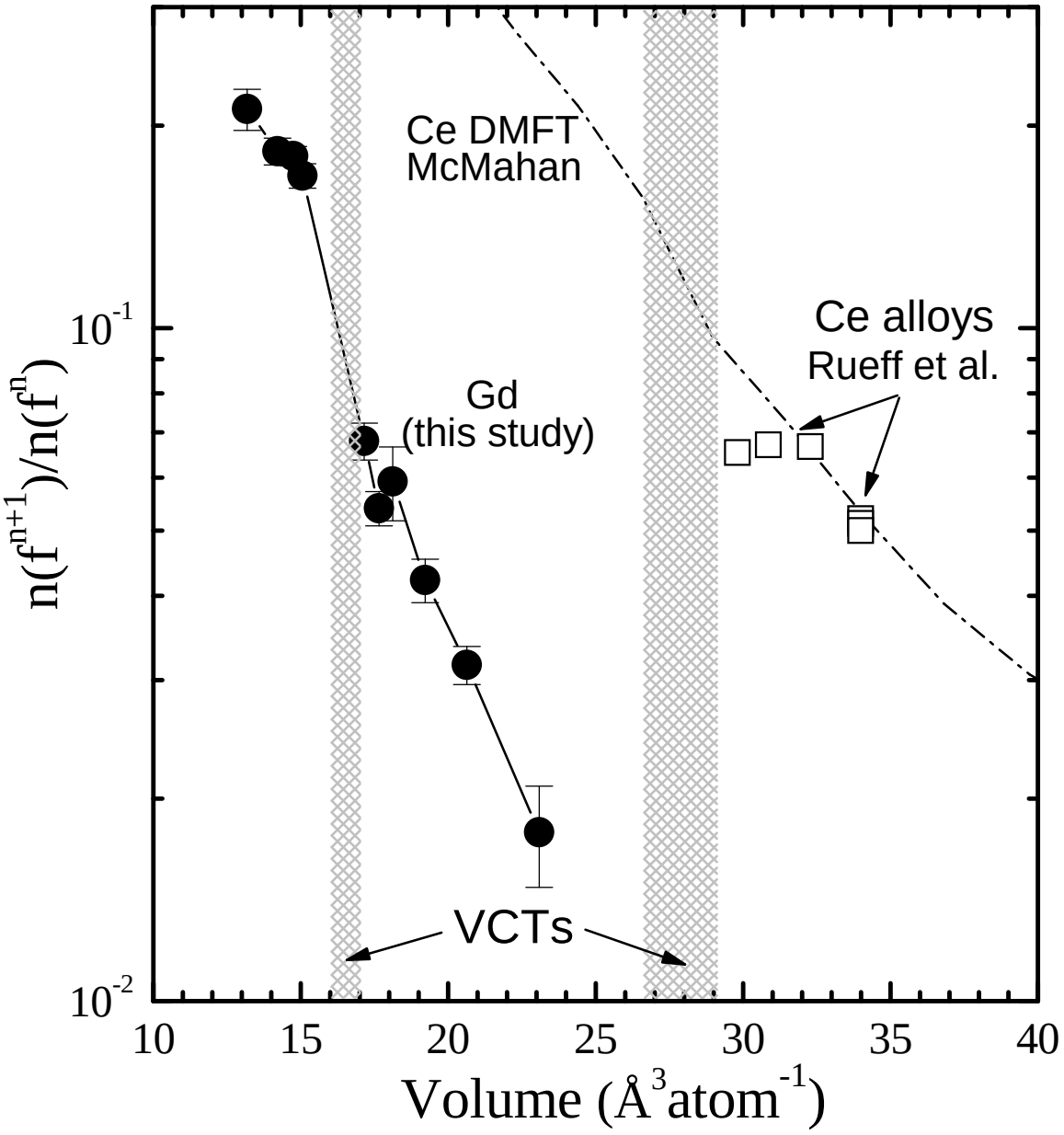

Figure 4.7. The degree of f-electron hybridization, reflected by the ratio $n(f^{n+1})/n(f^n)$, measured by the present RIXS experiments on Gd compared with those previously determined in RIXS experiments on Ce alloys [9] and in recent DMFT calculations [10]. The volume collapse transition (VCT) regions for Gd and Ce are shown as hatched areas.

out for the lowest-energy states of the $4f^7$ shell for each of $J = 1/2$, $3/2$, $5/2$, and $7/2$ [1]. This ratio will be smaller in a real solid due to screening of the intraatomic exchange interactions. However, the essential message is that theory predicts that changes away from the $J = 7/2$, ${}^8S_{7/2}$ Hunds rules ground state should result in significant changes in the XES spectra which are not seen experimentally, consistent with the predictions of Eq. 3.6.

Ce

Cerium is a challenging material to study using $L\gamma_1$ XES due to its single f electron, giving it the lowest $4f$ moment of all rare-earths described here and a low emission energy. The branching ratio between the $L\gamma_1'$ satellite peak and the main $L\gamma_1$ peak, given by Eq. 3.6 (this equations doesn't fully apply to the heavy lanthanides), is the smallest of the rare-earth metals studied in this work [7]. For there reasons, a large sample size and small diameter gasket was used to maximize the collected XES signal, increasing our signal-to-noise (see Sec. 3.4.5). The results are shown in Fig. 4.9 for a number of pressures below and above the 7 kbar volume-collapse transition pressure. The spectrum consists of the main $L\gamma_1$ peak at 6052 eV and the low energy $L\gamma_1'$ satellite peak at 6035 eV, a separation of ~ 17 eV. No changes in the branching ratio were detected to 21 GPa, over 20 times the volume-collapse transition pressure. This result is consistent with our XES results on Gd (see Sec. 4.2.2) and suggests no change in the $4f$ moment up to 21 GPa.

For comparison, we show an XES spectrum taken on CeO_2 at ambient conditions. The Ce^{4+} ions in CeO_2 have an $4f^0$ ground state and should exhibit no net $4f$ moment [81]. The results are shown as the solid red line in Fig. 4.9. Figure 4.9(inset) shows a magnified view of the $L\gamma_1'$ satellite region. This comparison shows that all the Ce metal XES spectra

[1] The $4d \rightarrow 2p$ XES process for an isolated Gd atom was calculated using a fully relativistic, multiconfiguration Dirac-Fock code with the $4f^7$ shell in its lowest energy state for $J = 1/2$, $3/2$, $5/2$, and $7/2$, and taking a $J = 1/2$ $2p$ core hole [79, 80].

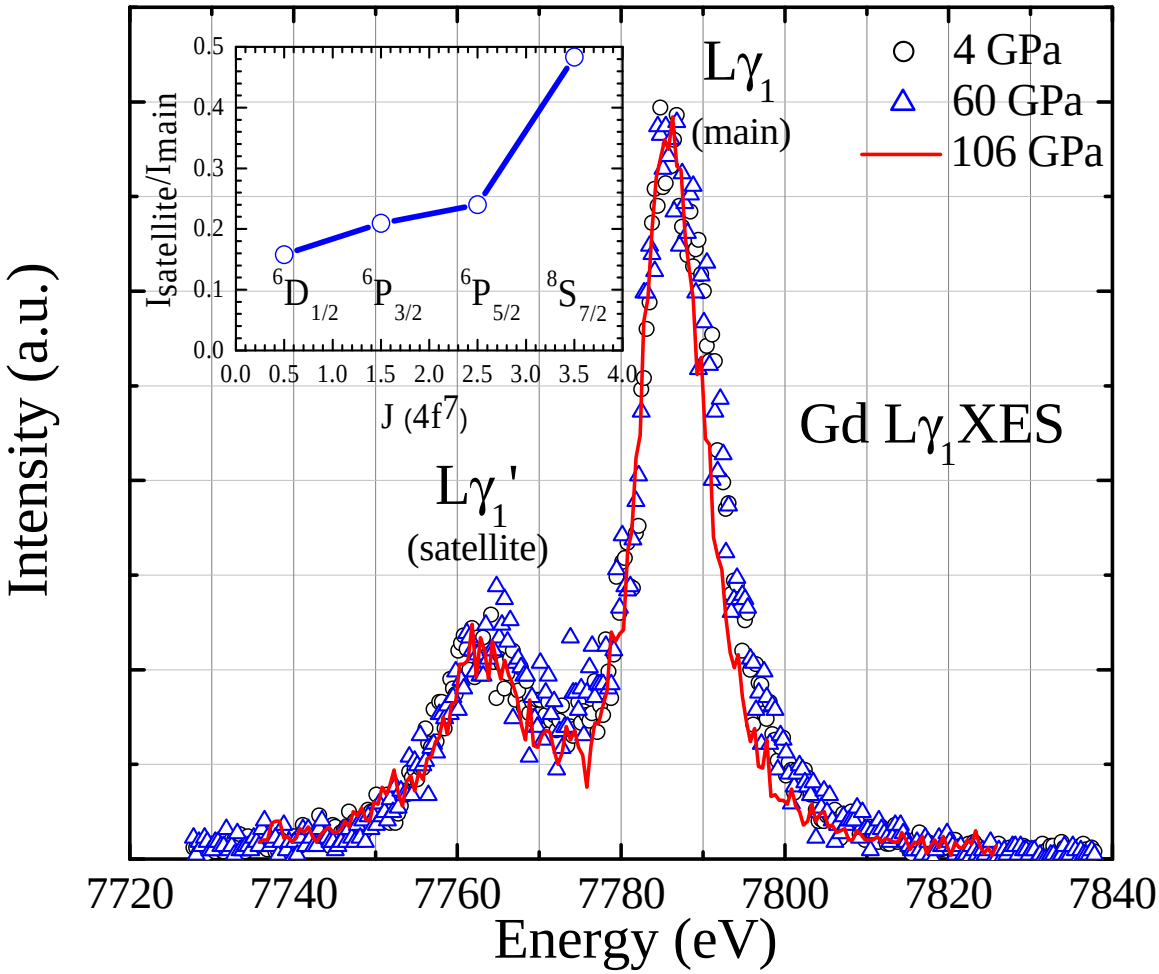

Figure 4.8. $L\gamma_1$ XES spectra of Gd at 4, 60, and 106 GPa, normalized to the main peak intensity, showing no apparent change in the $L\gamma_1'$ satellite peak intensity, suggesting no changes in the $4f$ moments up to 106 GPa. The inset shows $I_{satellite}/I_{main}$ derived from calculated $L\gamma_1$ XES spectra demonstrating that the intensity ratio of the satellite peak to the main peak decreases as you move away from the Hunds rule ground state.

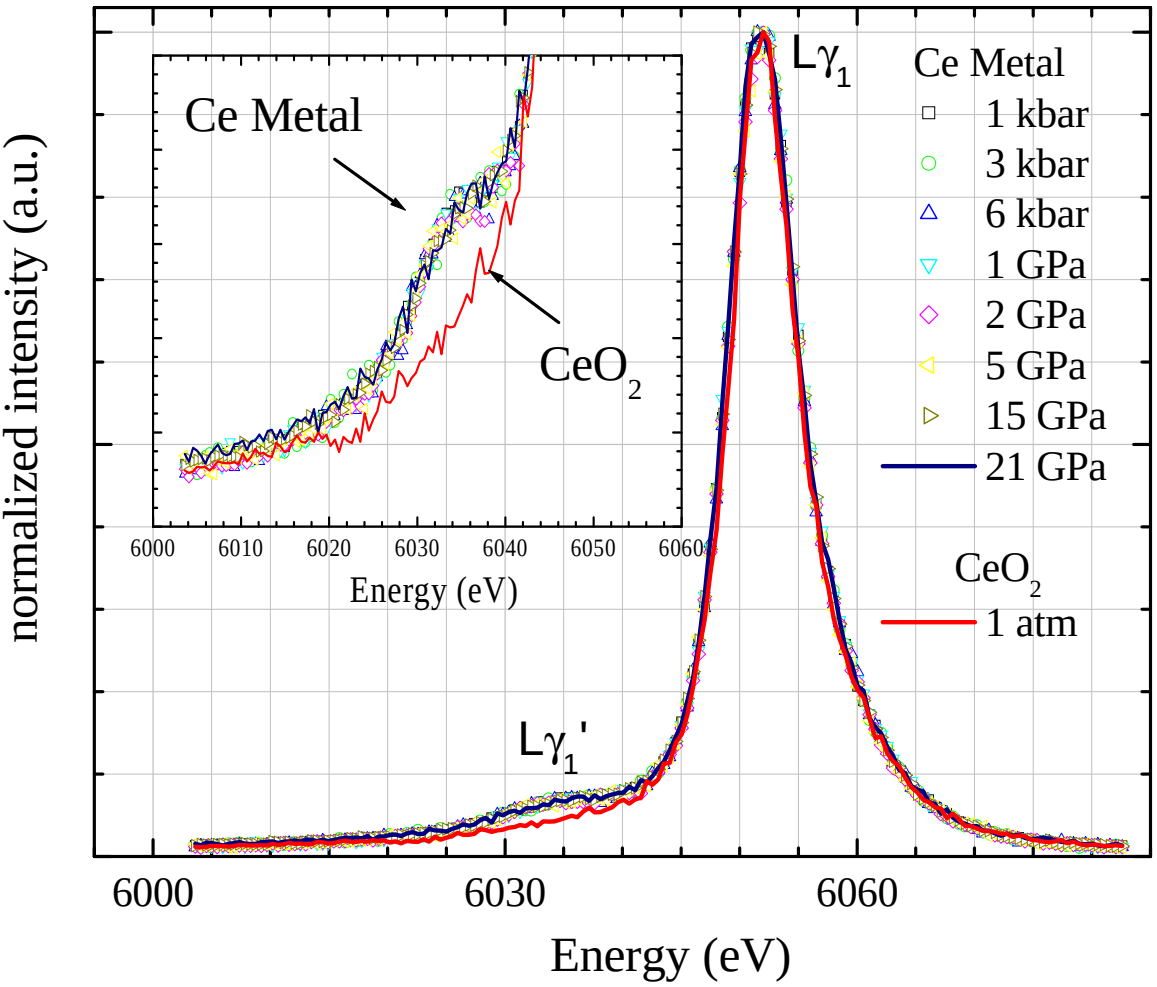

Figure 4.9. $L\gamma_1$ XES spectra of Ce, at a number of pressures, normalized to the main peak intensity showing no apparent change in the $L\gamma_1'$ satellite peak intensity all the way to 21 GPa, the highest pressure reached. Also shown is an XES spectrum taken from tetravalent CeO_2 showing no $L\gamma_1'$ peak intensity. The inset shows an expanded view of the $L\gamma_1$' satellite peak region for Ce metal and for CeO_2. It is clear from the CeO_2 XES spectra that our signal-to-noise is sufficient to detect any changes in the Ce XES.

are essentially the same. However, the CeO_2 spectrum is clearly distinguished from the Ce metal spectra demonstrating that our level of signal-to-noise is more than capable of detecting any changes in I'/I.

Pr

Praseodymium XES was obtained to 42 GPa. To prevent contamination of our signal from impurities in the Be gasket, we loaded Pr using a high purity Be gasket with an amorphous Boron insert to prevent the tails from the focused x-ray beam from clipping the edges of the Be gasket (see Secs. 3.1.2 and 3.1.3). We also used a 50 μm pinhole to remove the long tails of the incident x-ray beam before they reached the sample. Due to time constraints we increased the pressure of the sample to 42 GPa, well above the volume-collapse transition at 25 GPa, the results shown in Fig. 4.10. The spectrum consists of the main $L\gamma_1$ peak, at 6322 eV, and a low energy $L\gamma_1'$ satellite peak at 6303 eV, a separation of 19 eV. No significant changes were detected in the branching ratio between the ambient pressure Pr ingot XES spectrum and the Pr spectrum obtained at 42 GPa. This result is consistent with our XES results on Gd and Ce (see Secs. 4.2.2 and 4.2.2) and suggests no change in the $4f$ moment up to 42 GPa.

Nd

Figure 4.11 shows XES results on Nd up to 85 GPa. At ambient pressure Nd XES consists of the main $L\gamma_1$ line at 6602 eV and a low energy satellite peak, $L\gamma_1'$, at 6581 eV, a separation of 21 eV. No changes in the branching ratio were detected up to 85 GPa, the highest pressure reached in this study. This result is consistent with our XES results on Gd, Ce, and Pr (see Secs. 4.2.2, 4.2.2 and 4.2.2) and suggests no change in the $4f$ moment up to 85 GPa. There was, however, a small increase in linewidth at 85 GPa, seen in Fig.

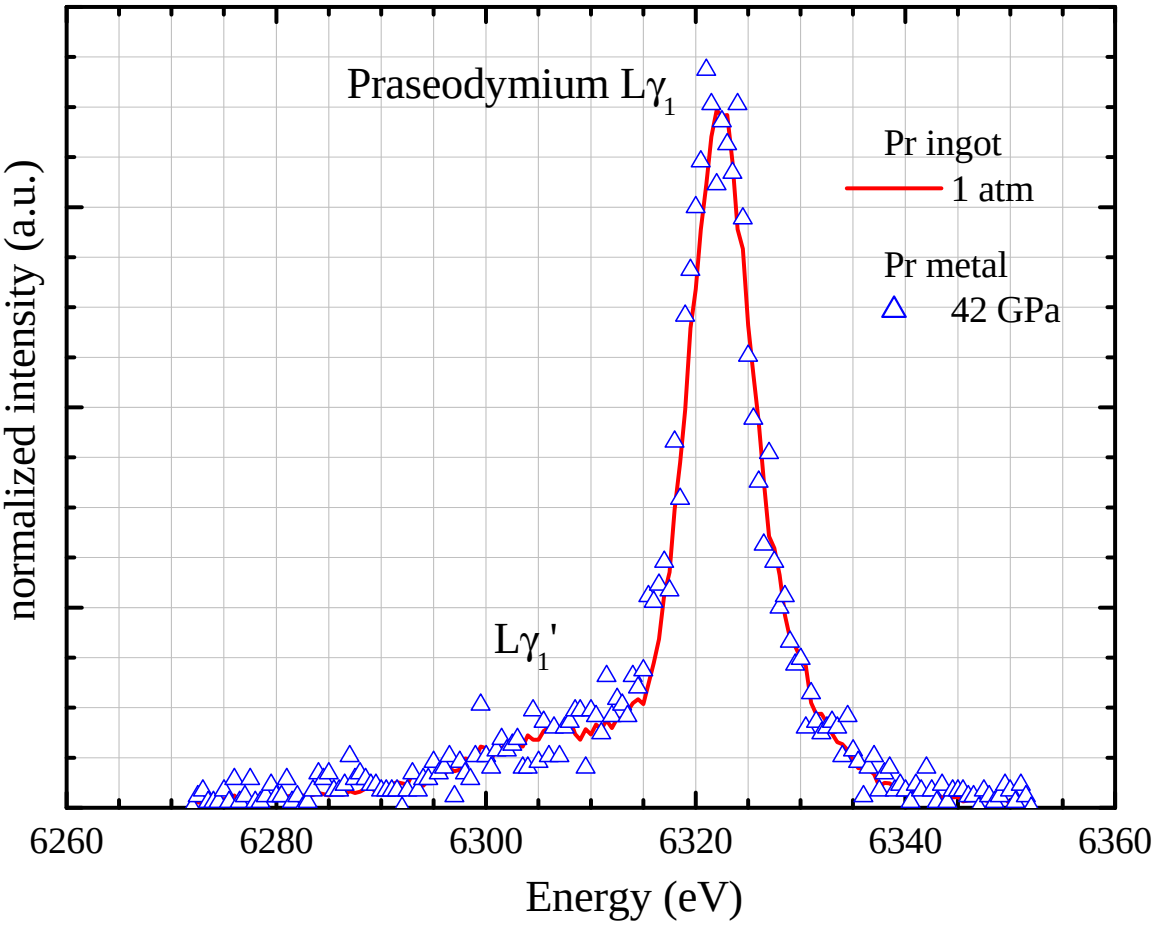

Figure 4.10. $L\gamma_1$ XES spectra of Pr, at ambient pressure (solid line, taken from Pr Ingot) and 42 GPa (open triangles, taken in DAC), normalized to the main peak intensity showing no apparent change in the $L\gamma_1'$ satellite peak intensity.

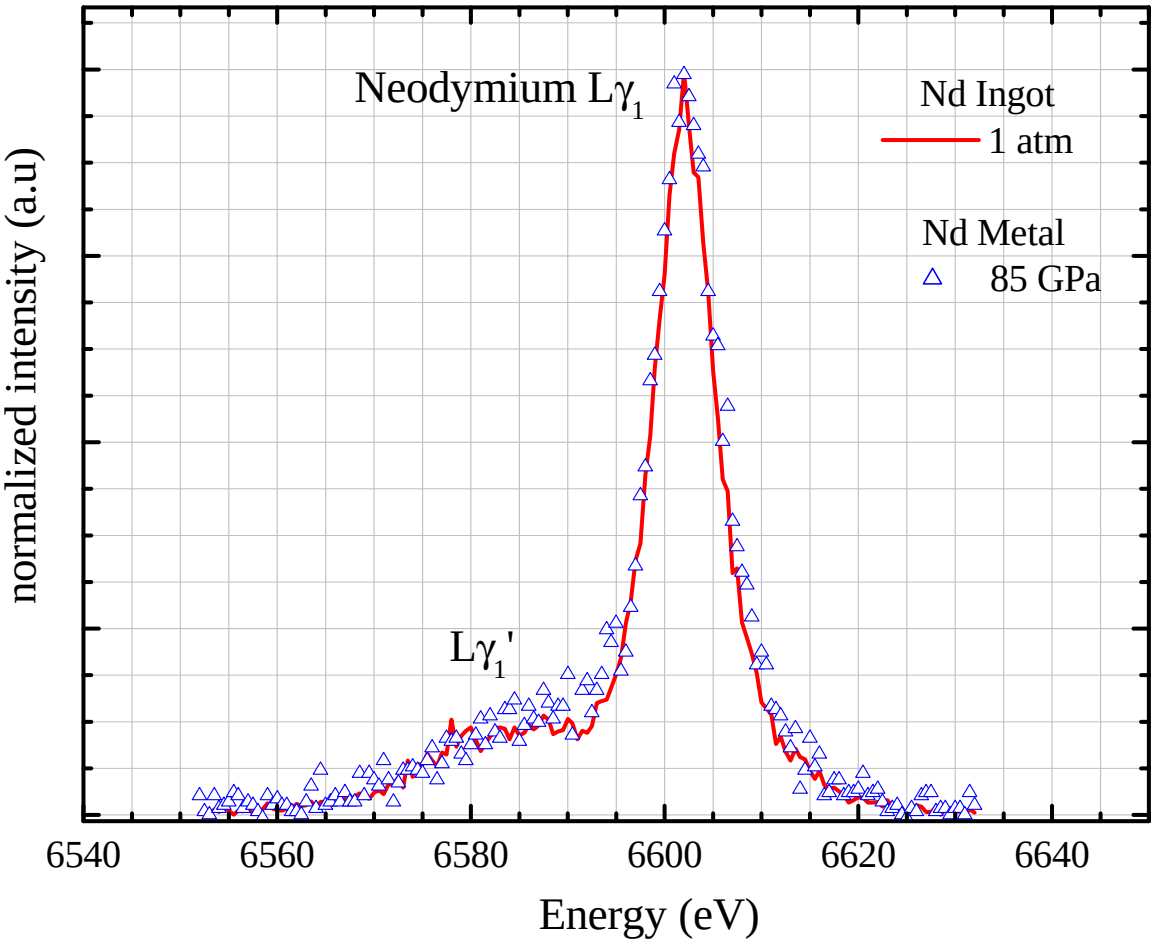

Figure 4.11. $L\gamma_1$ XES spectra of Nd, at ambient pressure (solid red line) and 85 GPa (open blue triangles), normalized to the main peak intensity showing no apparent change in the $L\gamma_1'$ satellite peak intensity.

4.11, most likely due to anisotropic broadening as a result of nonhydrostatic conditions in the sample chamber.

4.3 CrO_2

4.3.1 X-ray diffraction

Figure 4.12(a) shows a Rietveld refinement of α-CrO_2 ($P4_2/mnm$) at 7.7 GPa showing good agreement with the rutile structure with lattice parameters $a = b = 4.3710(1)$

Åand c = 2.8967(1) Å, and $u \sim .294(1)$ (see Sec. 2.2.3 for a description of the rutile structure). At this value of u the CrO_6 octahedra is flattened along apical direction with Cr-O distances of 1.809 Å and 1.928 Å for the apical(2) and equatorial(4) bonds, respectively. By 12.8 GPa an orthorhombic distortion was detected by the splitting of diffraction lines with values of (hkl) such that $h \neq k$, as shown in Fig. 4.12(b). The split $(hkl)'s$ are shown in bold. This is consistent with the structural transition from the rutile to the $CaCl_2$ ($Pnnm$, Z=2) crystal structure observed in other rutile-type oxides such as MnO_2 [82], RuO_2 [83], SiO_2 [84], GeO_2 [85, 86], SnO_2 [87, 88], and PbO_2 [89]. The $CaCl_2$ crystal structure consists of chains of distorted edge-sharing CrO_6 octahedra along the c-axis with the Cr ions forming a body-centered orthorhombic lattice and is shown in Fig. 2.6(c). The position of the oxygen atom is now described by two fractional coordinates u_x and u_y. The Rietveld refinement of β-CrO_2 at 14.0 GPa shown in Fig. 4.12(b) shows good agreement with the $CaCl_2$ structure with lattice parameters a = 4.3874(4) Å, b = 4.2818(4) Å, and c = 2.8779(2) Å, and $u_x = 0.299(1)$ and $u_y = 0.272(1)$.

Figure 4.13 shows lattice constants obtained using a LeBail whole-profile fit as a function of pressure with a dotted vertical line showing the transition pressure. The diffraction data from the mineral oil sample suffered from broadening of diffraction lines above 9 GPa, due to non-hydrostatic conditions inside the sample chamber [90], and made refinement difficult to converge. Therefore, we only present data below 9 GPa for this sample as shown in Fig. 4.13. On the other hand, the diffraction data obtained using liq.-He as a pressure medium stayed well resolved up to the highest pressure obtained. Below the transition pressure the compressibility of the a-axis using mineral oil and liq.-He is very close, with the liq.-He sample showing slightly higher compressibility. The c-axis, however, shows a much lower compressibility when using liq.-He as a pressure medium, although it is clear that both curves extrapolate back to the previously reported value at $P = 0$. A

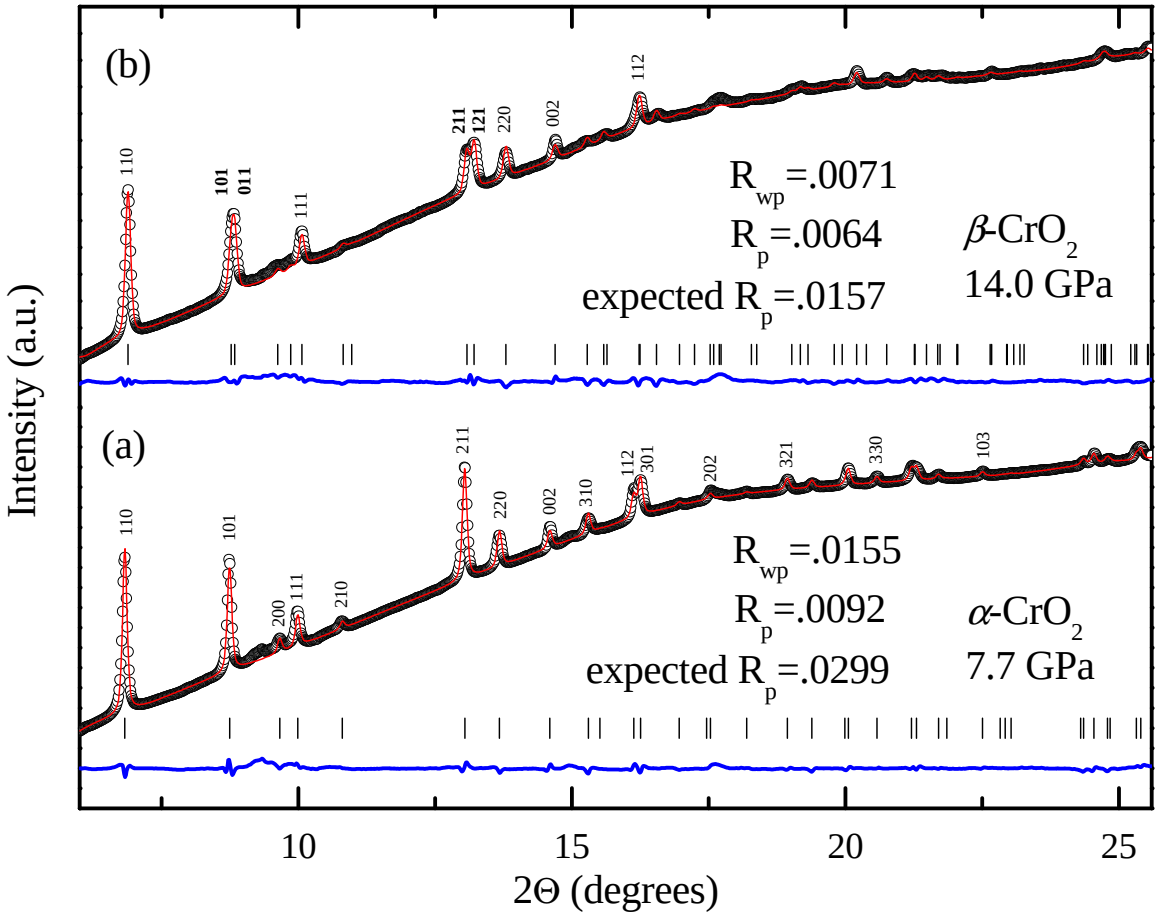

Figure 4.12. The x-ray diffraction pattern of CrO_2 at 7.7 GPa and 14.0 GPa. Open circles show our experimental data while the red and blue traces show the calculated spectra and difference spectra, respectively. Short vertical lines show positions of diffraction lines. (a) shows the structural refinement of rutile α-CrO_2, space group $P4_2/mnm$, while (b) shows the structural refinement of orthorhombic β-CrO_2 in the $CaCl_2$ structure, space group $Pnnm$. The $(hkl)'s$ shown in bold represent those diffraction lines with $h \neq k$ which were split due to the orthorhombic distortion from tetragonal $P4_2/mnm$ to $Pnnm$. The values R_{wp}, R_p, and expected R_{wp} were calculated without contribution from the background fit.

change in compressibility at 12.8 GPa is observed for the c-axis , while the area conserving quantity $\sqrt{ab}$ follows smoothly from the a-axis across the transition. There is also a small but apparent change in compressibility of the c-axis at $\sim$ 25-30 GPa. This change may be a signature of a second phase transition. Additional evidence supporting a second phase transition was observed in our Raman data in this pressure range and is discussed below.

The pressure vs. volume data from the α- and β-CrO_2 phases are plotted up to 50 GPa in Fig. 4.14, identifying the transition pressure $P_c = 12.8 \pm 3$. Below P_c the mineral oil and He data agree well, resulting in a nearly identical P-V curve. Above P_c an anomalous *increase* in the compressibility occurs. This is in contrast to most materials becoming stiffer with increased compression. The experimental P-V curve for α-CrO_2 was fit to the third-order Birch-Murnaghan [91] equation of state

$$P = \frac{3}{2}B_0\left[\left(\frac{V}{V_0}\right)^{-7/3} - \left(\frac{V}{V_0}\right)^{-5/3}\right]\left\{1 + \frac{3}{4}\left(B_0' - 4\right) \times \left[\left(\frac{V}{V_0}\right)^{-2/3} - 1\right]\right\} \qquad (4.2)$$

with $B_0' = (dB/dP)_{T;P=0} = 4$ and V_0 fixed at the previously reported value of 56.99 Å[11] which yielded a value of $B_0 = 239 \pm 2$ GPa for the zero-pressure bulk modulus. The high-pressure β-CrO_2 phase was also fit to Eq. 4.2 yielding values of $B_0 = 162 \pm 2$ GPa and $V_0 = 58.1 \pm 0.1$ $Å_3$ for the zero-pressure bulk modulus and unit cell volume, respectively. We also performed Birch-Murnaghan equation of state fits for both phases while letting B_0' vary. In addition, fits to the Vinet equation of state, a more recent EOS based on the Rydberg potential and believed to better model materials under very high compressions, were performed [92]. These are shown in Fig. 4.14 and the numerical results of the various fits are summarized in Table 4.3.1. The fits to the low-pressure phase all give quite similar answers; however, the differences between the various equations of state fits are evident in the high pressure phase. This is primarily due to the lack of data to constrain V_0 as β-CrO_2 does not exist at ambient conditions. It is clear, however, that a pronounced softening is

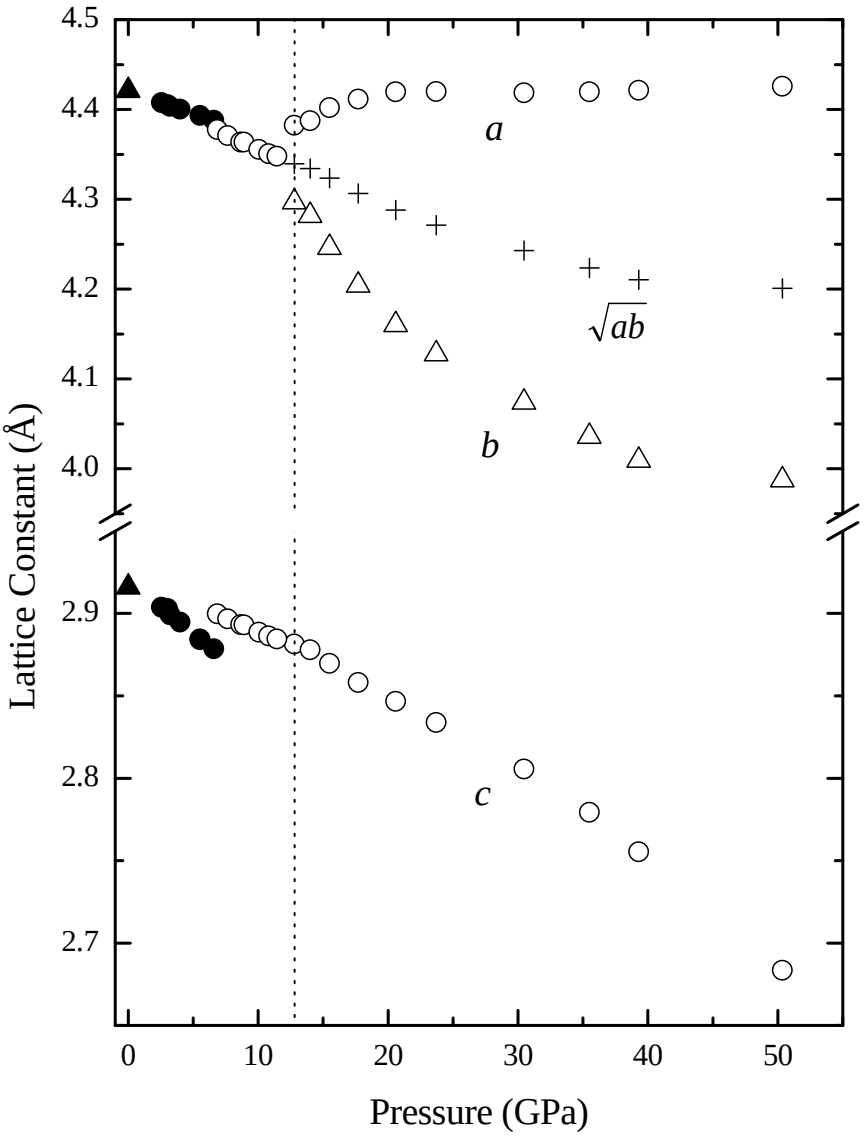

Figure 4.13. Lattice Constants of CrO_2 as a function of pressure. Open and closed circles represent data taken with Helium and mineral oil as pressure media, respectively. Dark triangles are data obtained by Cloud *et al.* [11]. Crosses represent the area conserving quantity $\sqrt{ab}$. Vertical dotted line at 12 GPa shows transition pressure from rutile α-CrO_2 to orthorhombic β-CrO_2.

	Birch-Murnaghan			Vinet		
Phase	B_0 (GPa)	B_0'	V_0 (Å^3)	B_0 (GPa)	B_0'	V_0 (Å^3)
I	239 ± 2	4.0	56.99	242 ± 2	4.0	56.99
I	235 ± 10	5 ± 2	56.99	235 ± 10	6 ± 2	56.99
II	162 ± 2	4.0	58.1 ± 0.1	181 ± 3	4.0	57.8 ± 0.1
II	143 ± 16	4.8 ± 0.7	58.5 ± 0.4	138 ± 16	5.8 ± 0.7	58.6 ± 0.4

Table 4.1. Summary of numerical results from various equation of state fits to our experimental P-V data. Numbers shown without error denote values that were fixed during the fitting procedure.

evident irrespective of the model used to fit the compression data.

4.3.2 Raman Spectroscopy

The Raman signal of half-metallic CrO_2 is very weak due to the metallic nature of the material which, due to a short penetration depth, results in a relatively small scattering volume and low number of scattering sites [12]. Nevertheless, by using a fast con-focal Raman spectroscopy system we were able to obtain relatively high quality Raman spectra from powdered CrO_2 using no more than 30 mW of laser power as measured at the sample (see Sec. 3.3.2). Small features in the Raman spectra below 200 cm^{-1} are, however, obscured because of the use of two holographic notch filters used to prevent Rayleigh scattered light from entering the spectrometer, the result of which was both the introduction of some small spurious peaks and much reduced transmission below 200 cm^{-1}.

A factor group analysis gives four Raman-active modes in the rutile structure, $\Gamma_{Raman} = E_g + A_{1g} + B_{1g} + B_{2g}$ (see. Sec. 3.3.1). Previous work by Iliev *et. al.* [12] using polarized Raman spectroscopy on single-crystal CrO_2 at ambient pressure describes these modes and determined the Raman-shifts to be 149 cm^{-1}, 458 cm^{-1}, 570 cm^{-1}, and 682 cm^{-1} for the B_{1g}, E_g, A_{1g}, and B_{2g} modes, respectively. Figure 4.15 shows the Raman spectra of CrO_2 taken at various pressures. The three peaks at 470 cm^{-1}, 584 cm^{-1} , and

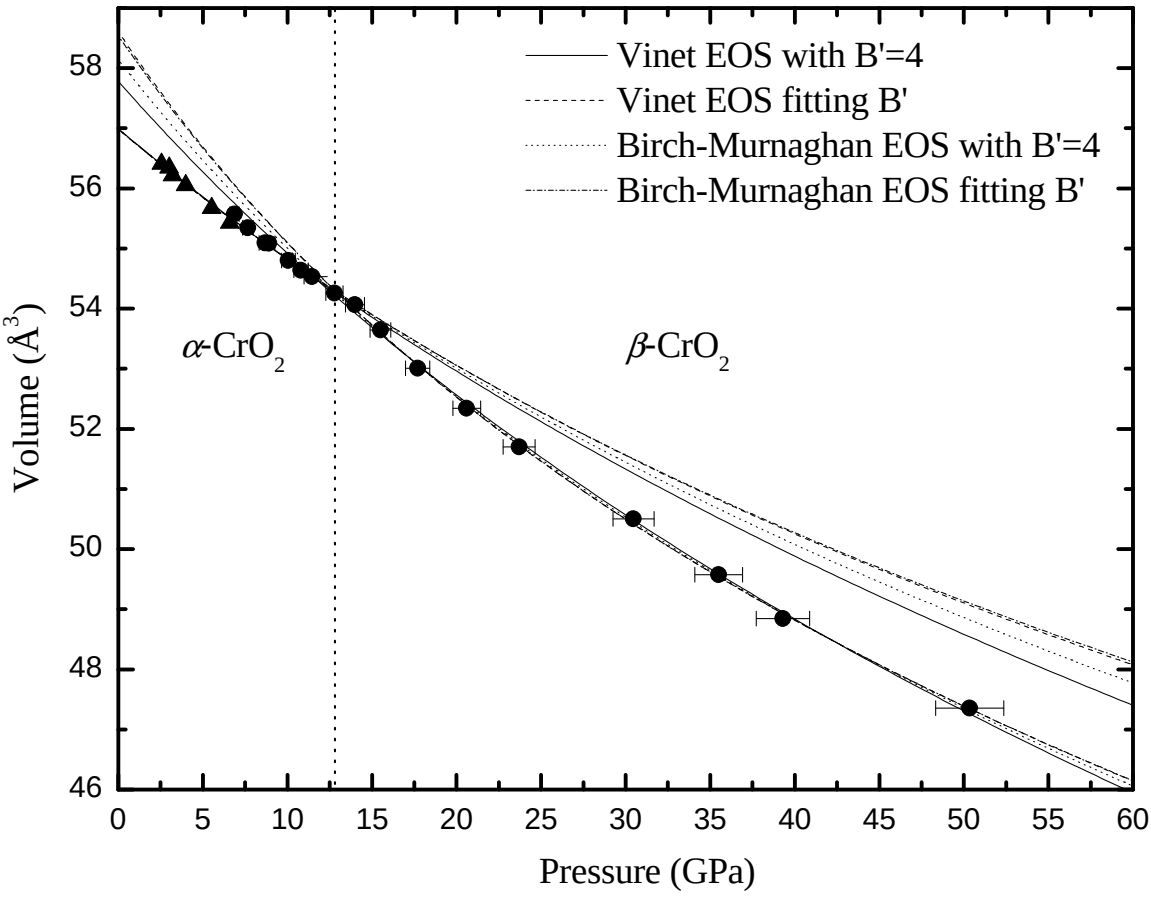

Figure 4.14. Pressure vs volume data for CrO_2. Dark circles and triangles are data taken with He and mineral as the pressure medium, respectively. Dotted vertical line denotes transition from rutile α-CrO_2 to orthorhombic β-CrO_2 at 12 ± 3 GPa. Error bars are shown when uncertainties exceed symbol width. Various fits are shown using the Birch-Murnaghan and Vinet equations of state, both with and without fixing $B_0' = 4$. The numerical results are summarized in Table 4.3.1.

700 cm^{-1} shown at 2.8 GPa are associated with the E_g, A_{1g}, and B_{2g} modes of the rutile structure. Unfortunately, we were not able to observe the Raman-active B_{1g} shear mode, which has been shown to exhibit soft-mode behavior at high pressure in other rutile-$CaCl_2$ [84, 88] transitions, due to its very weak scattering around 150 cm^{-1}.[83]

The expected mode behavior for a phase transition from rutile to $CaCl_2$ is a splitting of the doubly degenerate E_g mode along with the addition of a new Raman active mode of B_{1g} symmetry [83]. At 12.4 GPa a new peak appears at 470 cm^{-1} and the E_g mode begins to broaden. By 19.5 GPa a clear splitting of the E_g mode is observed along with an additional peak emerging at 162 cm^{-1}. Mode assignments for phase II are based primarily on the correlation between rutile (D_{4h}) and $CaCl_2$ (D_{2h}) modes except for the new Raman-active mode of B_{1g} symmetry which is tentatively assigned to the new peak at 470 cm^{-1} and assumed to be accidentally degenerate. The order of the B_{2g} and B_{3g} modes shown is arbitrary as it has been argued that the sign of the spontaneous strain, $e_{ss} = (a - b)/(a + b)$ where a and b are lattice constants, determines the ordering [93]. Because all our experiments were done on powdered samples and not single crystals, the sign of e_{ss} is unknown. It should also be noted that a seventh, unassigned peak was observed at 33 GPa, identified with an asterisk, showing a variation with pressure consistent with the other, identified peaks. The small peak around 185 cm^{-1} at 41.1 GPa, marked with a cross in Fig. 4.15, was intermittent and did not seem to show any consistent behavior with pressure. This peak is therefore attributed to spurious noise caused by the pair of holographic notch filters coupled with the background subtraction procedure.

Figure 4.16 shows the pressure-induced shifts of the observed Raman modes for α- and β-CrO_2. Although we were unable to directly observe any mode-softening behavior due to the weakness of the B_{1g} shear mode in rutile α-CrO2, we can speculate that in order for the B_{1g} mode to smoothly connect to the A_g mode there must have been some softening.

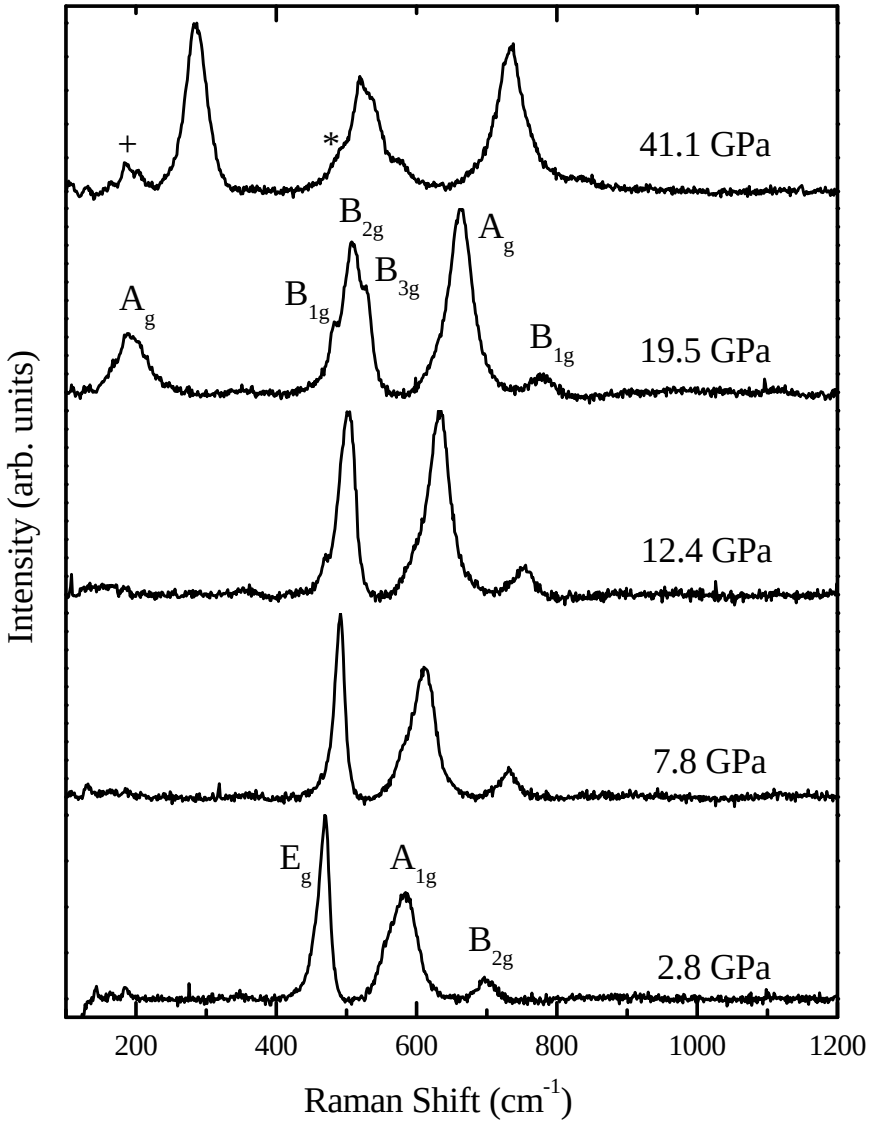

Figure 4.15. Raman spectra of CrO_2 at 532 nm excitation at various pressures. At 12.4 GPa the broadening of the E_g mode due to a splitting and the appearance of a new mode at 470 cm^{-1} are consistent with a phase transition from rutile to $CaCl_2$ structures. We also see the appearance of the Raman active A_g mode in $CaCl_2$ as shown at 19.5 GPa. The asterisk marks an unidentified peak occurring at 32 GPa and persisting up to the highest pressure obtained during this experiment. A broad background has been subtracted from all spectra. The cross marks an intermittent peak caused by a combination of the holographic notch filters and the background subtraction and does not shift consistently with pressure.

Figure 4.16 shows ambient pressure values obtained from Iliev *et al.* [12] for all four Raman active modes in rutile CrO_2 as dark triangles. A smooth curve can be drawn between the ambient pressure values and our data for the E_g, A_{1g}, and B_{2g} modes, however not for the B_{1g} mode. This is further evidence that β-CrO_2 takes the $CaCl_2$ structure; softening of the B_{1g} mode has been seen in many of the rutile-$CaCl_2$ transitions [84, 88, 85]. It should again be noted that the unidentified peak showing up at 33 GPa, marked with an asterisk in Fig. 4.16, shows a pressure-induced shift consistent with the rest of the identified modes.

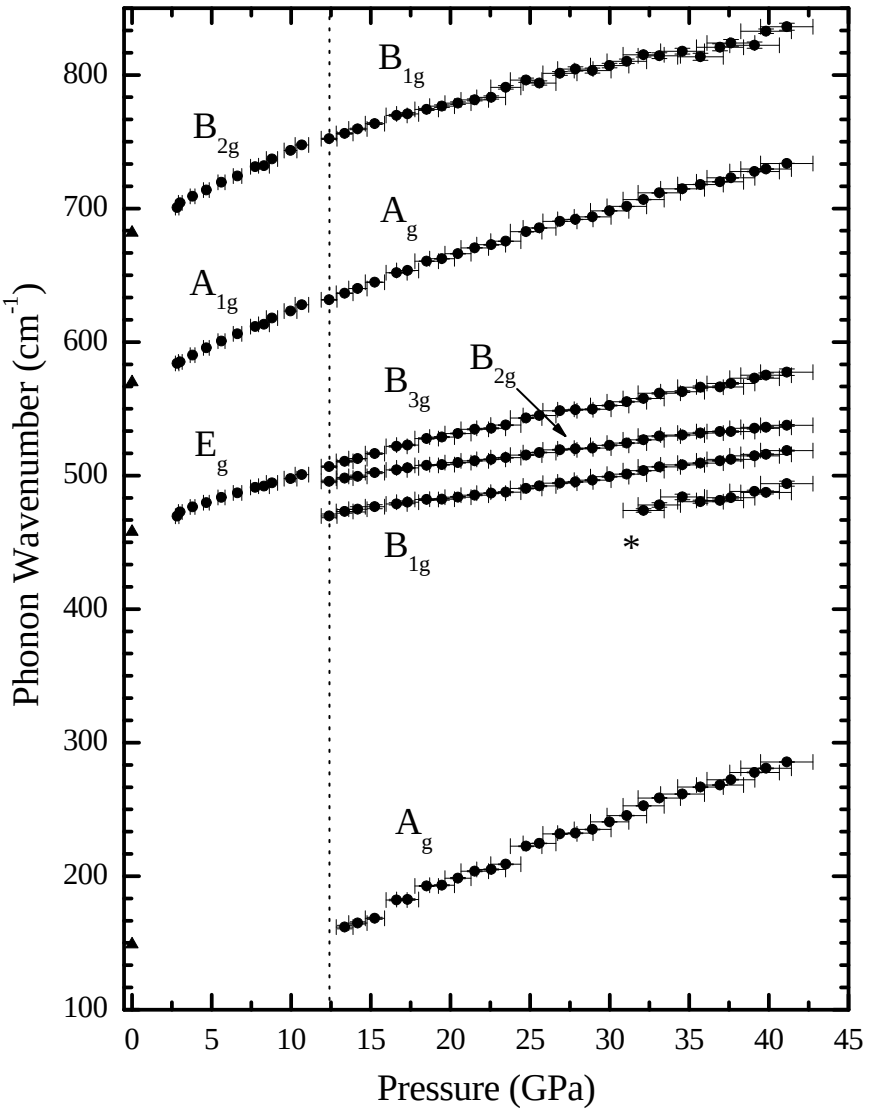

Figure 4.16. Plot of CrO_2 phonons vs. pressure in the rutile and $CaCl_2$ structures. Dark triangles show ambient pressure values obtained by Iliev et.al.[12] on single crystal CrO_2. Dark circles represent our data. Dotted vertical line at 12 GPa denotes the transition from tetragonal α-CrO_2 to orthorhombic β-CrO_2 derived from our experimental data.

Chapter 5

Discussion

5.1 MnO

5.1.1 Metallization Pressure Revisited

Patterson *et al.* [5] places the MnO metallization pressure at 90 GPa, at the start of the intermediate phase region, based on resistivity measurements. However, it was unclear whether metallization occurred due to a change in electron correlation or due to a simple change in crystal structure that resulted in a reordering of the electronic bands due to a change in the crystal field. A re-analysis of their data, shown in Fig. 5.1, indicates that the transition pressure should be placed closer 103 GPa. A smooth curve can be drawn through their resistance data all the way to 103 GPa, where a three order-of-magnitude drop is seen. The large, continuous drop starting from ambient pressure all the way to 103 GPa is then the result of pressure-induced band broadening.

Visual observations of our sample at each pressure point during the XES experiment provide further confirmation that the metallization does indeed occur closer to 108 GPa, and not the start of the 2-phase region at 90 GPa. Figure 5.2 shows MnO at three

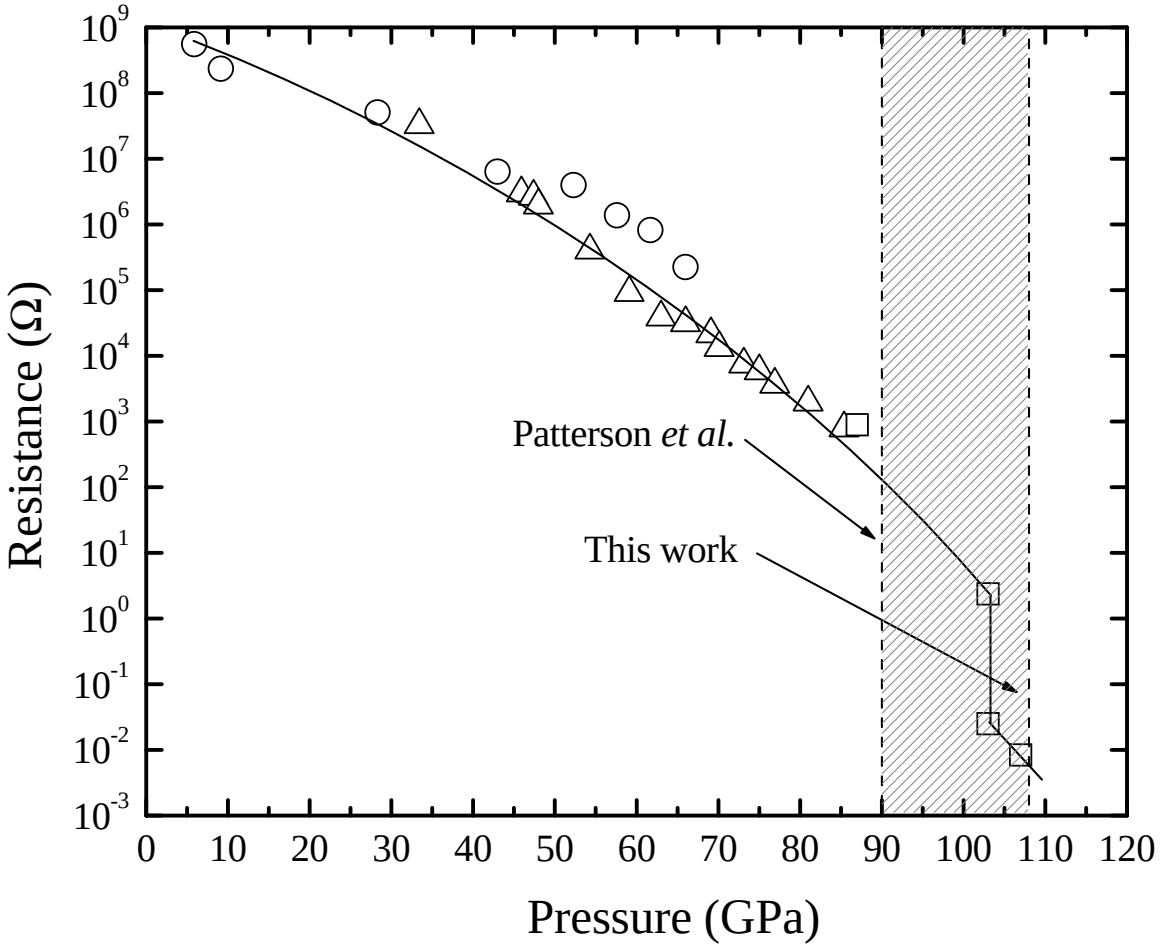

Figure 5.1. A replotting of the resistivity data on MnO from Patterson *et al.* (Ref. [5]). The leftmost dashed line shows the metallization pressure quoted by Ref. [5]. The rightmost dashed line shows the Mott transition pressure derived from our XES results. It is clear that an abrupt drop in resistivity is seen above 90 GPa, close to the 108 GPa pressure set by our XES measurements.

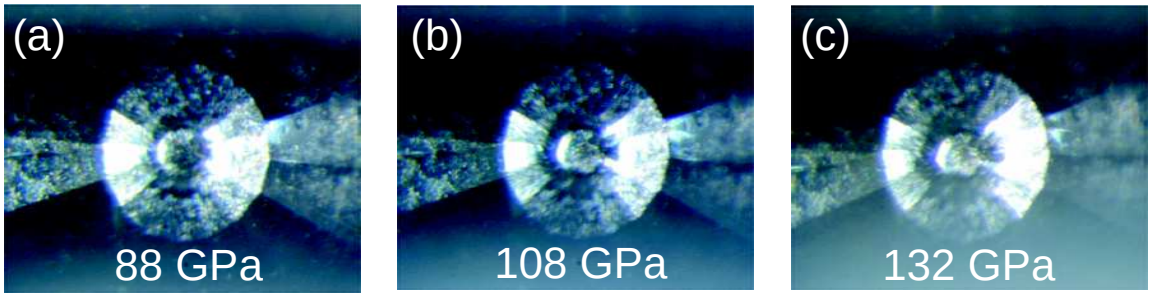

Figure 5.2. Visual observations taken under a microscope showing changes in the reflectivity of MnO across the Mott transition. The sample is slightly offset down and to the right from the center of the culet. (a) shows MnO at 88 GPa and illustrates the dark color of the sample. (b) shows the sample right at the 108 GPa. (c) shows the sample well above the Mott transition illustrating its highly reflective nature, indicative of metallic behavior.

different pressures around the vicinity of the Mott transition. At 88 GPa (Fig. 5.2(a)) MnO is still dark, showing little reflectivity. No changes were observed at the 98 GPa pressure point (not shown). However, at 108 GPa (Fig. 5.2(b)) the sample abruptly changes color and adopts a metallic luster. By 132 GPa (Fig. 5.2(c)) the entire sample is highly reflective, indicative of metallic behavior. The partial luster seen at 108 GPa is due to the pressure gradients present at such high pressures, even in the presence of a pressure-transmitting medium. However, this gradient was estimated to be only ~ 3 GPa at 100 GPa by measuring Ruby fluorescence at different points inside the sample chamber.

5.1.2 Interpretation of Intermediate Phase Region

Kondo *et al.* concluded that the transition to the $B8$ structure in MnO occurred at 120 GPa, directly following the unknown intermediate phase between 90 GPa and 120 GPa. This allows the possibility that the metallization at 108 GPa is due to a change in structure. However, our x-ray diffraction results indicate that the intermediate phase region is really a mixture of the lower pressure $dB1$ structure and the $B8$ structure, with the $B8$ structure actually appearing at 90 GPa. At 110 GPa, an isostructural volume-collapse

transition occurs in the $B8$ phase which coincides with the loss of magnetic moment from XES measurements and the metallization. These results rule out metallization due to a change in crystal structure.

There is a precedent for such mixed phase behavior and superlattice formations in displacive transitions [94], most notably during correlation-driven phase transitions in the Mott insulators Fe_2O_3 [95] and FeI_2 [96]. Theoretical investigations of the Mott insulator FeO [97] also show such behavior. Note first that there is only a small difference between $dB1$ and $B8$ structures: the $dB1$ is a six-layer A(O)c'(Mn)B(O)a'(Mn)C(O)b'(Mn) structure, whereas $B8$ is a four-layer structure with the sequence a(Mn)B(O)a(Mn)C(O). Therefore, the $dB1$ to $B8$ transition requires only a small displacement of oxygen atoms from distorted octahedral sites with three quasi-nearest Mn-O distances, 1.70, 2.17, and 2:24 Å to perfect trigonal prism sites with all equal Mn-O distance, 2.04 Å. Such a displacive transition between two energetically similar structures often results in relatively large hysteresis in pressure and thus in two phases which coexist over an extended pressure range.

5.1.3 Collapse of the local moment and The Mott Transition

Our high pressure XES results indicate a collapse of the $3d$ magnetic moment at 108 GPa and a metallization occurring at around $\sim$ 103 GPa. Since the pressure gradients in our samples were $\sim$ 3 GPa at 1 MBar, these phenomenon occur sufficiently close in pressure to be considered happening concurrently. We therefore place the transition pressure at 105 ± 5 GPa. These results strongly support a Mott transition scenario in which pressure drives the delocalization of the $3d$ band by reducing the inter-atomic distances, thus increasing the bandwidth W in relation to the intra-atomic coulomb interaction U. As the bandwidth increases, the Hubbard gap decreases, eventually resulting in the overlap between the UHB and LHB and prompting a transition to the metallic state. This metallic state also destroys

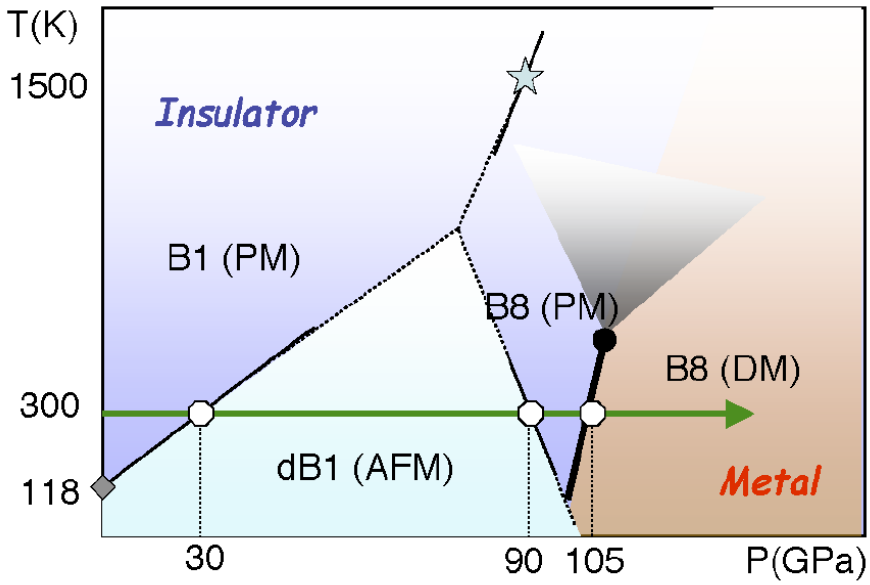

Figure 5.3. Our proposed phase diagram of MnO constructed from our experimental data, with insights from the magnetic and structural phase diagrams of FeO [13, 14].

the local 3*d* moment since the same electron correlations that produce the insulating state are responsible for the formation of moments. This picture is supported by the continuous decrease in resistance leading up to the metallization, shown in Fig. 5.1.

We can now form a coherent picture of the high pressure behavior of MnO and the Mott transition at 108 GPa. Figure 5.3 shows the phase diagram of MnO deduced from our results, coupled with resistance data [5] and insight from the magnetic and structural phase diagram of FeO [13, 14]. The PM to AFM and AFM to PM transitions are shown at 30 GPa and 90 GPa. Above 90 GPa and 300K, MnO is PM and strongly 2-phase. At 108 GPa, a complete loss of 3*d* magnetic moment is detected, coinciding with an abrupt drop in resistance [5]. In addition, an isostructural volume-collapse within the *B*8 phase is detected. All of these are a manifestation of the same phenomenon, the Mott transition.

5.1.4 Implications to other Correlated Materials

A large change in volume, between 5-7%, was also predicted for the transition metal monoxides across the magnetic collapse [98]. In MnO we see the metallization and magnetic collapse occur abruptly with no structural changes, rather an isostructural volume-collapse transition within the $B8$ phase. The measured volume change for MnO is $\sim 4.5\%$, consistent with these predictions. However, according to Ref. [98], the magnetic collapse is first-order only during a $dB1 \rightarrow inverse-B8$ transition and is second order for a $dB1 \rightarrow normal-B8$ transition. These two structures differ only in the placement of the metal ions. Our results are in disagreement with this conclusion, suggesting instead that a first-order collapse can occur across the $dB1 \rightarrow normal - B8$ transition.

Similarities between the electron correlation driven transitions in the $3d$ monoxides and the $4f$- and $5f$-electron metals were predicted over 20 years by Johansson [99]. He postulated that the γ-α transition in Ce was actually a Mott transition based on the bonding properties of the post-collapse structures [20]. This transition is also accompanied by a rapid decrease in resistance coupled along with changes in the magnetic susceptibility from Curie-Weiss behavior to an expected temperature-independent Pauli-like paramagnetism, suggesting loss of the moments [3, 38]. However, our XES results indicate the volume-collapse phenomenon in the lanthanides does not fit a Mott transition model. This is discussed in Sec. 5.2.2.

5.2 Rare-earth metals

5.2.1 f-electron Delocalization in Gd

The results of $2p3d$ RIXS on Gd metal at high pressure reveal that the delocalization (hybridization) of the $4f$ electrons occurs smoothly and continuously, over an extended

range of volumes. This continuous transition is in contrast to the abrupt metallization and moment collapse seen in the Mott insulator MnO (see Sec. 5.1.3). Calculations by McMahan [10] using DMFT + LDA on Ce also describe a prolonged transition characterized by the appearance and increase of the Kondo resonance at the Fermi level, a hallmark of the Kondo volume-collapse model. It was shown that in Ce, a marked increase in this resonance was seen to occur over the volume range associated with the collapse transition, in agreement with a Kondo volume-collapse scenerio where the transition is driven by an increase in the Kondo temperature.

It is also evident from Fig. 4.7 that the f-occupancy ratio $n(f^{n+1})/n(f^n)$ for Gd ($n = 7$) is much lower at a given volume than that of Ce ($n = 1$). One would expect Gd to be more localized and thus have a smaller $n(f^{n+1})/n(f^n)$ ratio than Ce at the same volume since the f shell is more tightly bound in the heavier lanthanides due to the ever increasing, but incompletely screened nuclear charge. More important is the half-filled shell in Gd with total $4f$ spin $S = 7/2$ and the associated large impact of the intraatomic exchange. This is reflected in an energy splitting of $\sim$ 12 eV (an effective Hubbard U) between lower and upper Hubbard bands in Gd as compared to $\sim$ 6 eV in Ce [100], which should make Gd significantly more localized. It is also interesting to note that the volume collapse transitions (shaded regions) also occur in roughly the same range of $n(f^{n+1})/n(f^n)$ as measured by RIXS in both Gd and Ce.

5.2.2 Behavior of $4f$ moment during VCT: Kondo vs. Mott

There has been much debate whether the VCT and $4f$ delocalization phenomenon in the rare-earths was a Mott transition, similar to that observed in MnO (see Sec. 5.1.3. The previous section (Sec. 5.2.1) on the delocalization of $4f$-electron in Gd seen using RIXS describes a prolonged, continuous process inconsistent with the abrupt delocalization

predicted for a Mott transition. However, another characteristic of the Mott transition is the magnetic collapse that is observed concurrent with the delocalization. Measurements of magnetic susceptibility in α-Ce and early actinide analogs have led to the expectation of a temperature-independent magnetic susceptibility in the collapsed phases of the f-electron metals, suggesting the absence of moments [3, 38]. This result has led many theorists to believe that the γ-α transition in Ce is indeed a Mott transition. Yet the single-ion magnetic response seen in high-energy neutron scattering measurements for α-Ce is consistent with a still extant $4f$ moment [39].

The XES results presented in Secs. 4.2.2, 4.2.2, and 4.2.2 on Gd, Ce, and Pr show no changes in the $L\gamma_1$ emission spectrum of these materials to very high pressure, well past their respective volume-collapse transitions. More specifically, there is no change in the relative intensity between the main $L\gamma_1$ peak and the $L\gamma_1'$ satellite peak. Since the intensity ratio is linked to the $4f$ moment, similar to the $K\beta$ emission reflecting the $3d$ moment in the transition metals, we conclude there is no change in the $4f$ moment in the rare-earth metals across their volume-collapse transitions. This result is in agreement with high-energy neutron scattering on α-Ce but is in seemingly disagreement with magnetic susceptibility measurements.

This dilemma is resolved by the Kondo volume-collapse perspective in which the delocalization is driven by increased hybridization. This hybridization is characterized by the ratio $|J|/D$, where J is the Kondo exchange interaction and D is the half-width of the conduction band. This is analogous with the ratio U/W in the Hubbard model except the the Kondo J described an interaction between the highly localized $4f$ electrons and the conduction band. Similar to the Hubbard model, pressure changes the ratio $|J|/D$ and drives the system to a regime of very high Kondo temperature ($T_K \sim 6000$). It was shown that well below T_K, the localized $4f$ moment is screened completely by the conduction

electrons [101]. The loss of magnetism seen in susceptibility measurements in Ce is then explained by a very high Kondo temperature in the collapsed phase, i.e. susceptibility measures a $4f$ moment largely screened away by the valence electrons [102, 21].

The Kondo volume-collapse perspective can also explain the apparent dilemma between magnetic susceptibility measurements of Ce and experiments such as high-energy neutron scattering on Ce and our XES results. The primarily atomic XES process reflects exchange interactions between $4f$ and core-hole orbitals whose radial distributions lie much closer to the nucleus than the valence orbitals. Because the screening occurs in the outer, valence orbitals, it seems intuitive that the XES process in the rare-earths measures a bare $4f$ moment. This same argument applies to high-energy neutron scattering in which the neutrons interact not with the electron density, as in x-ray diffraction, but with the positive nuclear core which should also see an unscreened, bare moment.

Neodymium reaches the itinerant state smoothly, without an abrupt VCT. Despite this important difference, our high pressure XES results show that the $4f$ moment in the rare-earths behaves the same regardless of whether there is a large volume-collapse at high pressure or not. It was long thought that the volume collapse was an integral part of the delocalization process. This is most evident in Ce where the volume-collapse is isostructural. However, all other rare-earths undergoing a volume-collapse do so along with a structural change. Our results on the $4f$ delocalization of Gd using RIXS show that the delocalization happens continuously with volume, *i.e.*, the volume-collapse only serves to speed up the delocalization process and does not drive it. This conclusion is supported by Nd, whose $4f$ moment behaves the same as those rare-earth metals who do undergo volume-collapse transitions.

5.3 CrO_2

The present x-ray data reveal that the rutile-to-$CaCl_2$ transition in CrO_2 is a strain-driven, 2nd-order distortive phase transition. The crystal structures of both phases (see Fig. 2.6) consist of distorted edge-sharing CrO_6 octahedra where the degree of distortion increases as you move from α-CrO_2 to β-CrO_2. For example, at ambient conditions the four equatorial Cr-O bonds in the [110] plane are at 1.917 Å and lie roughly along the c-axis while the other two apical Cr-O bonds in the [1-10] plane are at 1.882 Å and lie parallel to the ab-plane. At the onset of the transition at 12.4 ± 3 GPa the disparity in Cr-O distances increases to 1.930 Å for the equatorial bond and 1.795 Å for the apical bond. This local strain arising from the large disparity in bond lengths along the c-axis and ab-plane results in a large compressibility along the c-axis with respect to the a- and b-axes (see Fig. 4.13) and an increase of the O-O contact distance to 2.568 Å for β-CrO_2 from the relatively short 2.488 Å in α-CrO_2. This short O-O distance in α-CrO_2 may induce the softening of the B_{1g} mode inferred from the present Raman data, shown in Fig. 4.16, and cause a mechanical instability of the rutile structure [103, 104].

5.3.1 Second-Order Phase Transitions

It is often difficult to correctly determine the order of a phase transition through structural measurements alone. Recall that the splitting of the (101) diffraction peak into (101) and (011) peaks is seen clearly at 12.8 GPa. However, broadening of the (101) peak before 12.8 GPa was also detected which could indicate a continuous second-order transition that begins before 12.8 GPa. This is illustrated in Fig. 4.13 where a discontinuity in the lattice parameters is shown at 12.8 GPa, however extrapolation of the a- and b- axis curves from β-CrO_2 back to the a-axis from α-CrO_2 could indicate a continuous transition beginning as low as 10.8 GPa. Indeed, in many other rutile-type oxides [83, 87, 82] the

transition to the $CaCl_2$ structure has been shown to be second-order with the spontaneous strain, $e_{ss} = (a - b)/(a + b)$, as the order parameter. According to Landaus theory of second-order phase transitions, the order parameter should be proportional to $(P - P_c)^{1/2}$. To examine this possibility, we have plotted e_{ss} vs. pressure in Fig. 5.4(a). Our data appear linear up to 25 GPa with a fit to a straight line giving a value of $P_c = 12.2$ GPa. Above 25 GPa, however, strong deviations from linearity are observed.

The splitting of the E_g mode in rutile materials has been shown to be directly proportional to the spontaneous strain and should therefore also follow a $(P-P_c)^{1/2}$ scaling [105]. The square of this splitting is plotted in Fig. 5.4(b). We again see good linearity up to 25 GPa, giving a value of $P_c = 10.0$ GPa, above which we see deviations. The agreement with $(P - P_c)^{1/2}$ below 25 GPa suggests that this is indeed a second-order transition. Although this scaling only rigorously applies near the transition pressure, the deviations at 25 GPa coincide with the new Raman peak observed at 33 GPa and the change in compressibility of the *c*-axis, and could indicate the appearance of a new phase. However, no indication of a second structural phase transition was found in the x-ray diffraction data. Therefore, further experiments are needed to make a solid conclusion.

The lower value of P_c obtained from our Raman data, compared to x-ray, is likely due to the use of different pressure media: argon for Raman and liq.-He for x-ray diffraction. Argon is known to provide slightly less hydrostatic conditions than liq.-He and therefore could have forced the transition to occur at a lower pressure during the Raman experiment. In addition, the larger compressibility of the *c*-axis observed in α-CrO_2 using mineral oil compared to that obtained using liq.-He, shown in Fig. 4.13, is also suggestive of a greater strain when using mineral verses using liq.-He. It has been shown by Haines *et al.*[87] that the rutile$\rightarrow CaCl_2$ transition is very sensitive to non-hydrostatic stress. It has been shown that the use of non-hydrostatic pressure media can lower the transition pressure by

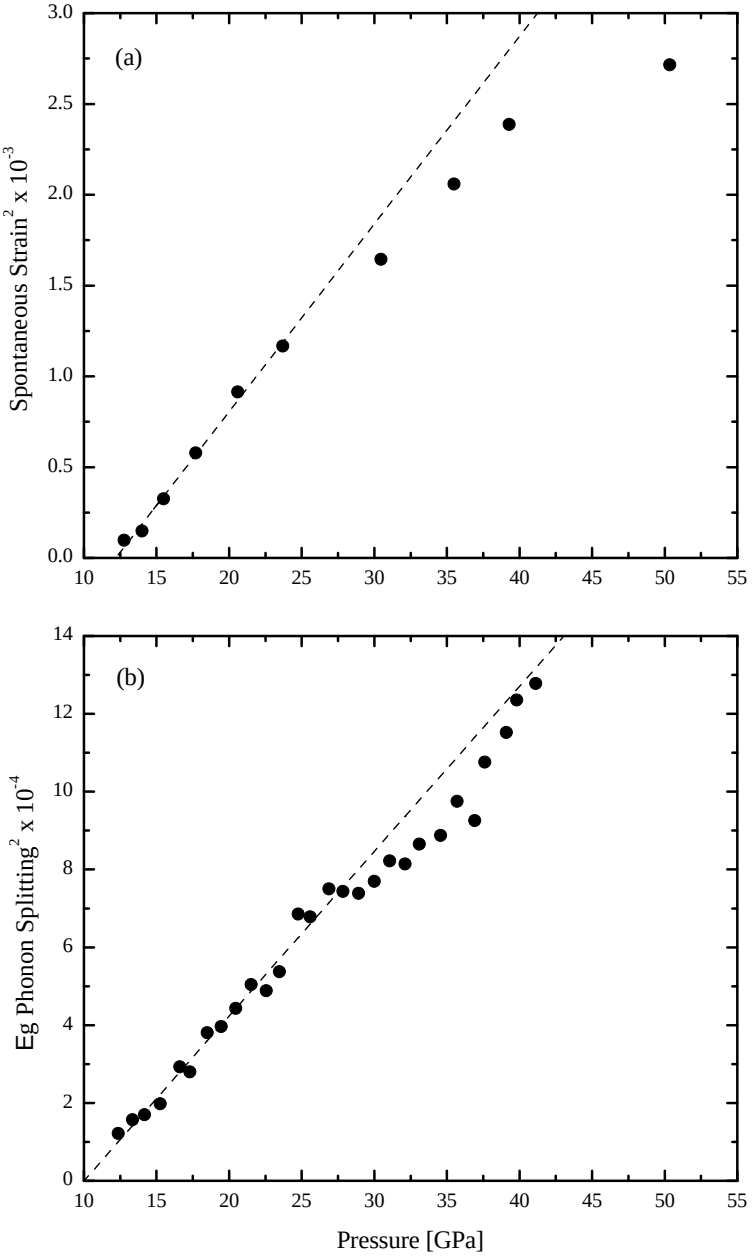

Figure 5.4. Plot of the square of the (a) spontaneous strain, defined as $|e_{ss}|^2 = (a-b)(a+b)$, and (b) E_g phonon splitting, defined as $|(\nu_1 - \nu_2)/(\nu_1 + \nu_2)|^2$, vs. pressure. Dotted lines show a linear fit of the form $(P - P_c)$ up to 25 GPa giving $P_c = 12.20$ GPa for (a) and $P_c = 10.0$ GPa for (b). Deviations from linearity are clear above 25 GPa.

as much as 8 GPa for SnO_2. Therefore, we place the transition at 12 ± 3 GPa based on the first appearance of a clear splitting of the diffraction lines with $h \neq k$ and estimate the experimental uncertainty to be ~ 3 GPa due to the discrepancy in P_c discussed above.

5.3.2 Lattice Softening and Electronic Phase Transitions

It is interesting to note that the extrapolated zero-pressure bulk modulus of β-CrO_2 is lower than that of α-CrO_2 going from $B_0 = 239 \pm 2$ to $B_0 = 162 \pm 2$ GPa across the phase transition (see Fig. 4.14 and Table 4.3.1). An alternative way of extracting compressibility data is to extract the instantaneous bulk modulus as a function of pressure from the pressure vs. volume data. Using the definition of the bulk modulus

$$\frac{1}{B(P)} = -\frac{1}{V}\left(\frac{\delta V}{\delta P}\right)_T \tag{5.1}$$

we can see that to calculate $B(P)$ we need to take the derivative of our $V(P)$ data. We can approximate $\delta V/\delta P$ at point n by fitting points $\{n-l, n-l+1, ..., n, ..., n+l-1, n+1\}$ with a straight line. Figure 5.5 shows the result of this procedure for values of $l = 1$ and $l = 2$. This is a relatively crude approximation to $\delta V/\delta P$, however it shows that there is indeed a marked reduction of the bulk modulus near the rutile$\rightarrow$$CaCl_2$ transition. For both values of l the bulk modulus drops to roughly the ambient pressure value. Since we have determined that this is a second-order transition, i.e. no first order change in the volume at the transition, then the only conclusion is that there is a significant reduction of the compressibility at the transition point.

Lattice softening is not uncommon for strain-driven distortive-type transitions at high pressures, as seen in materials like ReO_3 and UO_3 where the softening occurs as a result of buckling of the linear Re-O bonds [106, 107]. As previously discussed and shown in Fig. 4.14, the change in volume compressibility comes largely from an increase in compressibility

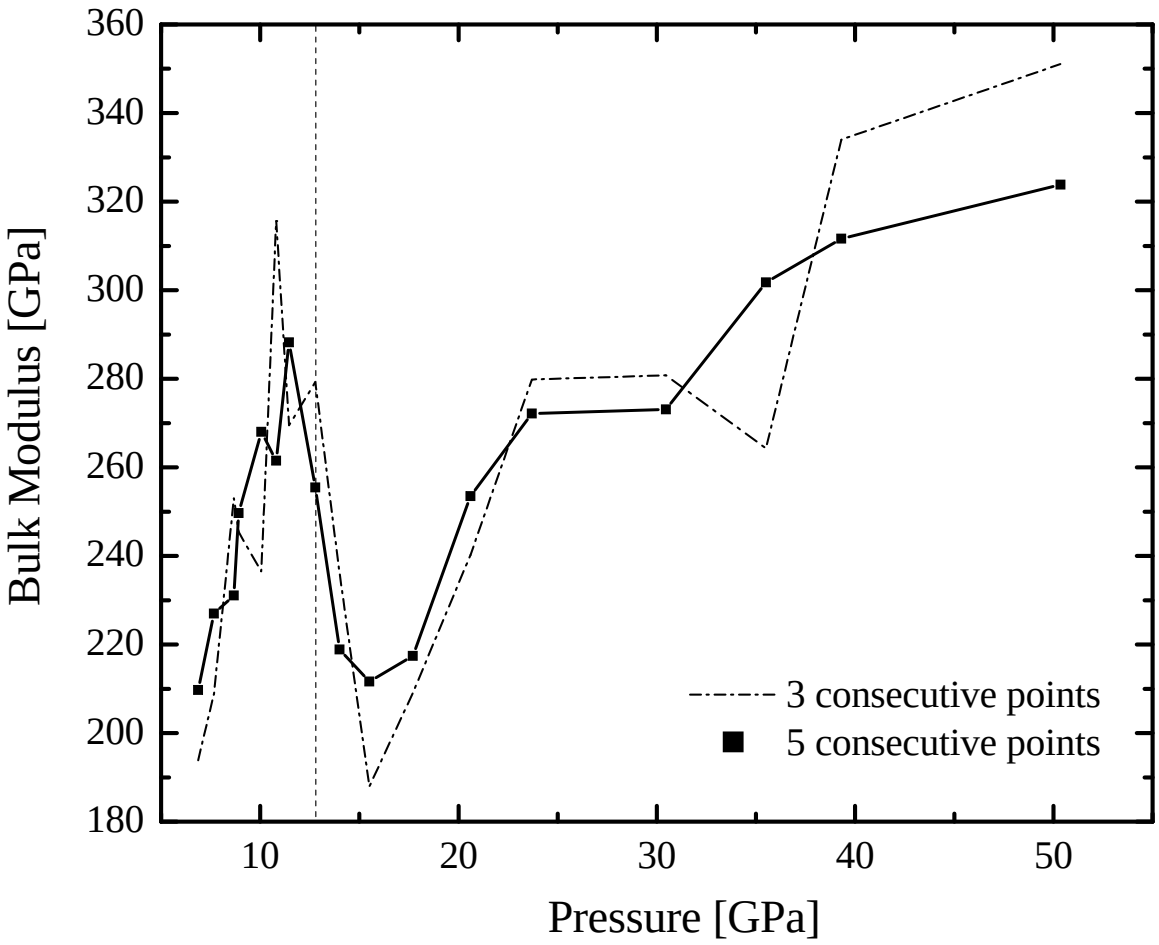

Figure 5.5. Instantaneous bulk modulus of CrO_2 extracted from PV data.

of the c-axis, not from a change in compressibility of the ab-plane as evident from observing the area conserving parameter $\sqrt{ab}$ as a function of pressure. A similar lattice softening has also been seen during the high-pressure rutile→α-PbO_2 transition in TiO_2 and PbO_2 which also involves a large change in the compressibility of the c-axis [89, 108]. In these materials the change in compressibility is due to the way the O-octahedra link along the c-axis, forming zig-zag edge-sharing chains instead of straight edge-sharing chains as in rutile. This increases the number of distortion mechanisms and hence a larger compressibility. The rutile→$CaCl_2$ transition, however, does not alter the way O-octahedra link along the c-axis and may therefore need an alternative explanation for the lattice softening.

The tetragonal distortion (apical Cr-O bond is shorter than the equatorial bonds) of the CrO_6 octahedra introduced in β-CrO_2 splits the doubly degenerate e_g molecular orbital into a_{1g} and b_{2g} states and splits the triply degenerate t_{2g} orbital into b_{2g} and e_g states [109]. The orthorhombic distortion in β-CrO_2 further splits this latter e_g orbital into b_{2g} and b_{3g} orbitals. As a result, the two unpaired d-electrons in d^2 CrO_2 can be paired up in the lowest energy d-orbital, either b_{2g} or b_{3g}, in a sufficiently strong crystal field. This would be equivalent to removing the exchange splitting of the up-spin and down-spin d-states and increasing the metallic character of CrO_2. Lattice softening due to changes in the electronic structure has been seen in a variety of materials. In the monochalcogenides of the rare-earths, such as TmTe, the anomalous increase in compressibility with pressure is attributed to continuous $4f$-$5d$ electron promotion, resulting in a semiconductor-metal transition [110]. Shock experiments on liq.-D_2 indicate a significant increase in compressibility accompanying the insulator-metal transition [111]. We therefore postulate that the increase in compressibility of CrO_2 at 12 GPa may be due to an electronic transition from half-metal to metal. Recent electronic structure calculations support this conjecture by showing that the density of state is much more sensitive to changes in the c-axis than either

the a- or b-axis [1].

5.3.3 Systematics in Rutile-Structured Compounds

The transition observed in the present study is in accordance with other MO_2-type transition metals or group-IV dioxides taking the rutile structure. For example, rutile-type MnO_2 undergoes a phase transition at 0.3 GPa to the $CaCl_2$ structure and possibly another phase transition around 46 GPa to an unknown cubic phase [82]. Other materials often undergo post-rutile phase transition to structures such as α-PbO_2, α-cristobalite, etc. Table 5.3.3 summarizes the results for many MO_2 compounds. To compare CrO_2 with the rutile-type compounds at high pressure and to gain insight into the systematics of these transitions we have plotted the metallic ion radii vs. transition pressure in Fig. 5.6(a). It should be noted that the structural results from Table 5.3.3 were taken from Bolzan *et al.* [2], however the values for the ionic radii were taken from Shannon and Prewitt [1]. The values used in Ref. [2] are those obtained by Ahrens which do not account for coordination number and spin state and, consequently, do not give the correct values for the anion-cation distances when added together. We see strong systematics in the group-IV dioxides showing increasing transition pressure with decreasing anion radius. The transition metals, however, show much more complex behavior.

To elucidate the connection between transition pressure and ambient pressure crystal structure parameters we have also calculated the degree of MO_6 octahedra distortion at ambient pressure, defined as $|(r_1 - r_2)/(r_1 + r_2)|$, where $r_1 \equiv$apical M-O distance and $r_2 \equiv$equatorial M-O distance. The values are plotted as a function of transition pressure in Fig. 5.6(b) and suggests that a higher degree of distortion leads to a dramatic increase in the stability range of the rutile structure. α-CrO_2, with an ambient pressure value of

[1] Unpublished LDA+U calculations by Kasinathan *et al.* confirm the insulating gap in the minority spin density of states is much more sensitive to compression of the c-axis than the a- or b- axis.

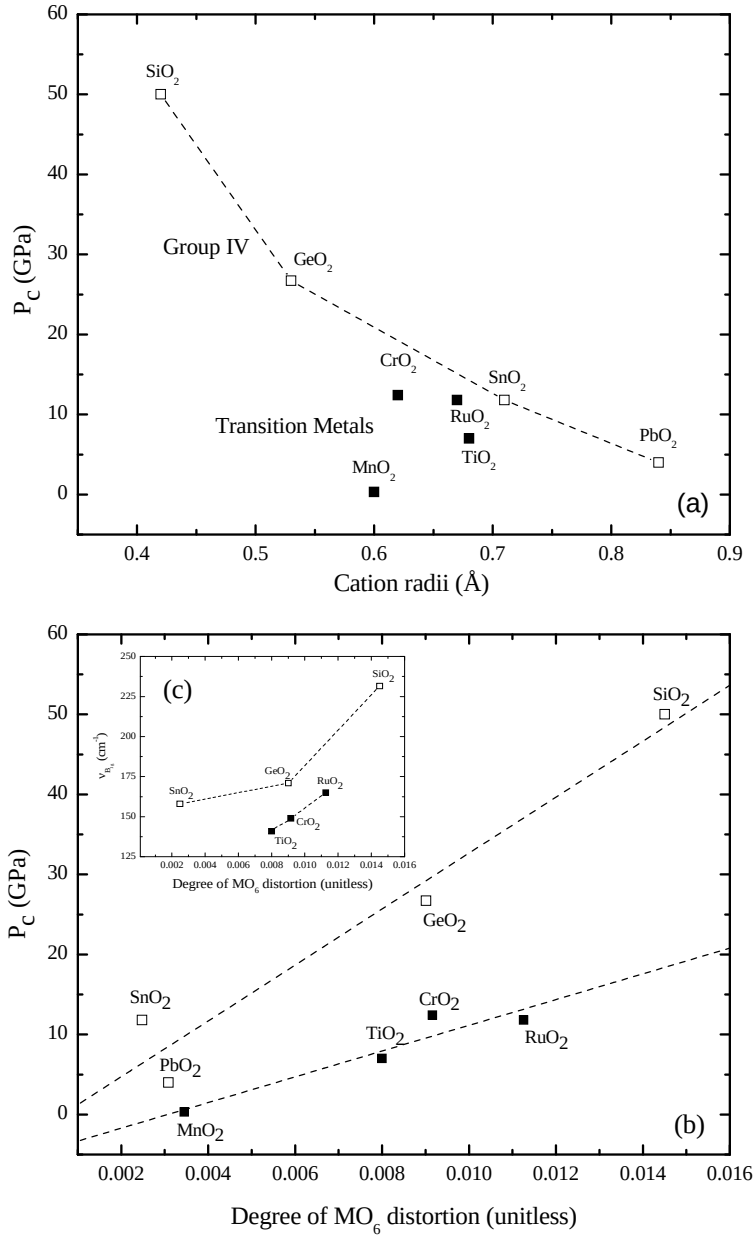

Figure 5.6. (a) Metallic ion radii for select MO_6 compounds vs. transition P_c. Open squares show group-IV oxides and dark squares show transition-metal oxides. Dotted line serves as a guide to the eye. (b) shows plot of the ambient pressure MO_6 distortion, defined as $|(a-b)/(a+b)|$ where $a \equiv$apical M-O distance and $b \equiv$equatorial M-O distance, vs. transition pressure (left axis, squares) and B_{1g} mode frequency (right axis, triangles). Light and dark squares represent the group-IV and transition-metal oxides, respectively. Dashed lines are linear fits. Inset (c) shows increase of B_{1g} mode frequency with increasing distortion.

MO_2 compound	Transition pressure (GPa)	Anion radii[a] (Å)	MO_6[b]	B_{1g} frequency (cm^{-1})
TiO_2[c]	7	0.745	0.008	141
CrO_2	12±3	0.69	0.00916	149
MnO_2	0.3	0.68	0.00345	
RuO_2	11.8	0.76	0.01126	165
SiO_2	50	0.54	0.0145	232
GeO_2	26.72	0.68	0.00901	171
SnO_2	11.8	0.83	0.00248	158
PbO_2	4	0.915	0.00309	

Table 5.1. Rutile to $CaCl_2$ transition pressure and ambient pressure anion radii, degree of MO_6 distortion, and B_{1g} mode frequencies for various metal and Group-IV oxides. [a]Anion radii obtained from Ref. [1] for the 4th oxidation state and 6-fold coordination. [b]Structural information for metal and Group-IV oxides at ambient conditions is summarized in Ref. [2]. [c]Transition pressure for rutile to α-PbO_2 in TiO_2.

0.00916, agrees well with the other transition-metal compounds. It should also be noted that, although the group-IV compounds and transition-metal compounds both follow a nearly linear trend, the line of transition-metal compounds is below that of group-IV. We can try to understand this behavior by looking at the B_{1g} vibrational mode frequency, ν_{B1g}, at ambient pressure for the various MO_2 compounds as a function of transition pressure. This is plotted in Fig. 5.6(c). We can see that an increased distortion of the MO_6 octahedra leads to an increase in ν_{B1g}. Since the rutile-$CaCl_2$ transition is driven by a mechanical instability with the same symmetry as the B_{1g} mode, demonstrated by softening of this mode, a material with a higher ambient pressure value for ν_{B1g} may take longer to transform, leading to a higher value for P_c. The fact that for a given distortion, the values of ν_{B1g} for the transition metal oxides are systematically lower, leading to lower values for P_c, may be electronic in nature. The bonding between M-O in the transition metal oxides is dominated by its partially-filled d orbitals where in the group-IV compounds, this same bonding has predominantly p character.

Chapter 6

Conclusions

6.1 The Mott Transition in MnO

The first confirmation of a Mott transition at high pressure in the transition-metal monoxides was presented for MnO. Using $K\beta$ XES, we observed a collapse of the $3d$ magnetic moment at 108 GPa. We also showed, through a re-analysis of resistance data collected by Patterson *et al.*, that the collapse of the $3d$ moment coincided with a first-order metallization, placing the Mott transition at 105 ± 5. This metallization was confirmed by visual observations of our sample.

A structural study of MnO also clarified the ill-characterized "intermediate phase" region reported by Kondo *et al.* [4]. They argued that because their hexagonal indexing gave a larger volume at 90 GPa than the $dB1$ phase at 80 GPa, the region between 90 and 120 GPa might be characterized by a single, new phase rather than a mixed phase. However, an analysis of our diffraction data on MnO reveals that the pattern between 90 and 120 GPa corresponds to a mixed phase region of the lower pressure $dB1$ phase and the high pressure $B8$ phase. In addition to the clarification of the pressure region between 90 and 120 GPa, we also discovered that the insulator-metal transition at 105 ± 5 GPa

also coincides with an isostructural 6.6% volume-collapse phase transition within the $B8$ phase. Using the results summarized above, we present the phase diagram of MnO (see Fig. 5.3), combining our results with that of shock measurements [112] on MnO and Mössbauer spectroscopy measurements on FeO, and present a complete picture of the Mott transition in MnO.

6.2 Delocalization Phenomenon in the Rare-Earths

Using Resonant-Inelastic X-ray Scattering at the L_{III} edge, we were able to probe the electronic structure of Gd metal across the volume-collapse transition at 60 GPa, up to over 1 MBar. The behavior of the RIXS spectrum was similar to that obtained during the pressure-induced valence change in YbS (f^{14} in Yb^{2+} and f^{13} in Yb^{3+}) [77], and during the γ-α transition in the Ce alloys [9, 78], *i.e.*, a new peak was seen to develop as a function of pressure which was associated with an increase in the $4f^8$ component of the ground state wavefunction $|\Psi\rangle = \alpha|4f^7v^3\rangle + \beta|4f^8v^2\rangle + \gamma|4f^6v^4\rangle$ of Gd. This interpretation allowed us to quantitatively measure the degree of $4f \rightarrow (5d6s)$ hybridization (delocalization) as a function of pressure by extracting the f-occupancy ratio $n(f^8)/n(f^7)$. Our results are compared with DMFT calculations using a Kondo-like model [10] and ambient pressure RIXS [9] on Ce metal and show a roughly exponential, continuous, and prolonged delocalization consistent with DMFT calculations.

By applying $L\gamma_1$ XES to the rare-earths at high pressure we were able to probe the $4f$ moment across their respective volume-collapse transitions and compare with our results on the Mott transition in MnO. Our data on Ce, Pr, and Gd revealed there was no change in the $4f$ moment to the highest pressures achieved, well past the volume-collapse transition pressures. The results were the same on Nd metal, which has no such VCT. These results are

in striking contrast with MnO, which showed a collapse of the $3d$ magnetic moment, and are inconsistent with a Mott transition model for the delocalization of the rare-earths. These results are consistent, however, with a Kondo VCT model where increasing hybridization at high pressure screens the local $4f$ moment, as seen in magnetic susceptibility, but allows XES and high-energy neutron scattering to interact with a bare $4f$ moment.

6.3 Half-Metals at High Pressure

An investigation of the half-metallic ferromagnet CrO_2 revealed a structural phase transition at 12±3 GPa from the common rutile structure to the $CaCl_2$ structure. We have also shown that this transition is second-order by comparing the splitting of the (101) diffraction peak and the E_g phonon splitting to the scaling $(P-P_c)^{1/2}$ predicted by Landau's theory of second-order phase transitions. However, the scaling breaks down at 25 GPa in both the diffraction peak splitting and the E_g phonon splitting, suggesting a second phase transition, a proposition supported by the appearance of a new Raman mode at 33 GPa and a change in compressibility of the $c-$axis around that pressure.

We also detected an anomalous softening of the lattice across the phase transition at 12 GPa by fitting both the low pressure and high pressure PV data using various equations of state. Both the Birch-Murnaghan and the Vinet equations of state show a marked reduction in B_0 across the phase transition. The fits to the Birch-Murnaghan EOS, the most widely used EOS in high pressure physics today, estimate a change in B_0 of -77 GPa across the transition, assuming a fixed value of $B' = 4$. We also verified this result by brute-force extraction of the instantaneous bulk modulus. This method, although a crude approximation of the derivative, shows a dramatic drop in the instantaneous bulk modulus at the transition. We suggest this softening may be due to a half-metal to metal transition

as the softening comes primarily from an increase in compressibility of the c-axis, the axis most sensitive to electronic structure.

Finally, we put the transition pressure of the rutile-$CaCl_2$ transition in CrO_2 in context with other rutile transitions in the transition-metal and group-IV dioxides. We found strong systematics when plotting the degree of MO_6 distortion in these materials as a function of transition pressure and link this to the ambient pressure Raman shift of the B_{1g} phonon. The rutile-$CaCl_2$ transition was shown to be driven by the softening of this mode. It was argued that a higher ambient pressure value for the B_{1g} Raman mode should lead to an increase in transition pressure.

6.4 Future Work

6.4.1 Eu and EuN

Divalent Eu (and Yb) is an exception among the lanthanides. Most rare-earths are trivalent in solid due to the energy advantage to promoting a $4f$ electron into the valence orbitals and forming a metallic bond. Eu, however, is divalent because a half-filled $4f^7$ configuration is more stable than a $4f^6$ configuration. As a result, a pure valence transition occurs in Eu (and Yb) at high pressure, going continuously from a divalent $4f^7$ configuration to a trivalent $4f^6$ configuration, ending between 12 GPa [113] and 20 GPa [114]. This change should manifest itself in $L\gamma_1$ XES measurements as a reduction of the $L\gamma_1'$ satellite peak intensity and will be an important check to verify that this technique does indeed give a measure of the $4f$ moment. EuN is also unusual in that $J_{Total} =)$ due to a $S = 6$, $J = 6$ configuration. This is also an important materials to study using $L\gamma_1$ XES since there has been some debate to whether this technique measures total spin S or total angular momentum J.

Preliminary Results in Eu

Preliminary XES results were obtained on Eu metal to 45 GPa. However, our first attempt was plagued by gasket contamination. Figure 6.1 shows Eu XES taken during this first run. At 2 GPa, the main peak occurs at 7477 eV and is tentatively assigned to the $L\gamma_1$ peak of Eu. However, this is 3.3 eV lower than expected for Eu metal (7480.3 eV from Ref. [56]). The low energy $L\gamma_1'$ satellite peak appears at 7457 eV, a separation of only 20 eV. By 25 GPa, a 2 eV shift in position of the $L\gamma_1'$ peak toward the main peak is observed. The spectrum at 45 GPa appears unchanged from that obtained at 25 GPa. However, Ni $K\alpha$ XES at 7461 eV, shown in Fig. 6.1 as the dashed spectrum, lies very close to the shifted $L\gamma_1'$ satellite peak. It is known that the standard Be gasket contains up to 400 ppm Ni (see Sec. 3.1.3). These contaminations from the gasket have interfered with previous experiments (see Pr XES Sec. 4.2.2). Therefore, a second Eu XES run was conducted to rule out Ni contamination.

The results from our second Eu XES run are shown in Fig. 6.2 at 2 GPa and 45 GPa. The positions of the main $L\gamma_1$ and $L\gamma_1'$ satellite peak are consistent with those obtained during our first run, lying at 7477 eV and 7457 eV, respectively. Similar to what we saw during the first run, a 2 eV shift in the low energy $L\gamma_1'$ satellite peak position toward the main peak was observed. However, this shift was seen only at 45 GPa, not at 25 GPa as in the first run. The Ni content of the high purity gasket used during this second run is less than 1/10 that of the standard Be gasket used in the first run. We can therefore rule out any effect caused by Ni contamination. However, the origin of the 3.3 eV discrepancy between the position of the main $L\gamma_1$ line in our data vs. the literature remains unresolved.

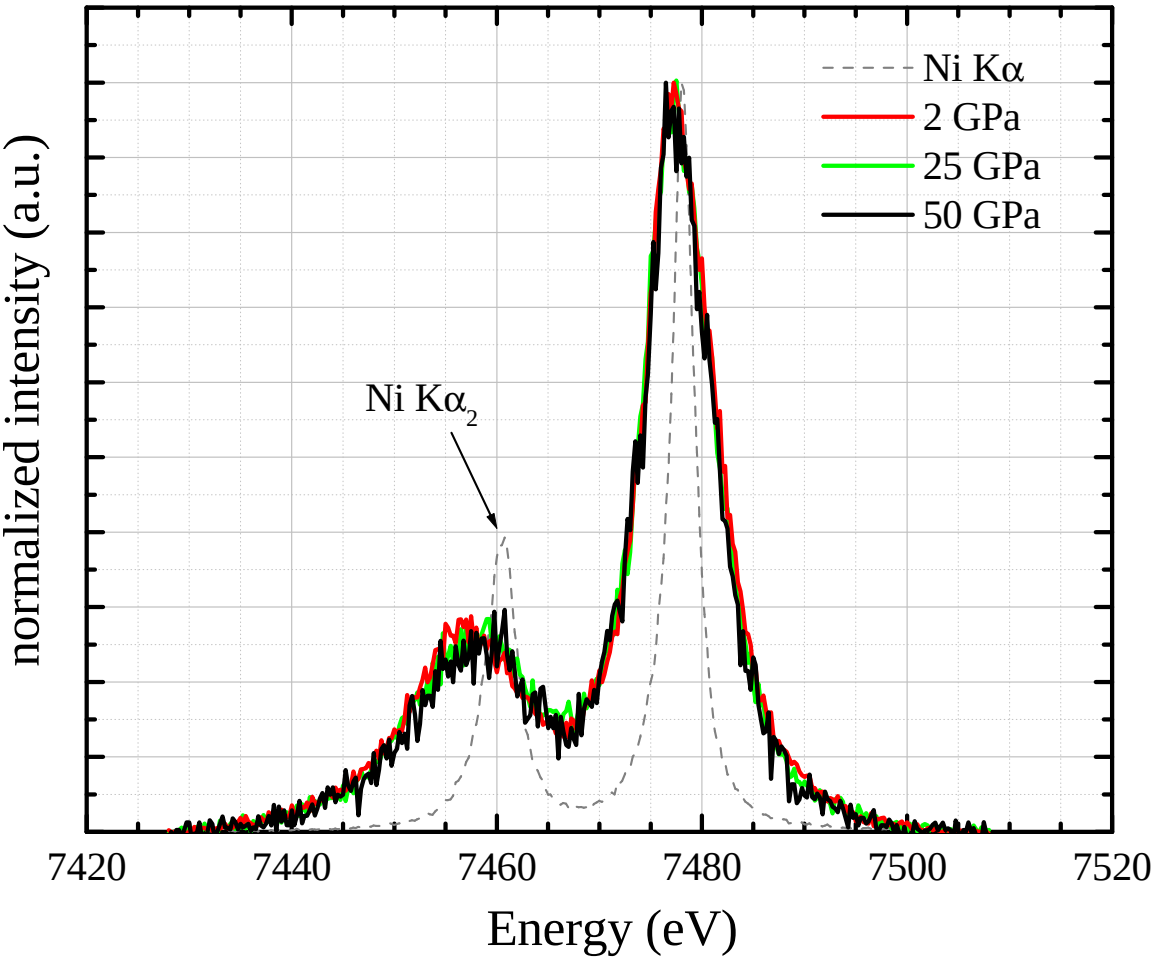

Figure 6.1. $L\gamma_1$ XES spectra of Eu at 2, 25, and 50 GPa from our first run. The main peak, shown here at 7477 eV, is assumed to be the $L\gamma_1$ line. At 2 GPa (solid red line), the the $L\gamma_1'$ satellite peak is at 7457 eV. At 25 GPa (solid green line) and 50 GPa (solid black line) the $L\gamma_1'$ line appears shifted toward the main peak by $\sim$ 2 eV. Overlaid is a Ni $K\alpha$ XES spectrum showing that the $K\alpha_2$ line appears at 7461 eV, very close in energy to the shifted $L\gamma_1'$ satellite peak at high pressure.

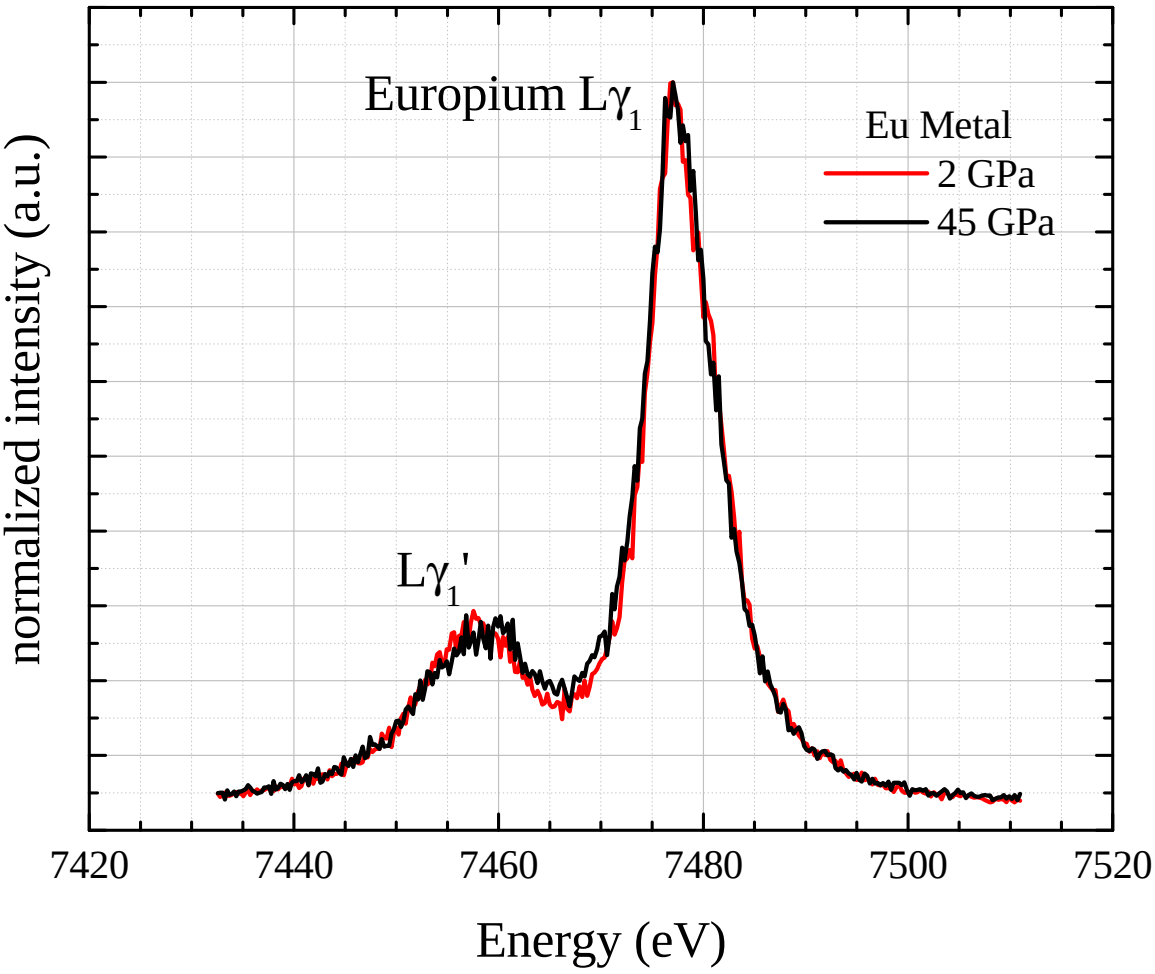

Figure 6.2. Results from our second run of Eu XES showing spectra taken at 2 GPa and 45 GPa. The positions of the main $L\gamma_1$ and $L\gamma_1'$ satellite peaks are consistent with those obtained during our first run, lying at 7477 eV and 7457 eV, respectively. At 45 GPa, The $L\gamma_1$ line is seen to shift toward the main peak by ~ 2 eV, similar to what was seen during our first run. However, during our second run, this shift wasn't seen until 45 GPa.

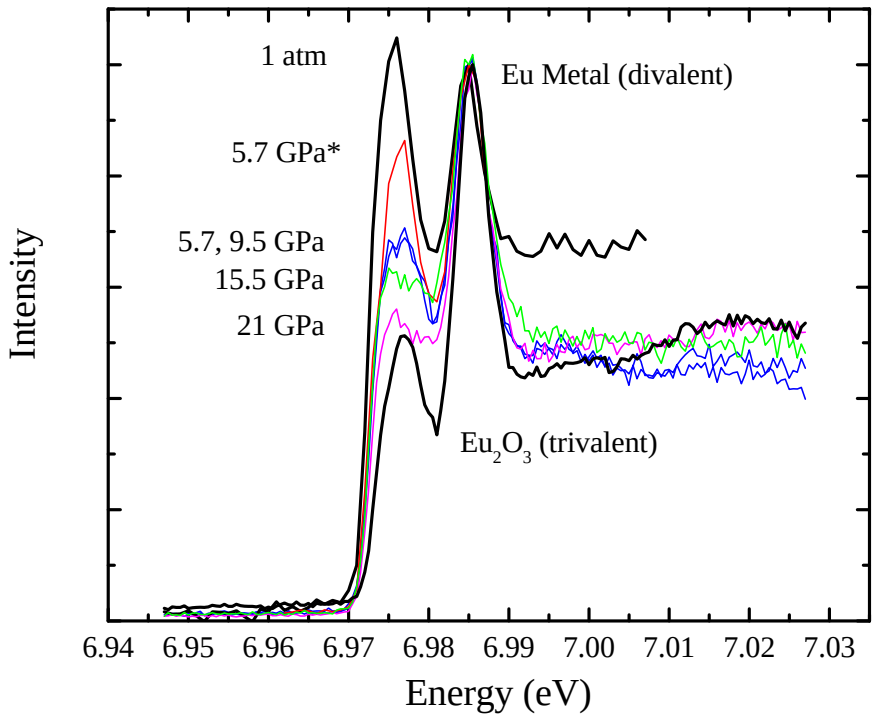

Figure 6.3. Preliminary results from Eu RIXS showing PFY scans taken with increasing pressure, and at different times. The 5.7 and 9.5 GPa spectra were taken only minutes apart, whereas an 8 hour interval between the other pressure points elapsed. The spectra marked with an asterisk was reconstructed from a 2D RIXS scan at 5.7 GPa showing the time dependent change at a given pressure.

Time Dependent Effects

Figure 6.3 shows partial fluorescence yield (PFY) scans from a preliminary RIXS experiment on Eu loaded in mineral oil, in steps of 5 GPa. With increasing pressure, the relative intensity of the two main edges, presumably associated with divalent and trivalent Eu ions, changes. At first glance it appears as though pressure is driving the sample towards the spectra associated with trivalent Eu_2O_3. However, the 5.7 GPa and 9.5 GPa are directly overlapping, inconsistent with the previous reports of a smooth, continuous transition to the divalent state in Eu metal.

Our data can be reconciled with the literature on Eu metal by correlating the time

the individual spectra were taken with the intensity ratio of the divalent and trivalent peaks. Each PFY scan was taken after first increasing the pressure and taking an 8-hour RIXS scan. However, the 9.5 GPa PFY scan was taken immediately after increasing pressure, instead of after the RIXS scan. Therefore, we can conclude that the 5.7 and 9.5 GPa scans are identical due to the short time interval between the two scans, whereas the large changes seen between the ambient-5.7 GPa, 9.5-15.5 GPa, and 15.5-21 GPa were due to some time-dependent changes of the sample. Additional evidence for this effect is shown in the 5.7 GPa spectra marked with an asterisk, which was reconstructed from the 2D RIXS spectra taken at 5.7 GPa. This clearly demonstrates time-dependent changes occurring within the same pressure point.

The nature of these time-dependent changes is unclear. One possible explanation is sample oxidation caused by the use of mineral oil as a pressure medium. Indeed, one can watch a Eu sample, freshly cut from the ingot, change color when placed in mineral oil. However, kinetic effects are also common when electronic phase transitions are coupled with structural transitions. Reports of the $bcc \rightarrow hcp$ transition in Eu place the transition pressure at either 12 GPa [115] or 18 GPa [116]. A similar discrepancy was found in the preliminary XES results presented in Sec. 6.4.1. Reference [115] attributed this discrepancy to impurities in the Eu specimens as well as to non-hydrostatic conditions. However, our samples were obtained from the same Eu stock and both samples used the same pressure medium (mineral oil), thus kinetic effects cannot be ruled out.

Our $L\gamma_1$ XES and $2p3d$ RIXS experiments should be repeated using more stringent sample loading procedures. Specifically, the sample should be loaded in a dry, inert gas environment. An inert pressure medium such as He or Ne should also be used. Argon gas is too heavy (Z=18) for use as a pressure medium in $L\gamma_1$ XES sample.

Preliminary Results on EuN

A preliminary XES experiment was performed on EuN to 85 GPa using 14.417 keV using two different samples, the first using a standard Be gasket and the second using a thin Re gasket (see Sec. 3.1.3). EuN powder was made by Mark Bailey at Cornell University. Because our Eu metal XES experiments were contaminated with Ni $K\alpha_2$ emission (see Sec. 6.4.1), the results from our first XES experiment on EuN using a standard Be gasket are not shown. Figure 6.4 shows the results of the second $L\gamma_1$ XES experiment on EuN, using a thin Re gasket, up to 82 GPa. At 8 GPa, the spectra consists of the main $L\gamma_1$ peak at 7477 eV and a low energy $L\gamma_1'$ satellite peak at 7455, a separation of 22 eV. Note that the main peak occurs at the same energy seen in our Eu metal XES results shown in Sec. 6.4.1. No changes are detected in the XES spectra until 82 GPa where a shift in the positions of the main peak and satellite peaks to 7476 eV and 7456 eV, respectively, reducing the separation of the peaks to 20 eV. In addition, a slight reduction in the satellite peak intensity is also observed at 82 GPa. Both observations are consisted with a slight reduction in the $4f$ moment of EuN at 82 GPa. The changes described above (and in Sec. 6.4.1 for Eu metal) show measurable changes in the XES spectrum at high pressure. This is in contrast to Ce, Pr, Nd, and Gd which all show no changes in their XES spectra well past their respective volume-collapse transitions. The null result obtained for those four materials can be interpreted as no change in the $4f$ local moment at high pressure. However, the changes in EuN (and Eu metal) are more difficult to interprate. The changes can be due to a reduction of the $4f$ moments due to changes in electron correlation. However, changes in crystal structure can also effect the XES spectrum by altering the exchange interaction. Further experiments on EuN (and Eu) should be accompanied by theoretical calculations to uniquely identify the cause of any changes in the XES spectrum.

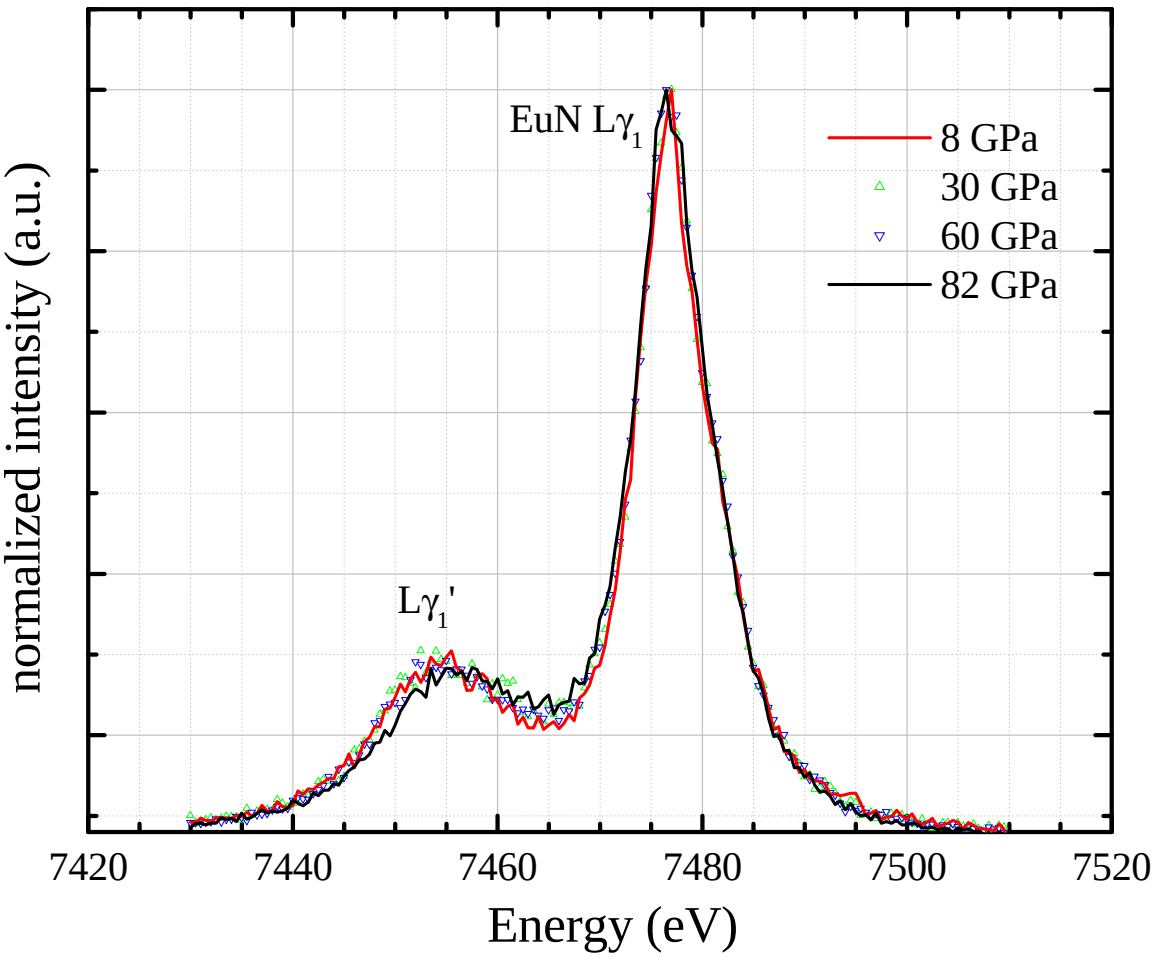

Figure 6.4. A comparison of EuN XES spectra a 8, 30, 60 and 82 GPa. At low pressure, the spectrum consists of the main $L\gamma_1$ peak at 7477 eV and a low energy $L\gamma_1'$ satellite peak at 7455 eV. No change is observed in the intensity or position of the satellite peak to 60 GPa. At 82 GPa, a shift in position of both peaks are observed, with final energies of 7476 and 7456 eV for the main peak and satellite peaks, respectively. A slight reduction in the satellite peak intensity is also observed at this pressure. Both observations are consistent with a slight decrease in $4f$ moment.

6.4.2 High Resolution IXS

The IXS experiment performed on the lanthanides described in this work achieved an energy resolution of ~ 1 eV. This resolution was primarily limited by the radius of the Rowland circle and the quality of the crystal analyzer. A 1 eV resolution was sufficient for probing the electronic structure of Gd as the features corresponding to different $4f$ occupations were separated by at least 2 eV. However, a more direct approach to the study of correlated materials would be to directly probe the Mott-Hubbard gap at high pressure. Recent work on high-T_c cuprate superconductors have been successful at probing this gap with an energy resolution of 400 meV [117]. The application of this technique to the transition-metal oxides and rare-earth metals would require even higher energy resolution since pressure narrows this gap. As IXS experiments improve, it will be possible to probe the Mott-Hubbard gap with the necessary emission energy resolution of $\sim 100 - 200$ meV and incident energy resolution of ~ 100 meV. Applying these techniques to the transition-metal oxides and rare-earth metals at high pressure would enable us to directly compare experimental and theoretical values for the Mott-gap excitations.

6.4.3 Rutile Compounds:CrO_2 at Low T

Preliminary Raman data on CrO_2 at low temperature, taken during my first few months at LLNL, showed an unusual fifth Raman peak that was much more intense than the four Raman-active phonon peaks of the rutile structure. This fifth peak also shifted much more strongly with pressure. Figure 6.5(a) shows this peak where Fig. 6.5(b) shows the Raman shift of all the peaks as a function of pressure. The origin of this peak is unknown and could indicate a structural phase transition However, because it only arises at low temperature, a magnon peak should not be ruled out. Unfortunately, problems with the cryostat coupled with higher priority projects prevented further investigations of this

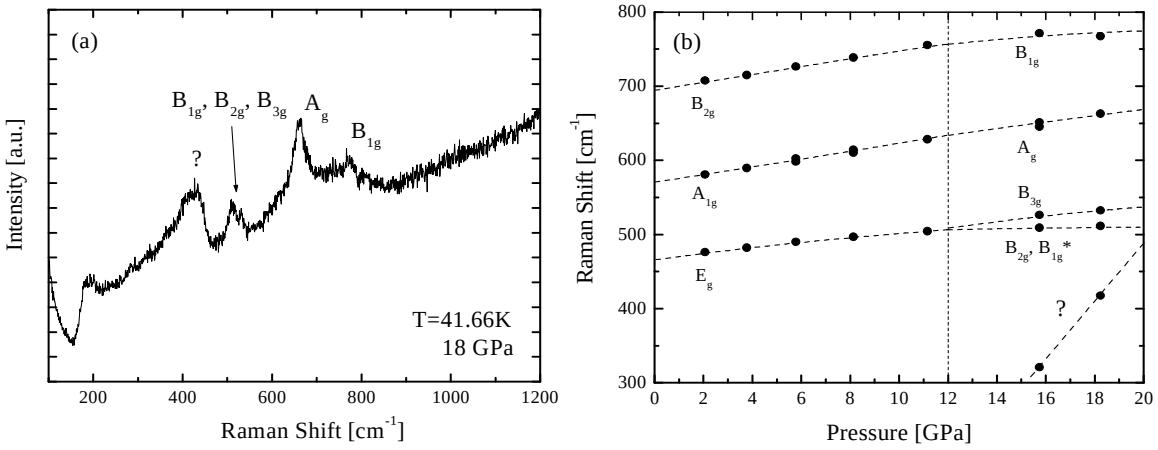

Figure 6.5. Preliminary Raman data on low temperature CrO_2. (a) shows the Raman spectra of CrO_2 at 18 GPa and 43 K. Peak assignments are based on the $CaCl_2$ phase of CrO_2 (see Sec. 4.3.1). (b) shows the extreme changes in the Raman shift of the anomalous peak with pressure compared to the phonon modes. *We did not observe the B_{1g} peak of the $CaCl_2$ structure, presumably due to the poor quality data obtained on this system (data taken before high-sensitivity Raman system was developed. See Sec. 3.3.2).

anomaly. A thorough study of CrO_2 at low temperature using Raman spectroscopy and x-ray diffraction should be conducted. In addition, VO_2, another rutile structured transition-metal oxide (albeit at elevated temperatures), has not been studied at high pressure. It also undergoes a metal-insulator transition at $T < 340$ K, below which VO_2 is an insulator [118]. Pressure should also drive VO_2 though a metal-insulator transition at ambient temperature.

Raman spectroscopy and ADXRD should be performed on VO_2 at high pressure in order test the systematics presented in Sec. 5.3.3 on the rutile-CaC_2 transition pressures as a function of MO_6 octahedral distortion and to study any metal-insulator transitions.

Appendix A

The Bragg Condition

There are many approaches used to understand the phenomenon of the diffraction of x-rays and the derivation of Bragg's Law, however the most straightforward is the Bragg construction. This approach is illustrated in Fig. A.1 and assumes specular reflection of the x-ray off the crystalline planes. For the x-ray beam to be reflected there must be constructive interference between photons reflected off two (or more) successive surfaces. This will occur when the path length difference, $(L_1 - L_2)$, between the two photons are $n\lambda$ where λ is the wavelength of the x-ray photons [62]. We can calculate L_1 to be

$$cos\,(90 - \theta_B) = \frac{d}{L_1}$$

Solving for L_1, using the identity $cos\,(90 - \theta_B) = sin\,\theta_B$ gives

$$L_1 = \frac{d}{cos\,(90 - \theta_B)} \tag{A.1}$$

$$= \frac{d}{sin\,\theta_B} \tag{A.2}$$

We can also calculate L_2 the same way starting with

$$cos\,2\theta_B = \frac{L_2}{L_1}$$

and solving for L_2 to give

$$L_2 = L_1 \, cos \, 2\theta_B \tag{A.3}$$

$$= \frac{d \, cos \, 2\theta_B}{sin \, \theta_B} \tag{A.4}$$

We can now derive Bragg's Law for constructive interference

$$n\lambda = L_1 - L_2 \tag{A.5}$$

$$= \frac{d}{sin \, \theta_B} - \frac{d \, cos \, 2\theta_B}{sin \, \theta_B} \tag{A.6}$$

$$= \frac{d \, (1 - cos \, 2\theta_B)}{sin \, \theta_B} \tag{A.7}$$

$$= \frac{2d \, sin^2 \, \theta_B}{sin \, \theta_B} \tag{A.8}$$

$$n\lambda = 2d \, sin \, \theta_B \tag{A.9}$$

using the identity $1 - cos \, 2\theta_B = 2 \, sin^2 \, \theta_B$.

Equation A.9 shows that, for Bragg diffraction to occur in a single crystal, one must either vary the incident x-ray energy to match the individual lattice planes, or keep the incident energy fixed and vary the angle of incident by rotating the crystal. The first method was used by von Laue and is called energy-dispersive x-ray diffraction (EDXRD). The second method, or angle-dispersive x-ray diffraction (ADXRD), is now more common due to the introduction of synchrotron radiation which is able to produce much more intense sources of monochromatic x-rays then was available during the early part of the 20^{th} century. In addition, the powdered samples primarily used in high pressure experiments require monochromatic light (see Sec. 3.2.2). Consequently, ADXRD was used for all experiments described in this dissertation.

Specific lattice planes are described using the notation (hkl) which defines a vector, $\vec{n} = h\hat{a_1} + k\hat{a_2} + l\hat{a_3}$, normal to the surface of the lattice plane, where $\hat{a_1}$, $\hat{a_2}$, and $\hat{a_3}$ are the lattice vectors of the crystal. In single-crystal diffraction each (hkl) would correspond to a

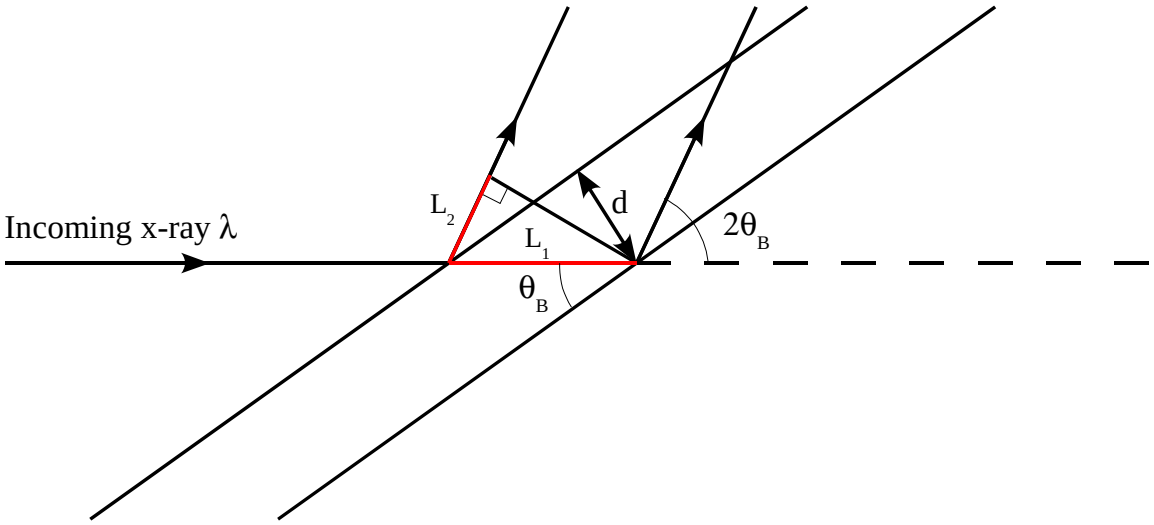

Figure A.1. A schematic diagram illustrating the Bragg condition for x-ray diffraction off a crystalline lattice. The angle between the incoming coherent x-ray beam and a crystal plane with spacing d is θ_B. The condition for constructive interference between x-ray photons reflected off the two successive surfaces is given by Bragg's Law, $n\lambda = 2dsin(\theta_B)$, where n is the order of the reflection.

single spot in the diffraction pattern. However, not all values of (hkl) produce diffraction spots. This is because at each lattice point, defined by the lattice vectors, there can exist a basis of atoms defined by their basis vectors. For example, the simple cubic lattice has a one atom basis with a zero basis vector. However, the body-centered cubic lattice has a 2-atom basis, one atom at $\vec{b_1} = 0\hat{a_1} + 0\hat{a_2} + 0\hat{a_3}$ and the other at $\vec{b_2} = \frac{1}{2}\hat{a_1} + \frac{1}{2}\hat{a_2} + \frac{1}{2}\hat{a_3}$. Because the x-ray beam will interact with all atoms in the basis, some diffraction lines which are present in the simple cubic lattice will be absent in the *bcc* structure because of interference. In general, the atoms in the basis need not be identical. As a result, each compound will have a unique diffraction pattern based on its crystal structure and chemical composition with the diffracted spot intensities being a function of the crystal structure and atom basis.

Appendix B

Origin of the Raman Effect

A rigorous treatment of the Raman process requires a bit of quantum mechanics, however the basic origin of the Raman effect can be derived using a classical description. To illustrate this process consider a single molecule placed in an electromagnetic field. The polarization of a molecule in an electric field is given by given by

$$\vec{P} = \alpha \cdot \vec{E} \tag{B.1}$$

where α is the polarizability tensor. Equation B.1 can be written explicitly as

$$\begin{bmatrix} P_x \\ P_y \\ P_z \end{bmatrix} = \begin{bmatrix} \alpha_{xx} & \alpha_{xy} & \alpha_{xz} \\ \alpha_{yx} & \alpha_{yy} & \alpha_{yz} \\ \alpha_{zx} & \alpha_{zy} & \alpha_{zz} \end{bmatrix} \begin{bmatrix} E_x \\ E_y \\ E_z \end{bmatrix} \tag{B.2}$$

Given that the electric field can be written as

$$\vec{E} = \vec{E_0}\ cos\ 2\pi\nu_0 t \tag{B.3}$$

and substituting Eq. B.3 into Eq. B.1, the polarization is then

$$P_i = \alpha_{ij} E_{j0}\ cos\ 2\pi\nu_0 t \tag{B.4}$$

With *apriori* knowledge that the Raman process is associated with the interaction between photons and the normal modes of vibration in a material we can expand the polarizability using a Taylor series in the normal mode vectors, Q_k. The polarizability is then given by

$$\alpha_{ij} \approx \alpha_{ij0} + \sum_k \left(\frac{\delta\alpha_{ij}}{\delta Q_k}\right)_0 Q_k \tag{B.5}$$

Because the Q_ks are normal modes of the material their time dependence can be written as

$$Q_k = Q_{k0}\, cos\, 2\pi\nu_k t \tag{B.6}$$

Substituting Eqns. B.5 and B.6 into Eq. B.4 gives the equation for the polarizability

$$P_i = \left(\alpha_{ij0} + \sum_k \left(\frac{\delta\alpha_{ij}}{\delta Q_k}\right)_0 Q_{k0}\, cos\, 2\pi\nu_k t\right) E_{j0}\, cos\, 2\pi\nu_0 t \tag{B.7}$$

which can be expanded to

$$P_i = \alpha_{ij0}E_{j0}\, cos\, 2\pi\nu_0 t + \frac{1}{2}\sum_k \left(\frac{\delta\alpha_{ij}}{\delta Q_k}\right)_0 Q_{k0}E_{j0}\left[cos\,(\nu_0 - \nu_k)2\pi t + cos\,(\nu_0 + \nu_k)2\pi t\right] \tag{B.8}$$

using the identity $cos\, x\, cos\, y = 1/2[cos\,(x+y)\, cos\,(x-y)]$. The first term in Eq. B.8 describes normal Rayleigh scattering where the emitted radiation from the oscillating dipole is the same frequency as the incident electric field. However, the second term in Eq. B.8 describes radiation that has been shifted either up or down in frequency by an amount ν_k corresponding to the normal mode frequency. This shifted radiation is the Raman scattered light. Another important consequence of Eq. B.8 is that in order for the second term to be non-zero, $\left(\frac{\delta\alpha_{ij}}{\delta Q_k}\right)_0$ must also be non-zero. Physically this means that for a normal mode to be "Raman active", the change in polarizability along the normal mode direction must be non-zero at equilibrium [119].

Bibliography

[1] R. D. Shannon and C. T. Prewitt, Acta Crystallogr., Sect. B: Struct. Crystallogr. Cryst. Chem. **25**, 925 (1969).

[2] A. Bolzan, C. Fong, B. J. Kennedy, and C. J. Howard, Acta Crystallogr., Sect. B: Struct. Sci. **53**, 373 (1997).

[3] A. K. McMahan, C. Huscroft, R. T. Scalettar, and E. L. Pollock, J. Comp.-Aided Mat. Des. **5**, 131 (1998).

[4] T. Kondo, T. Yagi, Y. Syono, Y. Noguchi, T. Atou, T. Kikegawa, and O. Shimomura, J. Appl. Phys. **87**, 4153 (2000).

[5] J. R. Patterson, C. M. Aracne, D. D. Jackson, V. Malba, S. T. Weir, P. A. Baker, and Y. K. Vohra, Phys. Rev. B **69**, 220101 (2004).

[6] G. Peng, F. M. F. deGroot, K. Hämäläinen, J. A. Moore, X. Wang, M. M. Grush, J. B. Hastings, D. P. Siddons, W. H. Armstrong, O. C. Mullins, and S. P. Cramer, J. Am. Chem. Soc. **116**, 2914 (1994).

[7] K. Jouda, S. Tanaka, and O. Aita, J. Phys. Cond. Matt. **9**, 10789 (1997).

[8] S. Tanaka, H. Ogasawara, K. Okada, and A. Kotani, J. Phys. Soc. Japan **64**, 2225 (1995).

[9] J.-P. Rueff, C. F. Hague, J.-M. Mariot, L. Journel, R. Delaunay, J.-P. Kappler, G. Schmerber, A. Derory, and N. Jaouen, Phys. Rev. Lett. **93**, 067402 (2004).

[10] A. K. McMahan, Phys. Rev. B **72**, 115125 (2005).

[11] W. H. Cloud, D. S. Schreiber, and K. R. Babcock, J. Appl. Phys. **33**, 1193 (1962).

[12] M. N. Iliev, A. P. Litvinchuk, H.-G. Lee, C. W. Chu, A. Barry, and J. M. Coey, Phys. Rev. B **60**, 33 (1999).

[13] H. kwang Mao, J. Shu, Y. Fei, J. Hu, and R. J. Hemley, Earth Planet. Inter. **96**, 135 (1996).

[14] J. Badro, V. V. Struzhkin, J. Shu, R. J. Hemley, H. kwang Mao, C. chang Kao, J.-P. Rueff, and G. Shen, Phys. Rev. Lett. **83**, 4010 (1999).

[15] F. Bloch, Z. Phys **52**, 555 (1928).

[16] A. H. Wilson, Proc. R. Soc. Lond. A **133**, 458 (1931).

[17] N. F. Mott, Proc. Phys. Soc. Lond. **62**, 416 (1949).

[18] W. H. Zachariasen and F. H. Ellinger, Acta. Cryst. A **33**, 155 (1977).

[19] B. Coqblin and A. Blandin, Adv. Phys. **17**, 281 (1968).

[20] B. Johanssen, Philo. Mag. **30**, 469 (1974).

[21] M. Lavagna, C. Lacroix, and M. Cyrot, Phys. Lett. **90A**, 210 (1982).

[22] M. Croft, J. H. Weaver, D. J. Peterman, and A. Franciosi, Phys. Rev. Lett. **46**, 1104 (1981).

[23] A. K. McMahan, K. Held, and R. T. Scalettar, Phys. Rev. B **67**, 075108 (2003).

[24] Y. Ji, G. J. Strijkers, F. Y. Yang, C. L. Chien, J. M. Byers, A. Anguelouch, G. Xiao, and A. Gupta, Phys. Rev. Lett. **86**, 5585 (2001).

[25] J. Hubbard, Proc. R. Soc. Lon. A **276**, 238 (1963).

[26] E. H. Lieb and F. Y. Wu, Phys. Rev. Lett. **20**, 1445 (1968).

[27] C. Lacroix and M. Cyrot, Phys. Rev. B **20**, 1969 (1979).

[28] N. Kawai and S. suke Mochizuki, Solid State Commun. **9**, 1393 (1971).

[29] T. Eto, S. Endo, M. Imai, Y. Katayama, and T. Kikegawa, Phys. Rev. B **61**, 14984 (2000).

[30] J.-P. Rueff, A. Mattila, J. Badro, G. Vanko, and A. Shukla, J. Phys.:Condens. Matter **17**, S717 (2005).

[31] D. Bloch, C. Vettier, and P. Burlet, Phys. Lett. A **83**, 4101 (1980).

[32] W. A. Grosshans, Y. K. Vohra, and W. B. Holzapfel, Phys. Rev. Lett. **49**, 1572 (1982).

[33] B. Johanssen and A. Rosengreen, Phys. Rev. B **11**, 2836 (1974).

[34] J. S. Olsen, L. Gerward, U. Benedict, and J. P. Itié, Physica B **133**, 129 (1985).

[35] B. J. Baer, H. Cynn, V. Iota, C.-S. Yoo, and G. Shen, Phys. Rev. B **67**, 134115 (2003).

[36] N. C. Cunningham, N. Velisavljevic, and Y. K. Vohra, Phys. Rev. B **71**, 012108 (2005).

[37] H. Hua, Rev. High Pressure Sci. Technology **7**, 233 (1988).

[38] D. G. Kaskimaki and J. K. A. Gschneider, *Handbook on the Physics and Chemistry of Rare Earths* (North-Holland, Amsterdam, 1978).

[39] A. P. Murani, S. J. Levett, and J. W. Taylor, Phys. Rev. Lett. **95**, 256403 (2005).

[40] J. B. Goodenough, Progress in Solid State Chemistry **5**, 145 (1971).

[41] K. Schwarz, J. Phys. F-Metal Phys. **16**, L211 (1986).

[42] K. P. Kämper, W. Schmitt, G. Güntherodt, R. J. Gambino, and R. Ruf, Phys. Rev. Lett. **59**, 2788 (1987).

[43] T. Tsujioka, T. Mizokawa, J. Okamoto, A. Fujimori, M. Nohara, H. Takagi, K. Yamaura, and M. Takano, Phys. Rev. B **56**, 15509 (1997).

[44] K. Suzuki and P. M. Tedrow, Phys. Rev. B **58**, 11597 (1998).

[45] T. Sharp, A. E. Goresy, B. Wopenka, and M. Chen, Science **284**, 1511 (1999).

[46] C. S. Yoo, H. Kohlmann, H. Cynn, M. F. Nicol, V. Iota, and T. LeBihan, Phys. Rev. B **65**, 104103 (2002).

[47] C. S. Yoo, B. Maddox, J. H. P. Klepeis, V. Iota, W. Evans, A. McMahan, M. Y. Hu, P. Chow, M. Somayazulu, D. Hausermann, R. T. Scalettar, and W. E. Pickett, Phys. Rev. B **94**, 115502 (2005).

[48] A. L. Chen, P. Y. Yu, and R. D. Taylor, Phys. Rev. Lett. **71**, 4011 (1993).

[49] A. W. Lawson and T. Y. Tang, Rev. Sci. Instrum. **21**, 815 (1950).

[50] C. E. Weir, E. R. Lippincott, A. V. Valkenburg, and E. N. Bunting, J. Res. **64**, 55 (1959).

[51] J. P. Ruoff, H. Xia, and Q. Xia, Rev. Sci. Instrum. **63**, 4342 (1992).

[52] D. J. Dunstan, Rev. Sci. Instrum. **60**, 3789 (1989).

[53] L. Merrill and W. A. Bassett, Rev. Sci. Instrum. **45**, 290 (1974).

[54] A. V. Valkenburg, Rev. Sci. Instrum. **33**, 1462 (1962).

[55] P. W. Bridgman, Proc. Am. Acad. Arts Sci. **84**, 111 (1955).

[56] A. Thompson, I. Lindau, D. Attwood, P. Pianetta, E. Gullikson, A. Robinson, M. Howells, J. Scofield, K.-J. Kim, J. Underwood, J. Kirz, D. Vaughan, J. Kortright, G. Williams, and H. Winick, X-ray Data Booklet (2001).

[57] G. J. Piermarini, S. Block, and J. D. Barnett, J. Appl. Phys. **44**, 5377 (1973).

[58] G. J. Piermarini, S. Block, J. D. Barnett, and R. A. Forman, J. Appl. Phys. **46**, 2774 (1975).

[59] H. K. Mao, J. Xu, and P. M. Bell, J. Geophys. Res. **91**, 4673 (1986).

[60] J. H. Eggert, F. Moshary, W. J. Evans, K. A. Goettel, and I. F. Silvera, Phys. Rev. B **44**, 7202 (1991).

[61] J. Miyahara, K. Takahashi, Y. Amemiya, N. Kamiya, and Y. Satow, Nucl. Instrum. Methods **A246**, 572 (1986).

[62] C. Kittel, *Introduction to Solid State Physics*, fifth ed. (John Wiley and Sons, New Jersey, 1976).

[63] A. P. Hammersley, Technical report, ESRF (unpublished).

[64] A. C. Larson and R. B. V. Dreele, Technical report, Los Alamos National Laboratory Report LAUR 86-748 (unpublished).

[65] R. Shankar, *Principles of Quantum Mechanics*, 2nd ed. (Plenum Press, New York, 1994).

[66] H. Ogasawara, A. Kotani, and B. T. Thole, Phys. Rev. B **50**, 12332 (1994).

[67] G. Kaindl, G. Kalkowski, W. D. Brewer, B. Perscheid, and F. Holtzberg, J. Appl. Phys. **55**, 1910 (1984).

[68] H. H. Johann, Z. Phys. **69**, 185 (1931).

[69] http://www.amptek.com/xr100cr.html, 2006.

[70] W. A. Harrison, *Electronic Structure and the Properties of Solids: The Physics of the Chemical Bond* (W. H. Freeman and Company, New York, 1980), p. 253.

[71] J. R. Ferraro and K. Nakamoto, *Introductory Raman Spectroscopy* (Academic Press, San Diego, 1994).

[72] *SPECTRA-PHYSICS Stabilite Series Laser Beam Specifications*, 2001.

[73] T. Yu, Z. X. Shen, J. He, W. X. Sun, S. H. Tang, and J. Y. Lin, J. Appl. Phys. **93**, 3951 (2003).

[74] K. Tsutsumi, H. Nakamori, and K. Ichikawa, Phys. Rev. B **13**, 929 (1976).

[75] T. Paiva, R. T. Scalettar, C. Huscroft, and A. K. McMahan, Phys. Rev. B **63**, 125116 (2001).

[76] M. H. Krisch, C. C. Kao, F. Sette, W. A. Caliebe, K. Hamalainen, and J. B. Hastings, Phys. Rev. Lett. **74**, 4931 (1995).

[77] C. Dallera, E. Annese, J. P. Rueff, M. Grioni, G. Vanko, L. Braicovich, A. Barla, J. P. Sanchez, R. Gusmeroli, A. Palenzona, L. Degiorgi, and G. Lapertot, J. Phys.: Condens. Matter **17**, S849 (2005).

[78] C. Dallera, M. Grioni, A. Palenzona, M. Taguchi, E. Annese, G. Ghiringhelli, A. Tagliaferri, N. B. Brookes, T. Neisius, and L. Braicovich, Phys. Rev. B **70**, 085112 (2004).

[79] M. H. Chen, K. Cheng, and W. R. Johnson, Phys. Rev. A **47**, 3692 (1993).

[80] P. Beiersdorfer, D. Knapp, R. E. Marrs, S. R. Elliot, and M. H. Chen, Phys. Rev. Lett. **71**, 3939 (1993).

[81] T. K. Sham, R. A. Gordon, and S. M. Heald, Phys. Rev. B **72**, 035113 (2005).

[82] J. Haines, J. M. Leger, and S. Hoyau, J. Phys. Chem. Solids **56**, 965 (1995).

[83] S. S. Rosenblum, W. H. Weber, and B. L. Chamberland, Phys. Rev. B **56**, 529 (1997).

[84] K. J. Kingma, R. E. Cohen, R. J. Hemley, and H. kwang Mao, Nature **374**, 243 (1995).

[85] J. Haines, J. M. Leger, C. Chataeu, R. Bini, and L. Ulivi, Phys. Rev. B **58**, R2909 (1998).

[86] S. Ono, K. Hirose, N. Nishiyama, and M. Isshiki, Am. Mineral. **87**, 99 (2002).

[87] J. Haines and J. M. Leger, Phys. Rev. B **55**, 11144 (1997).

[88] H. Hellwig, A. F. Goncharov, E. Gregoryanz, H. kwang Mao, and R. J. Hemley, Phys. Rev. B **67**, 174110 (2003).

[89] J. Haines, J. M. Leger, and O. Schulte, J. Phys.: Condens. Matter **8**, 1631 (1996).

[90] U. Ponkratz, F. Porsch, G. Wortmann, and W. B. Holzapfel, J. Alloys Compd. **359**, 99 (2003).

[91] F. Birch, J. Appl. Phys. **9**, 279 (1938).

[92] P. Vinet, J. H. Rose, J. Ferrante, and J. R. Smith, J. Phys.: Condens. Matter **1**, 1941 (1989).

[93] W. H. Weber, G. W. Graham, and J. R. McBride, Phys. Rev. B **42**, 10969 (1990).

[94] C. S. Yoo, H. Cynn, P. Söderlind, and V. Iota, Phys. Rev. Lett. **84**, 4132 (2000).

[95] M. P. Pasternak, G. K. Rozenberg, G. Y. Machavariani, O. Naaman, R. D. Taylor, and R. Jeanloz, Phys. Rev. Lett. **82**, 4663 (1999).

[96] G. K. Rozenberg, M. P. Pasternak, W. M. Xu, L. S. D. J. M. O. Guillén, R. Ahuja, B. Johansson, and T. L. Bihan, Phys. Rev. B **68**, 64105 (2003).

[97] I. I. Mazin, Y. Fei, R. Downs, and R. Cohen, Am. Mineral. **83**, 451 (1998).

[98] R. E. Cohen, I. I. Mazin, and D. G. Isaak, Science **275**, 654 (1997).

[99] B. Johanssen, Phys. Rev. B **15**, 5890 (1977).

[100] Y. Baer and W. D. Schneider, in *Handbook on the Physics and Chemistry of Rare Earths*, edited by K. A. Gschneidner, L. Eyring, and S. Hufner (Elsevier Science, North America, 1987), Vol. 10, p. 1.

[101] K. G. Wilson, Rev. Mod. Phys. **47**, 773 (1975).

[102] J. Allen and R. M. Martin, Phys. Rev. Lett. **49**, 1106 (1982).

[103] J. F. Mammone and M. Nicol, J. Phys. Chem. Solids **42**, 379 (1981).

[104] C. Lee and X. Gonze, J. Phys.: Condens. Matter **7**, 3693 (1995).

[105] P. Merle, J. Pascual, J. Camassel, and H. Mathieu, Phys. Rev. B **21**, 1617 (1980).

[106] J. E. Schirber and B. Morosin, Phys. Rev. Lett. **42**, 1485 (1979).

[107] T. I. Dyuzheva, N. A. Bendeliani, V. V. Brazhkin, and L. M. Kuznetshov, J. Alloys Compd. **315**, 59 (2001).

[108] J. Haines and J. M. Leger, Physica B **192**, 233 (1992).

[109] S. Sugano, Y. Tanabe, and H. Kamimura, *Multiplets of Transition Metal Ions in Crystals* (Academic Press, New York, 1970), Vol. 70.

[110] A. Chatterjee, A. K. Singh, and A. Jayaraman, Phys. Rev. B **6**, 2285 (1972).

[111] R. Cauble, P. M. Celliers, G. W. Collins, L. B. D. Silva, D. M. Gold, M. E. Foord, K. S. Budil, and R. J. Wallace, Astron. Astrophys., Suppl. Ser. **127**, 267 (2000).

[112] Y. Syono, RIKEN Rev. **27**, 72 (2000).

[113] J. N. Farrell and R. D. Taylor, Phys. Rev. Lett. **58**, 2478 (1987).

[114] K. Takemura and K. Syassen, J. Phys. F: Met. Phys. **15**, 543 (1985).

[115] W. A. Grosshans and W. B. Holzapfel, J. Magn. Magn. Mater. **47 & 48**, 295 (1985).

[116] K. Takemura and K. Syassen, in *Intern. Symp. on Solid State Physics under Pressure*, edited by S. Minomura (Terra Scientific Publ. Corp., Tokyo, 1984).

[117] K. Ishii, K. Tsutsui, Y. Endoh, T. Tohyama, K. Kuzushita, T. Inami, K. Ohwada, S. Maekawa, T. Masui, S. Tajima, Y. Murakami, and J. Mizuki, Phys. Rev. Lett. **94**, 187002 (2005).

[118] F. J. Morin, Phys. Rev. Lett. **3**, 34 (1959).

[119] M. C. Tobin, *Laser Raman Spectroscopy*, 1st ed. (Robert E. Kreiger Publishing Company, Melbourne, 1982).